Probing local anisotropies with Type Ia Supernovae from the Zwicky Transient Facility

Melissa Amenouche

To cite this version:

Melissa Amenouche. Probing local anisotropies with Type Ia Supernovae from the Zwicky Transient Facility. Cosmology and Extra-Galactic Astrophysics [astro-ph.CO]. Université Clermont Auvergne, 2022. English. NNT : 2022UCFAC101 . tel-04165406

HAL Id: tel-04165406
https://theses.hal.science/tel-04165406

Submitted on 19 Jul 2023

Université Clermont Auvergne
UMR 6533 - Laboratoire de Physique de Clermont
École Doctorale des Sciences Fondamentales

Étude des anistropies locales avec les Supernovae de Type Ia de la Zwicky Transient Facility

Présentée par **Melissa Amenouche**

Thèse de Doctorat en Particules, Inetraction, Universe

Soutenue publiquement le 5 décembre 2022

Devant un jury composé de:

Rigault, Mickael	CNRS (IP2I)	Rapporteur
Yan, Lin	Caltech	Rapporteure
Antilogus, Pierre	CNRS (LPNHE)	Examinateur
Monteil, Stéphane	CNRS (LPC) - UCA	Président
Roucelle, Cécile	Université Paris Cité	Examinatrice
Smith, Mathew	CNRS (IP2I)	Invité
Rosnet, Philippe	CNRS (LPC) - UCA	Directeur de thèse

Université Clermont Auvergne
UMR 6533 - Laboratoire de Physique de Clermont
École Doctorale des Sciences Fondamentales

Probing local anisotropies with Type Ia Supernovae from the Zwicky Transient Facility

Presented by **Melissa Amenouche**

supervised by Philippe Rosnet

PhD thesis in Particles, Interaction and Universe

Defended on the 5^{th} of December, 2022

Jury composition:

Rigault, Mickael	CNRS (IP2I)	Reviewer
Yan, Lin	Caltech	Reviewer
Antilogus, Pierre	CNRS (LPNHE)	Examiner
Monteil, Stéphane	CNRS (LPC) - UCA	President
Roucelle, Cécile	Université Paris Cité	Examiner
Smith, Mathew	CNRS (IP2I)	Guest
Rosnet, Philippe	CNRS (LPC) - UCA	Supervisor

Abstract

Probing local anisotropies with Type Ia Supernovae from the Zwicky Transient Facility

In this manuscript, I present our work on two key steps of Type Ia Supernovae (SNeIa) cosmology: photometric calibration and selection with the Zwicky Transient Facility (ZTF) data. We also investigated the detectability of bulk flow anisotropies with ZTF-like data to test ΛCDM model in the nearby Universe.

In order to improve the precision of ZTF photometric calibration, I developed a multi-epoch method that better constrains the calibrated quantities. With this technique, I calibrate simultaneously all images from the same ZTF field. To avoid any biases, I identified images with poor photometric quality and removed them from the time-series. In addition, I accounted for atmospheric extinction effects on the magnitudes.

To unlock ΛCDM tests in the local Universe with ZTF, I developed ZTF-like simulations to study bulk flows detectability with the first year sample. I applied the dipole method to estimate the bulk flows velocity and location. However any precision cosmology inference with ZTF SNeIa sample, bulk flow measurements included, requires to understand the biases and selection effects of the sample and how to correct for them. The only way to achieve this task is through realistic simulations. For this part of our work, a simulation tool *simsurvey* was used that produces SNeIa light-curves based on a survey observing strategy and SNeIa template. I used in simsurvey ZTF real-time observing information combined with *Spectral Adaptive Light-curve Template 2* (SALT2), state of the art SNeIa SED template, as SNeIa model to replicate the Data Release 2 (DR2) sample. To assess the accuracy of our simulations, every individual object of the DR2 was reproduced and I compared the simulated and measured quantities.

With this simulations framework, I investigated biases in the distance measurements. I compared the underlying population of SALT2 parameters, from realistic distribution input to simsurvey, to the fitted values on the simulated light-curves. No evidence of bias was found. The DR2 sample is constituted of spectroscopically confirmed SNeIa, whereas with the simulations framework we simulated all the objects that ZTF has observed photometrically. We aimed to apply the spectroscopic selection function of the DR2 sample to the simulations and investigated the selection. There is a good match when the distributions are compared, indicating that the DR2 sample is unbiased up to $z = 0.05$.

Résumé

Étude des anisotropes locales avec les Supernovae de Type Ia de la Zwicky Transient Facility

Les Supernovae de Type Ia (SNeIa) sont de puissants indicateurs de distances dans l'univers. Nous leur devons notamment la découverte de l'expansion accélérée de l'univers. Dans ce présent manuscrit seront présentés des travaux couvrant deux étapes cruciales dans l'utilisation des SNeIa provenant de la Zwicky Transient Facility (ZTF) en cosmologie. Il s'agit de la calibration photométrique des images du télescope et de l'étude des biais de sélection dans l'échantillon de données employé. La détectabilité d'anisotropies type *mouvements d'ensembles* avec des simulations, basées sur les données ZTF, afin de tester le modèle standard (Λ CDM) dans l'univers proche est aussi abordée.

Le pipeline actuel de ZTF réalise la calibration photométrique image par image. Dans le but d'améliorer la précision de cette étape de la calibration, une méthode multi-époque permet de mieux contraindre les paramètres de calibration. En effet, avec cette méthode, toutes les images d'un même champ d'observations de ZTF sont calibrées simultanément. Afin d'éviter de potentiels biais, il était nécessaire d'identifier et d'enlever les images de mauvaise qualité photométrique des séries d'images. De plus, les effets de l'extinction atmosphérique sur les magnitudes ont été pris en compte.

Nous avons développé des simulations similaires aux données ZTF afin de tester l'efficacité du modèle ΛCDM dans l'univers proche avec la détection de mouvements d'ensembles. À l'aide de la méthode dite du dipôle la vitesse et location des mouvements d'ensembles ont été estimées. Cependant, toute inférence cosmologique de précision, l'estimation de mouvements d'ensembles incluse, requiert l'étude des biais et effets de sélection de l'échantillon utilisé. Cette étude ne peut se faire qu'avec des simulations réalistes qui reproduisent les échantillons ZTF. À cet effet, un outil de simulations *simsurvey* a été utilisé. Il permet de produire des courbes de lumière de SNeIa en se basant sur une stratégie d'observation et un modèle de SNeIa. Pour notre étude, nous avons utilisé les informations d'observation en temps réel de ZTF combiné avec *Spectral Adaptive Light-curve Template 2* (SALT2), le modèle de SNeIa le plus efficace, en modèle de SNeIa pour simuler un échantillon de données SNeIa de ZTF (Data Release 2). Afin d'estimer la justesse de ces simulations, chaque objet de la DR2 a été reproduit puis comparé aux mesures.

À l'aide de cette structure de simulations, l'étude de la présence de biais dans les mesures de distances a été réalisée. Dans ce contexte, nous avons comparé les populations sous-jacentes des paramètres SALT2 utilisées dans simsurvey aux paramètres ajustés sur les courbes de lumière simulées. Aucun signe de biais dans les paramètres SALT2 n'a été observé. L'échantillon DR2 est constitué de SNeIa dont la classification a été confirmée spectroscopiquement, alors que la structure de simulations utilisée simule toutes les SNeIa que

ZTF a observé photométriquement. Nous avons appliqué la fonction de sélection spectroscopique de la DR2 aux simulations et comparé les distributions des échantillons mesurés et simulés. Une bonne correspondance entre les deux lots est trouvée. Il en résulte de cette étude que l'échantillon de la DR2 est non-biaisé jusqu'à $z = 0.05$.

CONTENTS

List of Figures

INTRODUCTION

Type Ia Supernovae (SNeIa) are standardisable candles, they are widely used as distance indicators in observational cosmology. For more than two decades, their observations have been used to measure distances to extra-galactic objects. The comparison of distances and velocities of distant objects enables to put constraints on the content and dynamics of the universe. In this context, the accelerated expansion of the universe was discovered in the late 90 s with SNeIa distance measurements (Riess et al. 1998; Perlmutter et al. 1999) which revealed the existence of Dark Energy. The nature of this component is still unknown, large scientific efforts are being held to characterise it.

A crucial assumption of the standard model of cosmology (ΛCDM) is the homogeneity and isotropy of the universe on sufficiently large scales. It implies that there is no preferred location or direction in the universe. Theses basic symmetries were essential for the development of the metric that we use today as the description of the universe. However, on small scales we observe deviations from these assumptions since the universe is highly inhomogeneous. These inhomogeneities are explained, within ΛCDM, by structure formation theory, they grew from initially small fluctuations of the density field through gravitational collapse. This sets limits on the amplitude of the inhomogeneities and anisotropies that are expected in the universe. Measuring these amplitudes and comparing them to ΛCDM predictions is a key test of our standard model. SNeIa as standardisable candles are used to probe the matter density field through *bulk flow* measurements. In these studies, no deviation from ΛCDM was noticed. However, there are many limitations in the samples used, noticeable in the large uncertainties they display on the measurements: the sample volume and control of systematic uncertainties.

The Zwicky Transient Facility (ZTF) will unlock unprecedented bulk flow measurements. It has been running for five years and its SNeIa sample is the largest found in the literature. Nonetheless, to precisely measure any cosmological quantities with ZTF, bulk flows included, we must understand what are the selections in the sample and how they impact our measurements. Simulations are crucial tools to understand biases in samples.

In the present manuscript, we present in Chapter 1 the essential elements of cosmology to introduce the ΛCDM model and its description of our universe with the current challenges it is facing. In Chapter 2, we focus on bulk flows theory, how they can be measured with SNeIa, we also review the current measurements of bulk flows from multiple probes and how new wide-field surveys like ZTF can change the landscape we drew up. In Chapter 3, we present the ZTF experiment and the data set used for our work in Chapter 7.1.3. In Chapter 4, we present our work on improving ZTF flux level precision with a new technique to perform ZTF photometric calibration. It is followed by an introduction to SNeIa, the standardisable candles and their use in cosmology. In Chapter 6, we investigate the detectability of bulk flows with ZTF-like simulated distance measurements. Finally, in Chapter 7.1.3 we present how we tuned realistic SNeIa that enabled us to reproduce all the SNeIa light-curves from the first three years of ZTF, investigated biases in the underlying populations of this sample along with its spectroscopic selection.

CHAPTER 1

ELEMENTS OF COSMOLOGY

Cosmology is the science that aims to explain the origin and evolution of the universe and describes its content and dynamics. It consists of theoretical modelling of large-scale gravity and on astronomical observations. This chapter summarises the fundamental theory for cosmology with an homogeneous and isotropic expanding universe to structure formation in Section 1.1. We review the current inconsistencies between the theoretical predictions and the observations in Section 1.2.

1.1 The Standard Model of Cosmology

In this section, we introduce all the theoretical ingredients of the standard model of cosmology. The Cosmological Principle (CP) is introduced in 1.1.1, followed by the metric used in 1.1.2, expansion and content of the universe in respectively 1.1.3 and 1.1.4. In 1.1.5, we introduce the structure formation the frame of the standard model of cosmology.

1.1.1 The Cosmological Principle

The Cosmological Principle is the fundamental assumption that the Universe is homogeneous and isotropic : invariant under translation and rotation. All our current understanding of the universe is based on this principle. Principle that is only valid at large scales, as showed by sky surveys such as the Two-degree Field Galaxy Redshift Survey (2dFGRS)[1] or the Sloan Digital Sky Survey (SDSS)[2], it breaks down on smaller scale, typically below 100 Mpc. These symmetries only apply to the spatial component of the cosmological models. It allows us to study the evolution of the Universe.

1.1.2 The Universe in General Relativity

General Relativity (GR) theory, introduced by A. Einstein, demonstrated that gravity can be expressed as a curved space-time caused by any energy density. As a result, the evolution of the universe can depend directly on the energy density and pressure in the universe.

Einstein equation

In GR, the curvature of space-time is described using four-dimensional metric tensor $g_{\mu\nu}$ that defines an invariant differential of distance ds:

$$ds^2 = g_{\mu\nu} dx^\mu dx^\nu \tag{1.1}$$

The metric tensor, $g_{\mu\nu}$, is related to the densities of energy and momentum by Einstein's field equation :

$$R_{\mu\nu} - \frac{1}{2} g_{\mu\nu} R = -\frac{8\pi G}{c^4} T_{\mu\nu} + \Lambda g_{\mu\nu}, \tag{1.2}$$

---

[1] `http://2dfgrs.net/`

[2] `http://sdss.org/`

where $R_{\mu\nu}$ the Ricci curvature tensor, G Newton's gravitational constant, c the speed of light and $T_{\mu\nu}$ the energy-momentum tensor. Λ, the cosmological constant, was introduced by Einstein in order to obtain a static solution to the equation and hence a static model of the Universe (Einstein 1917). The universe is in expansion, as expressed by the Hubble law (more in Section1.1.3), Einstein abandoned this assumption. Nonetheless, the cosmological constant became of great interest after the discovery of the accelerated expansion of the Universe Riess et al. 1998; Perlmutter et al. 1999, as discussed further in 1.1.4.

FLRW Metric

The most basic model describing a spatially homogeneous and isotropic universe evolving in time, within GR, is the Friedmann-Lemaître-Robertson-Walker (FLRW) metric Friedmann 1922; Lemaître 1927; Robertson 1929; Walker 1933:

$$ds^2 = c^2dt^2 - a^2(t)\left(d\mathscr{X}^2 + \mathscr{F}_K^2(\chi)(d\theta^2 + \sin^2\theta d\phi^2)\right), \tag{1.3}$$

with $a(t)$ the scale factor of the universe (by convention $a(t_0) = 1$ for today[3]), χ is a comoving radial coordinate, θ and ϕ are angular coordinates and K is the curvature of the universe. $\mathscr{F}$ is the comoving angular diameter distance, which depends on the space-curvature and hence on K:

$$\mathscr{F}(\chi) = \begin{cases} \sqrt{|K|}^{-1}\sin(\sqrt{|K|}_{\chi} & \text{for} \quad K > 1, \\ \chi & \text{for} \quad K = 0, \\ \sqrt{|K|}^{-1}\sinh(\sqrt{|K|}_{\chi} & \text{for} \quad K < 0. \end{cases} \tag{1.4}$$

The different values for K correspond to, respectively, closed (spherical), flat and open (hyperbolic) universes. In a universe with FLRW metric, distances between objects, like galaxies, will increase (or decrease in case of a collapsing universe) according to the temporal evolution of the scale-factor $a(t)$. Therefore, the further the object is located from an observer, the faster it will appear to recede. This recession can be observed as a Doppler shift of the light emitted by the object. The observed effect can be related to the scale factor of the FLRW metric Equation (1.3) along a radial geodesic. Let's suppose that an object emits two flashes of light at t and $t + \Delta t_{em}$, which are received at t_0 and $t_0 + \Delta t_{obs}$. Assuming that the Δt's are small compared to $t_0 - t$, and that $a(t)$ is significantly invariant in the time between the two emissions, the light propagation equation $ds^2 = 0$ from the emitting source (em) to the observer (obs) gives :

$$\int_t^{t_0} \frac{cdt'}{a(t')} = \int_{t+\Delta t_{em}}^{t_0+\Delta t_{obs}} \frac{cdt'}{a(t')} = \int_t^{t_0} \frac{cdt'}{a(t')} + \frac{c\Delta t_{obs}}{a(t_0)} - \frac{c\Delta t_{em}}{a(t)} \tag{1.5}$$

Since $a(t_0) = 1$, it implies that Δt_{em} is stretched along the way to the observer by a factor $1/a(t)$ and therefore the observed frequency of the light decreases:

$$\frac{\Delta t_{obs}}{\Delta t_{em}} = \frac{\nu_{em}}{\nu_{obs}} = \frac{\lambda_{obs}}{\lambda_{em}} = \frac{1}{a(t)} = 1 + z, \tag{1.6}$$

---

[3] The subscript 0 refers to the current value of quantity, here it is the time t_0

where z is called the cosmological redshift. Therefore, the properties of an object's spectrum, namely, the shifted positions of spectral lines, are a direct probe of the scale factor of the universe at the time of emission.

Friedmann Equations

The distribution of energy in the universe is approximated as a perfect fluid, when applying the Cosmological Principle to the energy-momentum tensor $T_{\mu\nu}$:

$$T_{\mu\nu} = \left(\rho + \frac{P}{c^2}\right) u_\mu u_\nu + P g_{\mu\nu}, \tag{1.7}$$

where ρ is the energy density, p the pressure and $u = (1, 0, 0, 0)$ a velocity 4-vector. For the FLRW metric the $(0, 0)$-component of the Ricci tensor and the Ricci scalar becomes:

$$R_{00} = 3\frac{\ddot{a}}{a} \tag{1.8}$$

$$R = \frac{G}{c^2 a^2} \tag{1.9}$$

A combination of these equations with Einstein's field equation (1.2) would give the temporal evolution of the scale factor $a(t)$, in the case of a universe with perfect fluids. It is known as the first Friedmann equation Friedmann 1922:

$$3\left(\frac{\dot{a}}{a}\right)^2 + 3\frac{Kc^2}{a^2} = 8\pi G\rho + \Lambda c^2 \tag{1.10}$$

$$\Rightarrow H^2 \equiv \left(\frac{\dot{a}}{a}\right)^2 = \frac{8\pi G}{3}\rho + \frac{\Lambda c^2}{3} - \frac{Kc^2}{a^2}, \tag{1.11}$$

where H is the Hubble parameter.

To solve this equation, we need to know the evolution of ρ the density. Due to conservation of energy, the energy-momentum tensor $T_{\mu\nu}$ must have a vanishing divergence :

$$\begin{aligned} \nabla_\mu T^\mu_0 &= 0 \\ &= -\dot{\rho} - 3\frac{\dot{a}}{a}\left(\rho + \frac{P}{c^2}\right). \end{aligned} \tag{1.12}$$

The density and pressure are related by the equation of state $P = w\rho c^2$ with a constant parameter w. From this follows that

$$\frac{\dot{\rho}}{\rho} = -3(1+w)\frac{\dot{a}}{a} \tag{1.13}$$

The general solution for this equation is :

$$\rho \propto a^{-3(1+w)} \tag{1.14}$$

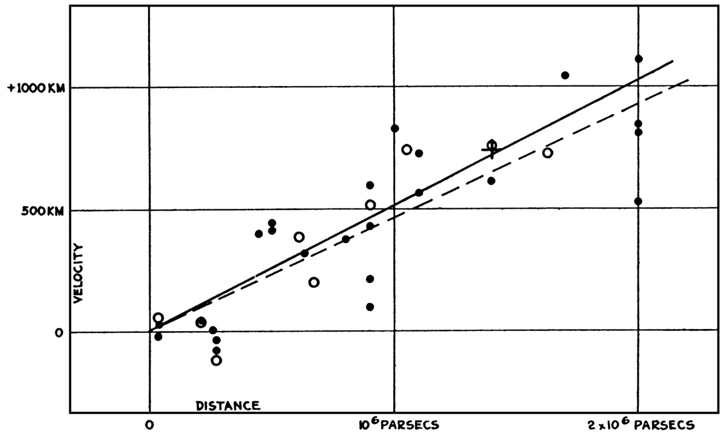

Figure 1.1: Original Hubble diagram, produced from distance measurements of galaxies. It shows velocities recession of galaxies (in $\mathrm{km\,s^{-1}}$) in function of their distances (Hubble 1929).

By differentiating the first Friedmann equation (1.11) in time and substituting equation (1.12), the *second Friedmann equation*, which is a relation between density, pressure and the acceleration of the expansion of the universe can be found :

$$\frac{\ddot{a}}{a} = \frac{4\pi}{3}\left(\rho + 3\frac{P}{c^2}\right) + \frac{\Lambda c^2}{3} \tag{1.15}$$

1.1.3 The expanding universe

At the beginning of the 20th century, the universe was thought to be static. The idea of an expanding universe was born in 1929 from galaxy distance measurements by Hubble. He measured the distances to "extra-galactic nebulae", galaxies, outside the Milky Way and compared to their redshift Hubble 1929. Hubble found a linear relation between these distances and velocities seen in Fig 1.1. The linear relation is known as the Hubble law and is expressed as :

$$v = H_0 d, \tag{1.16}$$

with H_0 is the Hubble constant, the current value of the Hubble parameter. The measurements by Hubble, gave an approximate value of $H_0 = 500\ h^{-1}\,\mathrm{Mpc}$, where h is the normalisation factor, historically introduced in the parametrisation of the Hubble constant, it is measured at ~ 0.7. The first measurement of H_0 was overestimated due to bad distance calibration. All the current measurements of H_0 are discussed further in 1.2.1.

1.1.4 Energy Content of the Universe

We find three basic cases of energy densities, characterised by their equation-of-state parameters w.

Matter: baryons and dark matter

Non-relativistic matter has no pressure and is denoted with the subscript m. From the equation of state, we note that $w = 0$. The energy density of matter is dominated by its mass energy. Thus, the energy conservation equation becomes :

$$\dot{\rho}_m = -3H\rho_m, \tag{1.17}$$

when integrated over the time, the density decreases as the cube of the scale factor ($\rho_m \propto a^{-3}$).

At first, non-relativistic matter included only ordinary (**baryonic**) matter. However, in the early 20 th century observations, by Zwicky and Smith (Zwicky 1933), of galaxies in the Coma and Virgo clusters provided the first hints for another type of non-relativistic matter. Their estimations of the total mass required to gravitationally bind the galaxies were two orders of magnitude above Hubble's estimation of the galaxy mass. This led Zwicky to postulate the existence of an "invisible" matter that interacts gravitationally and does not with electromagnetic radiation. It is now known as **dark matter** and is studied using probes like BAO (*Baryons Acoustic Oscillations*), the CMB (*Cosmic Microwave Background*) and SNeIa. However, no direct or indirect detection of dark matter has been recorded to the present date. The particles of this matter are supposed to be too small to erase structure formation in the early universe and this matter is thought to be "cold". In the current cosmological model, non-relativistic matter is composed of baryons and cold dark matter (CDM).

Radiation

Particles with velocities close to the speed of light c are considered as relativistic matter or radiation. Radiation, subscript r, is described by the equation of state $\rho_r = 3P_r$. It denotes a state parameter of $w = \frac{1}{3}$ for radiation. The energy conservation equation for radiation follows :

$$\dot{\rho}_r = -4H\rho_r, \tag{1.18}$$

integrating over time, the density evolves as $\rho_r \propto a^{-4}$. The radiation density decreases faster than that of matter because the photons lose energy when they are redshifted, reducing the energy by an additional factor of a. In the current model radiation is accounted for by photons and neutrinos.

Dark Energy

The effect of the cosmological constant in Einstein's equation can be reproduced by an homogeneous fluid with pressure $P_\Lambda = -\rho_\Lambda$, using:

$$\rho_\Lambda = \frac{\Lambda c^4}{8\pi G}. \tag{1.19}$$

Dark Energy is considered as a fluid with negative pressure. The introduction of such a fluid was motivated by the accelerated expansion of the universe. In 1998, two teams lead by Perlmutter on one side, Riess and Schimdt on the other side discovered that the universe is expanding in an accelerated way that disagrees with a matter (baryonic and dark matter) and radiation Universe described by GR (Perlmutter et al. 1999; Riess et al. 1998).

It is convenient to express all energy densities in units of the critical density, which depends on the *Hubble constant* H_0, i.e the current value of the Hubble parameter $H = \dot{a}/a$:

$$\rho_{cr} = \frac{3H_0^2}{8\pi G}. \tag{1.20}$$

For each component i, the normalised density parameter Ω_i is defined as :

$$\Omega_i(t) = \frac{\rho_i(t)}{\rho_c(t)}, \tag{1.21}$$

where i stands for all components in the universe, introduced above. Then, the total energy density $\rho_{total} = \sum_i \rho_i$.

As a function of the normalised density parameters today $\Omega_{i,0}$, the first Friedmann equation (1.11) can be written as :

$$\left(\frac{H}{H_0}\right)^2 = \Omega_{k,0}a^{-2} + \Omega_{m,0}a^{-3} + \Omega_{r,0}a^{-4} + \Omega_{\Lambda,0}, \tag{1.22}$$

where a and H are functions of time. Using Equation(1.6), we found :

$$\left(\frac{H}{H_0}\right)^2 = \Omega_{k,0}(1+z)^2 + \Omega_{m,0}(1+z)^3 + \Omega_{r,0}(1+z)^4 + \Omega_{\Lambda,0}, \tag{1.23}$$

at $t = t_0$ this equation becomes :

$$\Omega_{r,0} + \Omega_{m,0} + \Omega_{\Lambda,0} = 1 - \Omega_{k,0}. \tag{1.24}$$

For our flat Universe, we can find that the total energy density is equal to the critical density

$$\Omega_{r,0} + \Omega_{m,0} + \Omega_{\Lambda,0} = 1 \Rightarrow \rho_{r,0} + \rho_{m,0} + \rho_{\Lambda,0} = \rho_c. \tag{1.25}$$

We have now introduced all the ingredients of the current cosmological model.

Beyond ΛCDM

In a more general universe, the cosmological constant (Λ) can be substituted by a dark energy density that has an arbitrary equation-of-state parameter w :

$$P_{DE} = w\rho_{DE}c^2, \tag{1.26}$$

where w is the dark energy state parameter and one of the free parameters of ΛCDM model. Equation (1.23) becomes then :

$$H(z) = H_0\sqrt{\Omega_{m,0}(1+z)^3 + \Omega_{K,0}(1+z)^2 + \Omega_{r,0}(1+z)^4 + \Omega_{DE,0}(1+z)^{3(1+w)}}. \quad (1.27)$$

ΛCDM model belongs to cosmological family models called wCDM. The case of the standard model with $w = -1$ corresponds to Einstein cosmological constant (Λ). Furthermore, the dark energy state parameter can itself depend of the redshift, in the *Chevallier-Polarski parametrisation*, suggested in Chevallier and Polarski 2001 :

$$w(a) = w_0 + w_a(1-a), \quad (1.28)$$

where w_0 is the current value of w and w_a is the directing coefficient that determines the temporal dependency. Evidence of physics beyond the ΛCDM model would be to measure values of w_a different from 0 and/or w_0 different from -1.

1.1.5 The inhomogenous universe

The FLRW metric assumes that the universe is homogeneous and isotropic, through the Cosmological Principle. However, this assumption is valid only at large scales, as mentioned in 1.1.1. In fact, the universe is strongly inhomogeneous, the biggest evidence being the existence of structures like galaxies and stars. Moreover, the CMB temperature anisotropies Kogut et al. 1993 showed the inhomogeneity of the universe at its earliest time. The standard model of cosmology posits that these large structures we observe today, due to the gravitational interaction, grew from small initial fluctuations, at early times of the universe.

Linear theory

In a Newtonian approach, the matter density $\rho(\mathbf{x}, t)$ can be described as a fluid with a velocity field $\mathbf{u}(\mathbf{x}, t)$. Its time evolution is ruled by the gravitational potential $\Phi(\mathbf{x}, t)$ such that:

$$\frac{\partial \rho}{\partial t} + \nabla \cdot (\rho \mathbf{u}) = 0, \quad (1.29)$$

$$\frac{\partial \mathbf{u}}{\partial t} + (\mathbf{u} \cdot \nabla)\mathbf{u} = -\nabla\Phi, \quad (1.30)$$

$$\nabla^2\Phi = 4\pi G\rho. \quad (1.31)$$

Noting $\bar{\rho}$ as the mean value of the density, we can introduce, $\delta(\mathbf{x})$, the density contrast which is a measure of overdensity, defined at every point :

$$\delta(\mathbf{x}, t) = \frac{\rho(\mathbf{x}, t) - \bar{\rho}(t)}{\bar{\rho}(t)}. \quad (1.32)$$

The linear theory is valid at sufficiently early times and large spatial scales and when the fluctuations in the density are less than unity ($|\delta| << 1$). At first approximation, the growth of matter density ρ_m fluctuations in time and within the Hubble radius can be obtained by solving the evolution equation:

$$\ddot{\delta} + 2H\dot{\delta} - 4\pi G \rho_m \delta = 0, \tag{1.33}$$

where $\dot{\delta}$ and $\ddot{\delta}$ are respectively the first and second derivative of the density contrast (δ) with respect to time t. As the evolution of Equation (1.33) is only time dependent, a solution with separate spatial and temporal components is suitable:

$$\delta(\mathbf{x}, t) = D_+(t)\delta(\mathbf{x}) + D_-(t)\delta(\mathbf{x}), \tag{1.34}$$

where $D_+(t)$ corresponds to the growing mode over time, responsible for the growth of perturbations and subsequent formation of the Large Scale Structures (LSS), while $D_-(t)$, is the decaying mode and becomes negligible over time. In a ΛCDM universe, the solution yields

$$D_+(t) \equiv D_+(a) \propto \frac{\dot{a}}{a} \int_0^a \frac{da'}{\dot{a}'^3} = H(t) \int \frac{a^2(t)}{H^2(t)} dt, \tag{1.35}$$

$$D_-(t) \propto \frac{\dot{a}}{a} = H(t) \tag{1.36}$$

The growing mode D_+ is known as the *growth factor of structure* and gives us the time evolution of δ the matter density field. The growth rate of structure is defined as:

$$f := \frac{d \ln D_+}{d \ln a} \tag{1.37}$$

Considering a matter-dominated universe, the growth rate of structure describes the rate at which structures form and can be parameterised as follows Peebles 1980:

$$f \approx \Omega_m(a)^\gamma \tag{1.38}$$

where γ is a crucial parameter since it depends on the dark energy equation of state Linder 2003 :

$$\gamma = \frac{3(w_{DE} - 1)}{6w_{DE} - 5} \tag{1.39}$$

In the framework of GR, it is predicted to be $\gamma \approx 0.55$, any deviation from the expected value would imply a non-standard dark energy such as modified gravity (Linder and Cahn 2007). Observations of the growth of structures provide rich information about dark matter and dark energy.

Within ΛCDM framework, a parameterized approximation of the growth factor of structure was proposed in Lahav et al. 1991

$$f(z) \approx \Omega_m(z)^{0.6} + \frac{1}{70}\left(1 - \frac{\Omega_m(z)}{2}(1 + \Omega_\Lambda(z))\right) \tag{1.40}$$

with the redshift evolution of the density parameters $\Omega_m(z) = \Omega_{m,0}(1+z)^3/E^2(z)$ and $\Omega_\Lambda(z) = \Omega_{\Lambda,0}/E^2(z)$, with $E(z) = H(z)/H_0$.

Two-point correlation function

In order to characterize the structure formation in the universe, $\delta(\mathbf{x}, t)$ has to be thought as a realisation of a stochastic process. In this way, the statistical tool to study the matter distribution in the universe from galaxies distribution, galaxy clustering or CMB anisotropies is the *two-point correlation function* :

$$\zeta(x) = \langle \delta(\mathbf{x_1})\delta(\mathbf{x_2}) \rangle \text{ with } x = |\mathbf{x_2} - \mathbf{x_1}|, \tag{1.41}$$

where $\langle ... \rangle$ denotes the average value of the stochastic process underlying the random (δ or ρ) field, by taking into account its homogeneous and isotropic properties at large scale, i.e. ζ, depends only on the scalar separation of the two-point $x = |\mathbf{x_2} - \mathbf{x_1}|$. In Fourier space, the two-point correlation function defines the power spectrum

$$P(k) = \hat{\zeta}(k) = \int \zeta(x) \mathrm{e}^{-i\mathbf{k}\cdot\mathbf{x}} d\mathbf{x}. \tag{1.42}$$

The amount of matter fluctuations averaged over a sphere of radius 8 h^{-1}Mpc, known as σ_8, at redshift z in a commonly used probe of the growth of structures. Its physical meaning is how much the mass within a sphere of radius 8 h^{-1}Mpc fluctuates from one point to another in the universe. In the framework of the structure formation theory, it corresponds to the variance of the two-point correlation function within a sphere of of radius 8 h^{-1}Mpc

$$\sigma_8^2 = \sigma_R^2(R = 8\, h^{-1}\text{Mpc}) = \frac{1}{2\pi^2} \int k^2 P(k) |W(k, R)|^2 dk, \tag{1.43}$$

where $W(k, R))$ is the filter function used to reject the small scales (high k values) characterized by large local over density. In general for cosmological analysis a top-hat filter function is used: $W(k, R) = \frac{3}{(kR)^3} (\sin(kR) - kR \cos(kR))$. Within ΛCDM, the estimated value in the present universe is $\sigma_8 \approx 0.8$.

Observations of the growth of structures provide a rich information about dark matter and dark energy. More specifically, the scaling of the amplitude of growth of the structure vs. cosmic time, also known as the *growth function*, constrains dark energy parameters in a complementary way to distance measurements.

1.2 Tensions between measurements and ΛCDM

A multiple variety of cosmological observations during the past years have validated the ΛCDM model as the standard model of cosmology. Amongst the major successes of the standard cosmological model:

- the Cosmic Microwave Background (CMB) angular power spectrum of perturbations Komatsu et al. 2011 is in good agreement with the predictions of the standard model. Despite that, there are few issues related to the orientation and magnitude of low multipole moments (CMB anomalies).

- CMB temperature perturbation maps are consistent with the predictions of the standard model.
- Observations of the accelerating expansion of the universe compatible with the prediction of Einstein's cosmological constant Λ, Scolnic et al. 2018.
- Observations of large scale structure in good agreement with ΛCDM model predictions.

In spite of the good fits of the standard model, with only six free parameters, to all the current cosmological observations Planck Collaboration et al. 2020; Scolnic et al. 2018 (to cite only few), ΛCDM is facing some challenges. Some of the these challenges are referred to as crisis. Below, we list the current inconsistencies between the measurements and ΛCDM predictions.

1.2.1 The Hubble constant H_0

As introduced before, the Hubble constant H_0 describes the expansion rate of the Universe today. Its measurement is achieved in two main ways :
(i) with luminosity distance measurements of standardisable candles and their redshifts due to the cosmic expansion, anchored on a second independent SNeIa sample calibrated on Cepheids or Tip of the Red Giant Branch (TRGB) (Freedman et al. 2001) and by computing the proportionality factor (Hubble Law). This approach is model-independent and is based on geometrical measurements.
(ii) By using early universe probes and assumptions about a model for the expansion of the universe. For this way, we have the CMB measurements and assume ΛCDM as the standard model of cosmology where, as seen in 1.1.2, the expansion history of the universe is obtained with the Friedmann's equations.

These two methods of estimating H_0 provide independent measurements, the measured quantities are close to each other. However some are incompatible like direct measurements with SNeIa and indirect ones obtained from the CMB. P. A. R. Ade et al. 2014 provided a confirmation of the standard model ΛCDM with indirect measurement of H_0 with the CMB. However this indirect measurement was a little bit lower ($67.3 \pm 1.2\ \mathrm{km\,s^{-1}\,Mpc^{-1}}$) than the direct measurement made by the SH0ES collaboration Riess et al. 2011; Humphreys et al. 2013, based on Cepheids and SNeIa distances ($72.7 \pm 2.4\ \mathrm{km\,s^{-1}\,Mpc^{-1}}$). This incompatibility is now confirmed as a "tension" at the 5σ level, with more precise measurements, Planck Collaboration et al. 2020 at $H_0 = 67.4 \pm 0.5\ \mathrm{km\,s^{-1}\,Mpc^{-1}}$ and Riess et al. 2022 found $H_0 = 73.2 \pm 1.3\ \mathrm{km\,s^{-1}\,Mpc^{-1}}$.

Fig. 1.2 illustrates the tension and sum up all the H_0 measurements from several probes. This tension could be a sign of new fundamental physics or the sign of a bias in the direct or indirect measurements of H_0. For example with SNeIa, the bias could come from environmental dependencies of their distance, discussed further in 5.3.2. From the same figure 1.2, we can see that the dispersion of H_0 measured with CMB and SNeIa is significantly reduced when the SNeIa luminosities are calibrated with another probe than the Cepheids, like the

TRGB. We can affirm that this compilation plot shows the H_0 tension. Moreover it indicates that the precise way to calibrate SNeIa luminosities remains still unknown, since the cosmological estimations seem to vary with the methods of SNeIa luminosities calibration.

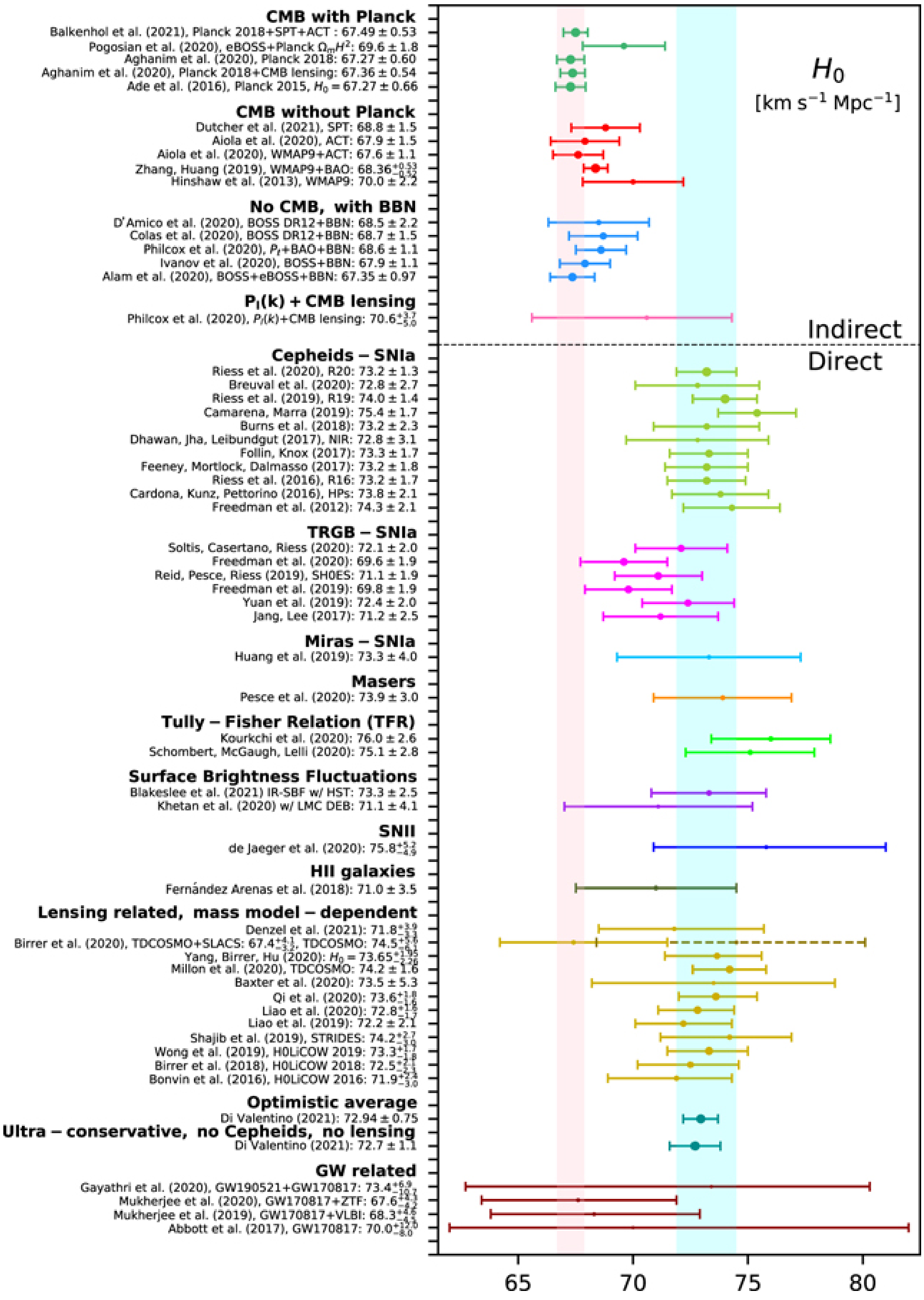

Figure 1.2: Comparison plot with 68% CL constraints of H_0 through direct (top) and indirect (bottom) measurements with the associated uncertainties by different surveys and groups produced over the years. The cyan vertical band corresponds to the H_0 measurements from the SH0ES collaboration Riess et al. 2021, while the pink one corresponds to the H_0 value as reported by Planck Collaboration et al. 2020 performed with ΛCDM scenario. Whisker plot from Di Valentino et al. 2021b.

1.2.2 The growth parameter σ_8

Also known as the $\Omega_{m,0} - \sigma_8$ tension, it refers to the incompatibility of the growth factor (see Section1.1.5) measurements from CMB data, at high redshift with low-z probes such as weak gravitational lensing and redshift-space galaxy clustering. With weak gravitational lensing, images from distant galaxies which are gravitationally lensed by the intervening matter are analysed to understand LSS in the universe. Redshift-space galaxy clustering are based on RSD (Redshift Space Distortion, Kaiser 1987) measurements, these distortions are correlated to $f\sigma_8$.

The tension can be visualized in the $\sigma_8 - \Omega_m$ plane in Fig 1.3, from Heymans, Catherine et al. 2021, and is quantified in the literature using the $S_8 \equiv \sigma_8\sqrt{\Omega_m/0.3}$ parameter. Assuming ΛCDM, Planck measurements Planck Collaboration et al. 2020 (in grey contour in Fig 1.3) are in disagreement with measurements from lensing Abbott et al. 2018 (orange) and galaxy clustering Tröster, Tilman et al. 2020 (purple). The low-z probes combination enable to tight the constraints but do not release the tension on σ_8. From Heymans, Catherine et al. 2021, the tension is reported at $\sim 3\sigma$. As for any tension, it could be due to systematic uncertainties unaccounted for or sign of physics beyond ΛCDM predictions, Di Valentino et al. 2021a lists the theoretical solutions investigated by multiple papers. Measuring peculiar velocities of galaxies with Type Ia Supernovae can contribute to precisely measure σ_8, especially with the increasing number of SNeIa observed from transient machine like the Zwicky Transient Facility (ZTF) or future wide-surveys like the Legacy Survey of Space and Time (LSST).

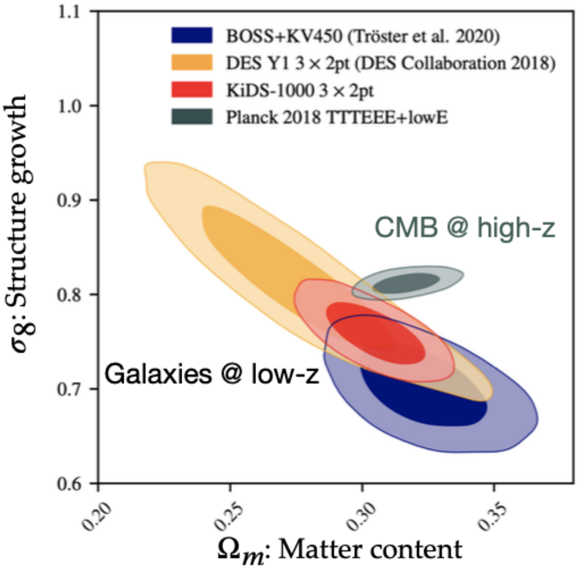

Figure 1.3: 68% CL and 95% CL Contour plots for σ_8 and Ω_m, from Heymans, Catherine et al. 2021.

1.2.3 Bulk flows

The standard model of cosmology assumes that the universe is statistically isotropic and homogeneous on large scales. Overall the isotropy was confirmed with Cosmic Microwave Background (CMB) temperature fluctuations which are directional independent (latest, Planck Collaboration et al. 2020). Coherent motion of matter, referred to as bulk flows, were detected in our cosmic neighbourhood. The amplitude of these motions converged, for some studies, to the Hubble expansion like in Feindt et al. 2013; Scrimgeour et al. 2015. However studies like Kashlinsky et al. 2010 claimed the existence of large bulk flow of $\sim 1000\,\mathrm{km\,s^{-1}}$ at scales $(0.07 < z < 0.2)$ at which the coherent velocity dipole is expected to be $100\,\mathrm{km\,s^{-1}}$. In Chapter 2, we introduce the needed tools and review bulk flow measurements.

CHAPTER 2

BULK FLOWS WITH TYPE IA SUPERNOVAE

One of the pillars of the Standard Model of Cosmology is the Cosmological Principle (see 1.1.1): at large scales ($\gtrsim$ 100 Mpc) it is assumed that there is no preferred direction or position in the universe. On smaller scales ($\lesssim$ 100 Mpc), the homogeneity assumption is non-valid since gravity makes matter clumps together to form the structures we observe today. As introduced in 1.1.5, growth structure originates from initially small density fluctuations through gravitational collapse, which is consistent with ΛCDM model. On top of the Hubble recessional velocities, the formed structures (galaxy clusters) exhibit peculiar motions arisen from gravitational perturbations creating coherent motion of matter, also referred to as *bulk flows*. These local anisotropies are expected by ΛCDM model and their amplitudes are predicted in this frame. Bulk flow measurements enable us to trace the matter density fluctuations and test whether the cosmological model accurately describes the motion of galaxies in the nearby universe. One of strongest observed anisotropies is the motion of our Local Group of galaxies (Kogut et al. 1993) with respect to the universal expansion at $620{\pm}15\,\mathrm{km\,s^{-1}}$ towards $l = 271.9{\pm}2°$, $b = 29{\pm}1.4°$, inferred from temperature fluctuations of the Cosmic Microwave Background CMB ($\Delta T/T 10^{-3}$) P. A. R. Ade et al. 2014. This anisotropy is also known as the CMB dipole, the frame in which the CMB is isotropic is referred to *CMB rest-frame*.

In this chapter, we introduce the cosmological observables, various definitions of distance in an expanding universe, peculiar velocities and effect of those on distance measurements in Section 2.1. We therefore present ΛCDM predictions for bulk flows velocities derived from the matter density field in Section 2.2. We introduce a well-established method to estimate bulk flows with Type Ia Supernovae (SNeIa) in Section 2.3 that we use in Chapter 6 with simulated SNeIa sample. We review and compare in Section 2.4 bulk flow measurements with multiple probes.

2.1 Cosmological observables

In section 1.1, we introduced the redshift as a fundamental observable of objects at cosmological distances. The redshift depends only on the scale factor at the time of light emission, it cannot be used to determine cosmological parameters by itself. We need to compare to other quantities depending on the cosmological parameters, quantities which will be presented below.

2.1.1 Distances

Because of the expansion of the Universe, distances between observers (like us) and celestial objects cannot be measured directly. There are multiple definitions of distance depending on the nature of observation used. There are detailed in the following.

Comoving distance along the line of sight (d_C)

The comoving distance between two objects remains invariant of the expansion of the universe. It is related to the proper distance, the distance between the two objects measured with a ruler at a given epoch, which increases with the scale factor a (defined in 1.1.2), so proportional to $(1+z)^{-1}$, while the comoving distance remains the same at all epochs. The radial (or line-of-sight) comoving distance d_C can be calculated by integrating over Hubble expansion since the time of emission at a redshift of z :

$$d_C(z) = d_H \int_0^z \frac{dz'}{E(z')}, \tag{2.1}$$

where $E(z) = H(z)/H_0 = \sqrt{\Omega_r(1+z)^4 + \Omega_m(1+z)^3 + \Omega_K(1+z)^2 + \Omega_\Lambda}$ is the normalised Hubble parameter and $d_H = c/H_0$ is the Hubble distance.

Angular diameter distance (d_A)

d_A is defined as the ratio between the physical diameter D of an object and its apparent angular diameter $\delta\theta$:

$$d_A = \frac{D}{\delta\theta}. \tag{2.2}$$

d_A measures the separation of two objects at the same redshift and is related to the transverse comoving distance d_M which is identical to the line-of-sight comoving distance d_C for a flat universe. Within ΛCDM, we have:

$$d_A = \frac{d_C}{(1+z)}. \tag{2.3}$$

Since this distance measures the proper size of an object (or the separation between two objects at the same redshift), it is used with observing *standard rulers*, which are objects or structures of known size like the Baryon Acoustic Oscillations (BAO). BAO are imprint of the matter density fluctuations caused by oscillations of the baryon-photon plasma in the early universe.

Luminosity distance (d_L)

The luminosity distance (d_L) is defined by the ratio of the observed flux F of a light source to its intrinsic luminosity L:

$$d_L = \sqrt{\frac{L}{4\pi F}}. \tag{2.4}$$

Since the objects are evolving in an expanding universe, we have to take into account the effects of the cosmic expansion as the photons propagate from the source to the observer. The expansion results in:

- the photons loose energy during their propagation $\propto (1+z)$,

- the photons arrive less frequently $\propto (1+z)$, compared to the frequency of their emission.

Therefore, the luminosity distance d_L is different from the comoving one d_C like following

$$d_L = (1+z)d_C = (1+z)^2 d_A. \tag{2.5}$$

We can express the luminosity distance as a function of the cosmological parameters:

$$d_L(z) = d_H(1+z)\int_0^z \frac{dz'}{E(z')}, \tag{2.6}$$

recalling that $E(z)$ is function of the Ω_i cosmological parameters.

The luminosity distance is used to compare the flux of *standardisable candles*, objects of known luminosity, to their redshift and thereby determine cosmological parameters. The term standard candles is commonly applied to Type Ia Supernovae (SNeIa), which we introduce in Chapter 5 and use as distance indicators in 2.3 to present bulk flows detection and in Chapter 6 to estimate the detectability of bulk flows with ZTF-like simulated data set. We can include Cepheids and galaxies amongst the objects with a well known relation between their luminosity and other properties.

2.1.2 Distance modulus

In astronomy, a source brightness is commonly expressed in terms of magnitude, more details can be found in Chapter 4. The magnitude depend on the relative measured flux f of objects in comparison to a reference star flux f_0. The apparent magnitude m of that object is defined as :

$$m - m_0 = -2.5\log_{10}\frac{f}{f_0}, \tag{2.7}$$

where m_0 is the magnitude of the reference star. Historically, Vega (α Lyrae) was used as the reference star and thus its magnitude is set to $m_0 = 0$. The absolute magnitude M is defined as the value that the apparent magnitude would have if the object were located at 10 pc; and the distance modulus μ is defined as the difference between m and M:

$$\mu \equiv m - M = 5\log_{10}\left(\frac{d_L}{10\text{pc}}\right), \tag{2.8}$$

with the luminosity distance d_L expressed in pc.

The distance modulus is related to the distances of standard candles and extensively referred to in Chapter 5.

2.1.3 Peculiar Velocities

As introduced in 1.1.2, the cosmological redshift $\bar{z}$ is due to the expansion of the universe only. Peculiar velocities from the galaxies produce an additional Doppler effect, which should be accounted for. In practice, redshifts are measured in the heliocentric referential, they are referred to as z_{hel} (Davis and Scrimgeour 2014):

$$(1 + z_{hel}) = (1 + \bar{z})(1 + z_{pec})(1 + \mathrm{z}_{\odot}), \tag{2.9}$$

where $\bar{z}$ is the cosmological redshift defined by Equation (1.6); $\mathrm{z}_{\odot} = \mathrm{v}_{\odot}{}^{r}/c$ is the redshift due to the sun velocity with respect to the CMB frame and z_{pec} is the one due to the peculiar motion of the galaxy. The redshift in the CMB frame is, usually, expressed as :

$$1 + z = \frac{1 + z_{hel}}{1 + \mathrm{z}_{\odot}}, \tag{2.10}$$

and therefore:

$$1 + z = (1 + \bar{z})(1 + z_{pec}). \tag{2.11}$$

This equation shows the decomposition of the redshift in two components: Hubble flow and peculiar velocities. The peculiar velocities involve Doppler effects which gives at first order and using the convention $c = 1$:

$$1 + z = (1 + \bar{z})(1 + (\mathbf{v}_e - \mathbf{v}_0) \cdot \mathbf{n}) \tag{2.12}$$

where $\mathbf{v}_e$ and $\mathbf{v}_0$ are, respectively, the peculiar velocities of the emitter and the observer and $\mathbf{n}$ is the unit vector from the observer to the emitter. The first order effects of peculiar velocities on d_L were derived in Hui and Greene 2006. Furthermore, the apparent angular diameter $\delta\theta$ changes, because the velocity of the observer introduces a stellar aberration effect which affects the angular diameter distances. In the following equations perturbed quantities will be noted with a tilde:

$$\delta\tilde{\theta} = \delta\theta(1 - \mathbf{v}_0 \cdot \mathbf{n}) \tag{2.13}$$

$$\Rightarrow \quad \tilde{d}_A(z) = d_A(\bar{z})(1 + \mathbf{v}_0 \cdot \mathbf{n})\,, \tag{2.14}$$

Combining the last equation with Equation (2.5), the perturbed luminosity distance becomes:

$$\tilde{d}_L(z) = d_L(\bar{z})(1 + (2\mathbf{v}_e - \mathbf{v}_0) \cdot \mathbf{n}). \tag{2.15}$$

The Taylor series expansion of Equation (2.6) at first order gives

$$\tilde{d}_L(z) = d_L(\bar{z}) \left\{ 1 + \left[1 + \frac{(1 + \bar{z})^2}{d_L(\bar{z})H(\bar{z})} \right] (\mathbf{v}_e - \mathbf{v}_0) \cdot \mathbf{n} \right\}. \tag{2.16}$$

Finally, inserting Equation (2.16) in Equation (2.15) gives the expression of the perturbed luminosity distance as a function of the observational redshift z

$$\tilde{d}_L(z) = d_L(z) \left[1 + \mathbf{v}_e \cdot \mathbf{n} - \frac{(1 + \bar{z})^2}{d_L(\bar{z})H(\bar{z})} \right]. \tag{2.17}$$

Peculiar velocities in the universe

The universe today is locally inhomogeneous: it is filled with stars, galaxies and clusters of galaxies. As for the growth of these structures, the force of gravity is responsible for all the

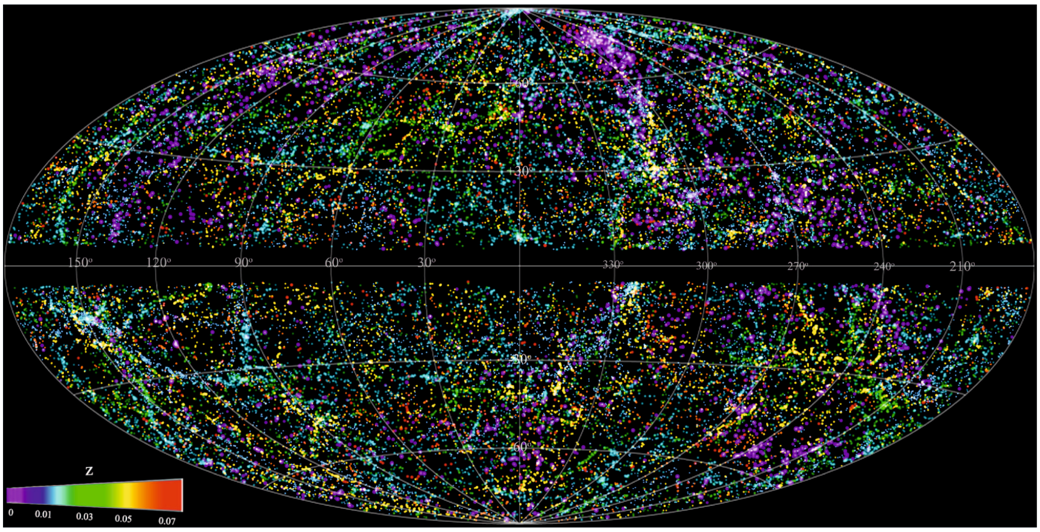

Figure 2.1: Distribution of all the 2MASS galaxies survey in Galactic coordinates, colored by redshift, from Macri et al. 2019

peculiar motions of these objects we notice today. Fig 2.1 shows all the local, up to $z \sim 0.7$ known structures associated to their peculiar velocities from Macri et al. 2019.

These peculiar motions are, for some, non-negligible like the motion of our Local Group (LG) which exceeds $600\ \mathrm{km\,s^{-1}}$. If such large velocities are measured, it indicates an infall to more massive regions like groups of galaxies. Answering to this question consists on mapping the field of density matter all around us, it would contribute to discover new structures and test our model of gravity. Many efforts over the years were deployed to understand and reconstruct the origin of this motion (Jerjen and Tammann 1993; Tully et al. 2014; Kocevski et al. 2007). As an example of the results of these studies, we know from Kocevski et al. 2007 that part of the LG velocity is caused by infall toward Shapeley super-cluster centred at a distance of $\sim 200\ \mathrm{Mpc}$, corresponding to $z \sim 0.046$.

In early studies, galaxies with their distance brightness relationship (Tully and Fisher 1977) were widely used to probe peculiar velocities and to measure the coherent motions. In the last decade, SNeIa as Standard Candles (more details in Chapter 5), became also probe of the matter density with the increasing number of data sets. SNeIa are standardised more accurately than galaxies, $\sigma_d \sim 15 - 25\%$ for galaxies against $5 - 8\%$ for SNeIa. The other advantage of SNeIa is that they can be observed to distances far beyond the local structure, when galaxies data become sparse and noisy, which allows to map the matter distribution up to $z > 0.1$.

Another probe of anisotropies is the Sunyaev-Zel'dovich (SZ) effect, first introduced in Zeldovich and Sunyaev 1969 which is a distortion in the CMB spectrum. It is of major interest and used to determine the Hubble constant H_0, locate new galaxy clusters and study of mass distribution. SZ-effect originates from CMB photons passing through hot plasma in galaxy clusters causing the photons to scatter and gain more energy. In fact, the effect described is a first-order one and due to the temperature (tSZ), there is a second-order effect, a kinetic one (kSZ) due to the bulk motion of the galaxies. Measurements of the kinetic component of SZ effect are correlated to large-scale peculiar motions and can be used to detect coherent motion.

2.2 Bulk flows: theoretical concept

The matter velocity field is, by definition, the temporal derivative of the spatial position $\mathbf{r} = a\chi$ with χ the 3D comoving coordinates

$$\mathbf{u} = \dot{\mathbf{r}} = \mathbf{V} + \mathbf{v}. \tag{2.18}$$

In this expression, $\mathbf{V} = H\mathbf{r}$ is the Hubble flow while $\mathbf{v} = a\dot{\chi}$ is the peculiar velocity field.

In the framework of linear theory of structure formation, the velocity field $\mathbf{u}$ is linked to the density field δ by the equation 1.29 giving in Fourier space

$$\mathbf{v}_k = iHf\delta_k \frac{\mathbf{k}}{k^2}, \tag{2.19}$$

where δ_k is the Fourier transform of the density field.

The variance of the velocity field can be computed, as for the matter fluctuation parameter σ_8, by averaging the velocity field two-point correlation function

$$\sigma_v^2 = \frac{H^2 f^2}{2\pi^2} \int P(k)|W(k,R)|^2 dk. \tag{2.20}$$

A well adapted all-sky filter function is the Gaussian one (Scrimgeour et al. 2015): $W(k,R) = \exp(-k^2R^2/2)$. Within the ΛCDM, the typical velocity field fluctuations, called bulk flow in the following, are shown in Fig 2.2 for low redshifts (using the matter power spectrum $P(k)$ from CLASS [1] Blas, Lesgourgues, and Tram 2011). The typical bulk flow effects expected are of the order of $300\ \mathrm{km\,s^{-1}}$ in the local universe.

Bulk flow detection of amplitudes significantly higher than the predictions would indicate

a higher range of anisotropy than expected for the given scale and thus a sign of physics beyond the standard model of cosmology (ΛCDM). It would imply that whether the assumption of homogeneity and isotropy in ΛCDM is not verified, or that ΛCDM model is not complete (new physics content, effects beyond General Relativity).

2.3 Measuring bulk flows with Type Ia Supernovae: methodology

One of the simplest anisotropy model is a peculiar velocity dipole, which corresponds to a *bulk flow*. Bulk flows are average coherent motion of matter in a region of space, relative to the Cosmic Microwave Background (CMB) frame, and are induced by peculiar velocities of galaxies. Bonvin, Durrer, and Kunz 2006 expressed the effect of anisotropy as the angular power spectrum of fluctuations of the luminosity distance. The luminosity distance (d_L) of

---

[1] `http://class-code.net`

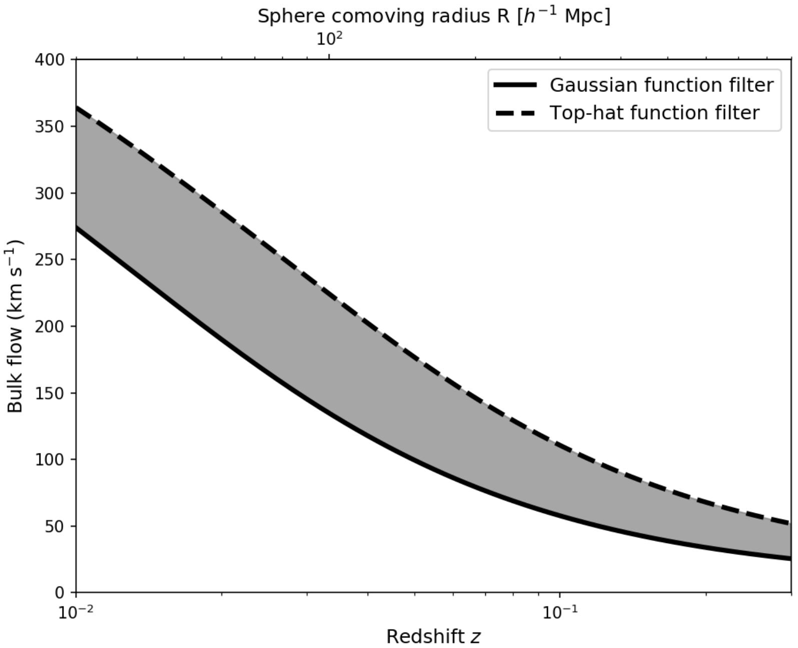

Figure 2.2: Velocity field fluctuations, or bulk flow, expected within ΛCDM as a function of the redshift or the comoving radius with two different filter functions: a Gaussian function (solid line) and a top-hat function (dashed line).

Standard Candles like SNeIa, introduced in 2.1.1, can be expressed with a dipole anisotropy using Equation (2.17) with $\mathbf{v}_e = 0$, i.e. with the assumption that the dipole effect is produced by the peculiar velocity of the observer:

$$\tilde{d}_L(z) = d_L(z) + d_L^{(1)}(z), \tag{2.21}$$

where

$$d_L^{(1)}(z) = \frac{(1+z)^2}{H(z)}\mathbf{n}.\mathbf{v}_d. \tag{2.22}$$

In this last equation, we recall that $H(z)$ stands for the expansion rate of the universe defined in Equation (1.27) , $\mathbf{n}$ refers to the unit vector of the observed object's position and $\mathbf{v}_d$ is the dipole velocity vector. We use this technique in Chapter 6 to estimate the detectability of bulk flows with ZTF-like SNeIa simulations. We describe the methodology to estimate the dipole velocity v_d and its location in Section 6.3.1 of the same chapter.

In addition to peculiar velocity measurements, we can test the isotropy and homogeneity of the universe using more general anisotropies. Colin et al. 2011 used a statistical method based on weighting the Hubble residuals of SNeIa based on their location. This method is referred to as smoothed residuals; it detects regions where the SNeIa are in average brighter or fainter. The dipole estimation described above can be used afterwards to constrain the bulk flow velocity. Colin et al. 2011; Feindt et al. 2013 used this technique to constrain local bulk flows, the results of their studies are presented in 2.4. In Mathews et al. 2016, they looked for a cosine dependence of the deviation from Hubble flow, in addition to the dipole fit. Another test of isotropy is to look at the directional variations of the Hubble expansion, like in Kalus, B. et al. 2013, they looked at the difference in the expansion rate on opposite hemispheres based on SNeIa data and found it consistent with ΛCDM predictions. Moreover, isotropy of the cosmic expansion was investigated in Colin et al. 2019, based on the methodology of Nielsen, Guffanti, and Sarkar 2016, no conflict with ΛCDM was shown.

2.4 Bulk flow measurements: current results

As stated above, evidence of a coherent bulk flow towards the Shapely super-cluster at a distance of ~ 200 Mpc has been observed. This local anisotropy can be perceived as a local perturbation within FLRW universe. The biggest question is whether the bulk amplitude converges to ΛCDM model predictions. Larger coherent motions, at higher scales, were detected in a study (Kashlinsky et al. 2010), some other studies did not recover the same motion amplitude. Bulk flows can be measured with multiple probes, in the local and large scales, introduced in Section 2.1.3. Table 2.1 summarises the bulk flow measurements from three probes at multiple scales. At small scales galaxies and SNeIa are used and kinetic Sunyaev-Zel'dovich (kSZ) effect is used at larger scales to map the matter distribution.

Table 2.1: Summary of bulk flow measurements

Reference	Obj.Type	No.Obj.	Redshift	Distance (h^{-1} Mpc)	v_{bf} $\mathrm{km\,s^{-1}}$	l ($\circ$)	b ($\circ$)	Notation
				Local measurements				
Colin et al. 2011	SNeIa	142	< 0.06	< 175	260 ± 130	298 ± 40	8 ± 40	$C11$
Turnbull et al. 2012	SNeIa	245	< 0.05	< 145	245 ± 76	319 ± 18	7 ± 14	$T12$
Feindt et al. 2013	SNeIa	128	$0.015 - 0.035$	$45 - 108$	243 ± 88	298 ± 25	15 ± 20	$F13$
		36	$0.035 - 0.045$	$108 - 140$	452 ± 314	302 ± 48	-12 ± 26	
		38	$0.045 - 0.06$	$140 - 188$	650 ± 398	359 ± 32	14 ± 27	
		77	$0.06 - 0.1$	$188 - 322$	105 ± 401	285 ± 234	-23 ± 112	
Ma and Scott 2013	galaxies	2404	< 0.026	< 80	340 ± 40	280 ± 8	5.1 ± 6	$M13$
Mathews et al. 2016	SNeIa	191	< 0.05	< 145	326 ± 54	275 ± 15	36 ± 13	$M16$
		61	$0.05 - 0.15$	$145 - 405$	431 ± 587	125 ± 65	38 ± 37	
		388	> 0.05	> 145	456 ± 320	180 ± 350	65 ± 41	
Scrimgeour et al. 2015	galaxies	8885	0.016	50	248 ± 58	318 ± 20	40 ± 13	$S16$
		8885	0.023	70	243 ± 58	318 ± 20	39 ± 13	
Boruah, Hudson, and Lavaux 2020	SNeIa	465	0.015	40	252 ± 11	293 ± 5	14 ± 5	$B20$
Qin et al. 2021	galaxies	9790	0.012	35	376 ± 23	298 ± 3	-6 ± 3	$Q21$
				Large scale measurements				
Kashlinsky et al. 2010	kSZ	516	< 0.12	< 345	934 ± 352	282 ± 34	22 ± 20	$K10$
		547	< 0.16	< 430	1230 ± 331	292 ± 21	27 ± 15	
		694	< 0.20	< 540	1042 ± 295	284 ± 24	20 ± 16	
		838	< 0.25	< 640	1005 ± 267	296 ± 29	39 ± 15	
P. A. R. Ade et al. 2014	kSZ	1743	< 0.5	< 2000	< 254	...	...	$P14$

Fig 2.3 shows the bulk flow measurements from galaxies and SNeIa, they are overall around ΛCDM prediction (see 2.2 calculated from gaussian window function). At $z < 0.05$, we have measurements from both galaxies (Ma and Scott 2013; Scrimgeour et al. 2015; Qin et al. 2021) and SNeIa (Turnbull et al. 2012; Mathews et al. 2016; Boruah, Hudson, and Lavaux 2020; Feindt et al. 2013), they are all in agreement or close to ΛCDM predictions. We can notice a difference in the uncertainties of the measurements, Boruah, Hudson, and Lavaux 2020 measurement displays the smallest uncertainty, they compared the reconstructed velocity

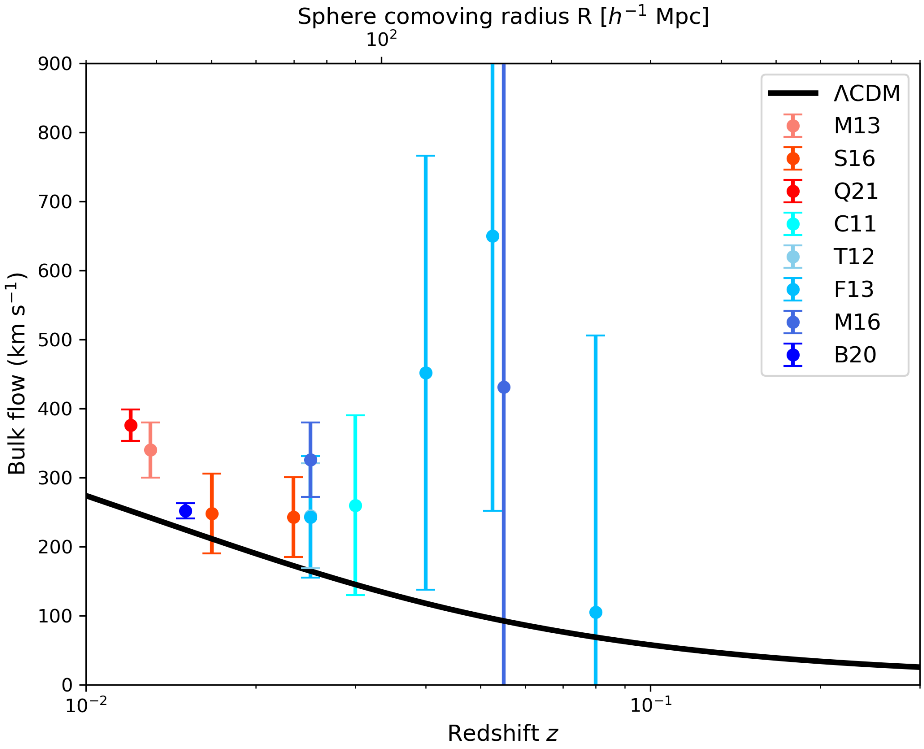

Figure 2.3: Comparison of the bulk flow measurements from different surveys and probes presented in Table 2.1. The black solid line is the ΛCDM prediction calculated from a Gaussian window function.

field of the 2M++ galaxy redshift catalogue (Carrick et al. 2015) to the measured peculiar velocities of 465 SNeIa. At $z > 0.05$, we have measurements only from SNeIa, they are consistent and within ΛCDM predictions. They all show high uncertainty values which can be due to the sparsity and inhomogeneity of the sample used, robustness of the inference method and more generally the increasing uncertainties from SNeIa distance measurements with increasing redshifts. All the inferred coordinates point toward the same direction, the location of CMB dipole (Kogut et al. 1993; Planck Collaboration et al. 2020).

At large scales, using the kSZ effect, Kashlinsky et al. 2010 claimed the existence of a coherent motion of $\sim 1000\ \mathrm{km\,s^{-1}}$ up to a comoving distance $640\ h^{-1}$ Mpc. This velocity is well above the expected value from ΛCDM. Later, using the same kSZ effect, P. A. R. Ade et al. 2014 found no evidence of such large-scale bulk flows, the constraints on the amplitude set at $< 254\ \mathrm{km\,s^{-1}}$ for comoving distances $< 2\ h^{-1}$ Gpc. This measurement is compatible with ΛCDM predictions, indicating that the Universe is homogeneous on Gpc scales. We can note that the measurements from (P. A. R. Ade et al. 2014), at small scales, were not sensitive enough in the local universe to test isotropy at these scales and compare it to other probe measurements.

Combining the local measurements, we can see that they are all in broad agreement. When SNeIa are used as a probe, the measurements display large uncertainties. The measurements are noisy, this can be due to the samples low statistics, especially when the number of SNeIa is compared to galaxies. The other contribution to the large uncertainties is the sample composition, they are constituted of objects from several surveys with different systematic uncertainties. As presented in Section 2.1.3, SNeIa show great advantages in their use to probe the local density matter. The only missing piece toward precision estimation of bulk flows with SNeIa is to have a large and homogeneous sample with known selection effects. With only three years of ZTF observations, we have an homogeneous sample of ~ 3700 spectroscopically confirmed SNeIa (more details in 3.2), which is already larger than the samples listed in Table 2.1. The characterisation of the selection function of this sample was investigated in the context of this thesis and is detailed in Chapter 7.1.3.

CHAPTER 3

THE ZWICKY TRANSIENT FACILITY

All the thesis work was based on the Zwicky Transient Facility (ZTF) data Bellm et al. 2018; Graham et al. 2019. ZTF is a wide-field optical survey of the northern sky, limited to $\delta \gtrsim -30°$, it started in March 2018. ZTF has two observing phases: phase I ($2018 - 2020$) and phase II ($2020 - 2023$). It is an international collaboration divided into working groups focusing on a broad range of time-domain and transient science : Solar System Bodies, Galactic Science, Multi-Messenger Astronomy, Active Nucleus and Tidal Disruption events, Physics of Supernovae & Relativistic Explosions and Cosmology. My work stands in the SNeIa Cosmology working group. In this chapter, we first present the survey design, observing and classifying strategy. We then introduce the ZTF Data Release 2 (DR2) sample of Type Ia Supernovae observed during ZTF phase I, with its general characteristics. This sample will be the baseline of our realistic simulation pipeline presented in Chapter 7.

3.1 Overview of the experiment

3.1.1 Survey design

ZTF is the latest transient survey. It is using the 48-inch Schmidt telescope (P48), mounted at Mount Palomar Observatory and equipped with a new 576 megapixel camera. It observes through three filters: *ztfg*, *ztfr* and *ztfi*, their transmission functions are represented in Fig 3.1. The camera consists of 16 CCDs[1], as detailed in Dekany et al. 2020a. Each CCD is subdivided into four read-out channels, as shown in Fig 3.3. Hereon we shall refer to these read-out channels as CCD-quadrants. Therefore, each ZTF exposure consists of 64 CCD-quadrants, one image corresponds to one CCD-quadrant.

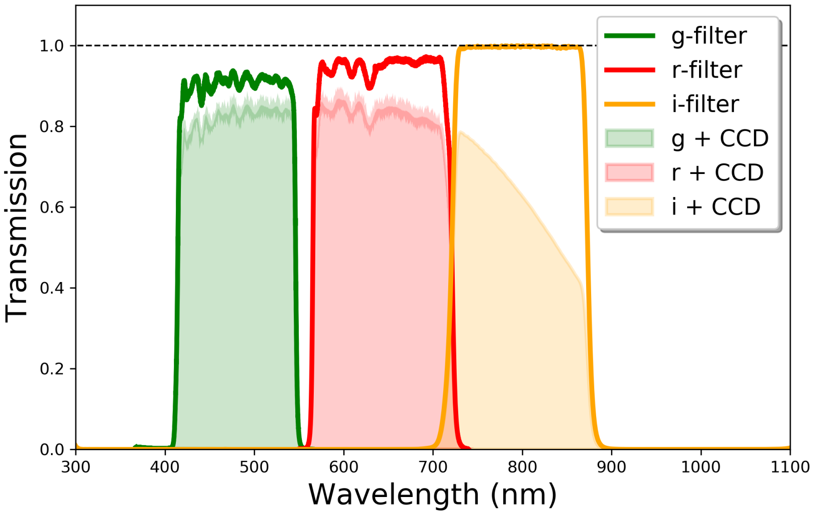

Figure 3.1: ZTF filter transmissions alone as a function of wavelength (bold lines) and with CCD quantum efficiency (filled lighter colors).

The ZTF camera has a field of view of 47 square degrees (see Fig 3.2), which enables to scan the whole northern sky every two nights. Long exposures allow to make deep observations,

---

[1] Charged Coupled Devices.

however it is at the cost of the size of the observed areas. Deep observations would cover small areas which is inconvenient for transient discoveries. ZTF observing strategy is a balanced combination between cadence and depth. With an exposure time of 30 seconds, ZTF survey is able to cover the majority of the visible sky and maximises the number of transient discoveries.

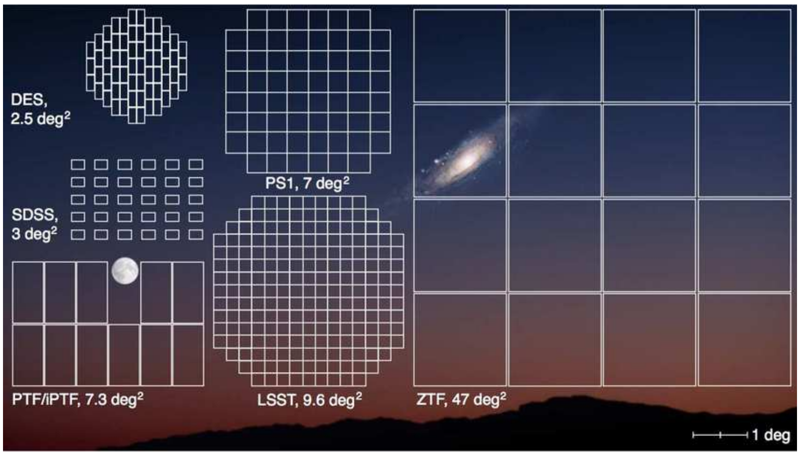

Figure 3.2: ZTF camera Field of View (FoV) compared to past and future survey cameras. Each square is one CCD. The apparent galaxy is Andromeda. Figure from Laher et al. 2017.

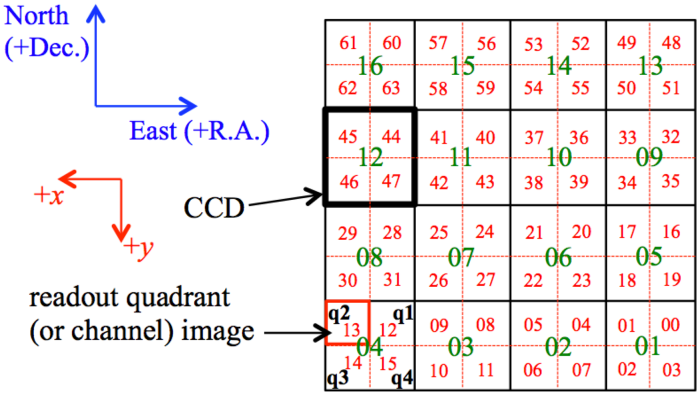

Figure 3.3: ZTF focal plane showing CCD IDs in green and CCD-quadrant IDs in red. The x, y vectors denote the directions of the increasing pixel coordinates that all readout quadrants must have when the Field of View (FoV) is orientated on the sky equatorial coordinates: right-ascension (RA) and declination (Dec). Figure from Masci et al. 2018.

3.1.2 Survey strategy

During ZTF phase I, the survey was divided in three main programs according the following time sharing Bellm et al. 2018: 40% of public surveys proposed to the National Science Foundation (NSF) and called Mid-Scale Innovations Program (MSIP), 40% for the ZTF Collaboration survey and 20% dedicated to Caltech surveys.

All data acquired during public time are publicly available and are observed only on *ztfg* and *ztfr* bands, *ztfi* band data are private. All detected sources passing the ZTF Alert Distribution System Patterson et al. 2019 are given ZTF names of the format : *"ZTFYYletters"*, where "YY" is the year of discovery and "letters" number-like identity (for instance ZTF20aajnksq). Events from the same location have the same name. Since the beginning of the survey $500.000.000$ alerts have been recorded, accordingly to IPAC [2] alert system.

Survey cadence

ZTF observing strategy is based on a fixed sky grids, each element of the grids is known as a field, identified by its field number and corresponding to ZTF footprint on the sky. ZTF has two grids, the "main" and "secondary" grids which are slightly shifted. They are respectively used 89% and 11% of the total observing time. The main grid is represented in Fig 3.4. The secondary grid is shifted, regarding the main one, by about half of a field to ensure that CCDs ship gaps are covered. This secondary grid is useful for calibration purposes.

Survey magnitude limit

The limiting magnitude, also known as the 5σ-limit depth, corresponds to the faintest magnitude of the observation at 5σ above the background level. Limiting magnitudes of ZTF observations are derived for each observation and computed by IPAC through the IPAC pipeline digesting the raw images to produce calibrated science images (more details can be found in 7.1.2 and in Masci et al. 2018). The median limiting magnitude values for 30 seconds exposures are 20.8 mag and 20.6 mag in respectively *ztfg* and *ztfr* bands (Masci et al. 2018). They are subject to seasonal variations due to their dependence on observing conditions.

3.1.3 Spectroscopic follow-ups and BTS program

ZTF has discovered about 50.000 transient events since it started. The survey is a transient detection machine. However, to understand and study transient events, we need to know the classification and redshift of every object. To this purpose, spectroscopy is required. Most transient objects detected by ZTF display magnitudes at the survey magnitude limit, thus they are unobservable without a very large telescope. ZTF has a dedicated working group in charge of bright sources classification, it is the Bright Transient Survey BTS (Fremling et al. 2019; Perley et al. 2020). It uses allocated observing time from multiple telescopes to classify bright transients discovered by ZTF. Among the telescopes used to classify ZTF discoveries, there is the P60 telescope of the Mount Palomar Observatory, in which an Integral Field Spectrograph "SED machine" (SEDm) (Blagorodnova et al. 2018; Rigault et al. 2019) is mounted and dedicated to ZTF follow-up. The SEDm has a 28×28 arcsec^2 field-

---

[2] IPAC is the Caltech science and data center for astrophysics and planetary sciences.

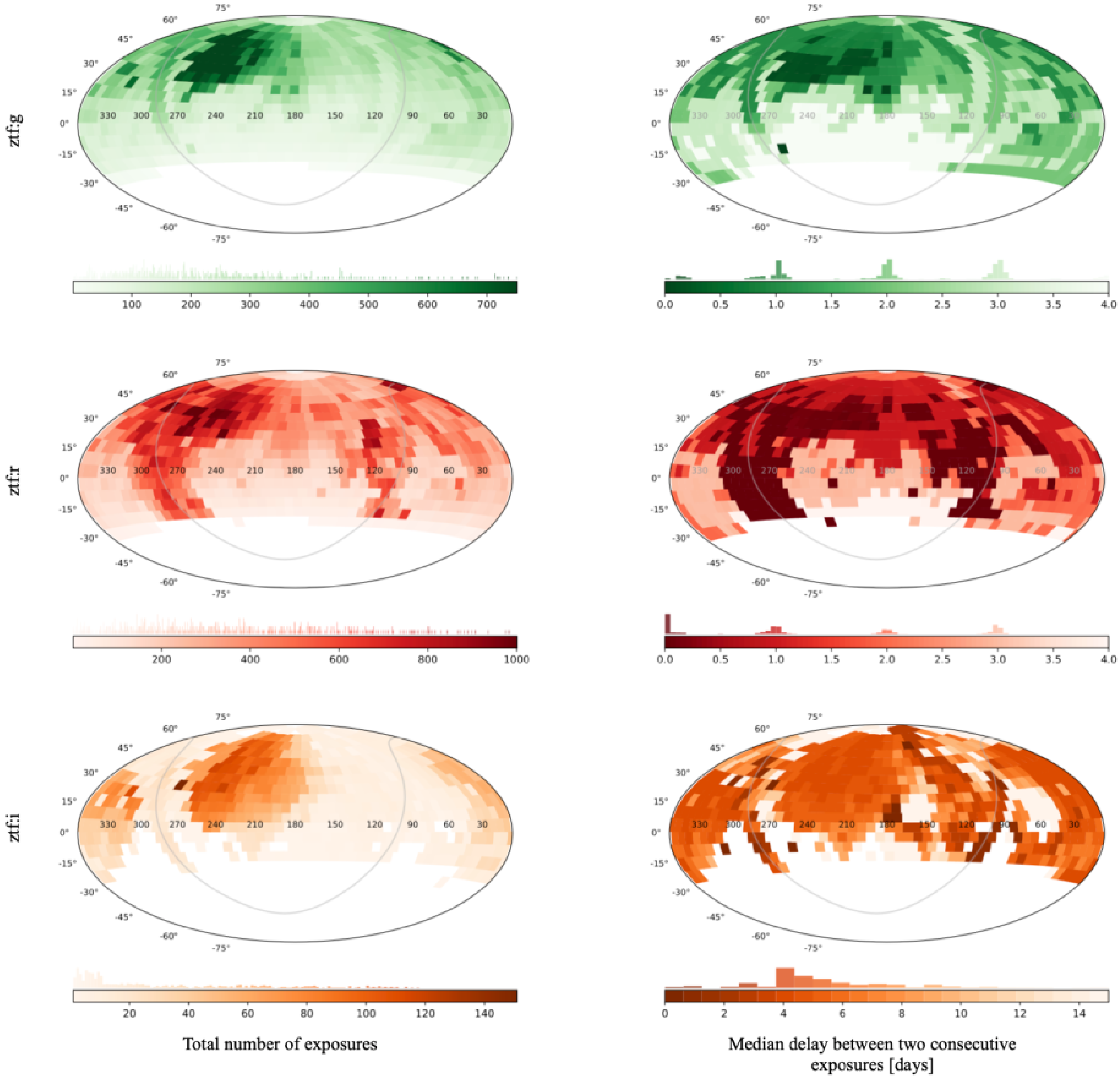

Figure 3.4: ZTF phase-I main grid cadence statistics per field and per filter. The grey line represents the Milky Way location. The densely observed region located around right ascension $\alpha = 240$ and declination $\delta = +30$ are the high cadence fields. **Left:** Number of exposures. **Right:** Median delay between two consecutive exposures illustrating the cadence sampling of transient light-curves acquired by ZTF. **From top to bottom:** g, r and i bands of ZTF. *Credit : Rigault, M.*

of-view filled by ~ 1300 hexagonal micro-lenses (spaxels). These lenses converge the light onto multi-prism that provides low-resolution spectra spanning from 4000 Å to 9000 Å.

BTS performances

In Fig 3.5, we have the sky-map of transients discovered by ZTF and classified by BTS, from the beginning of the survey to August 2022, across the northern sky. BTS has classified 6763 transients over 10462 submitted to classification. BTS spectroscopic classification is based on selection in transient peak brightness and light-curve sampling, further details can be found in Perley et al. 2020 and Section 7.4.2 in this manuscript. Fig 3.6 represents the peak magnitudes in any ZTF band (*ztfg* or *ztfr*) of transients classified by BTS (in green), thus transients passing the selection, and non-classified transients (in red) that failed the selection cuts. We can notice that most of the non-classified objects are the faintest, their peak magnitudes stand in the range $[18.5, 19]$.

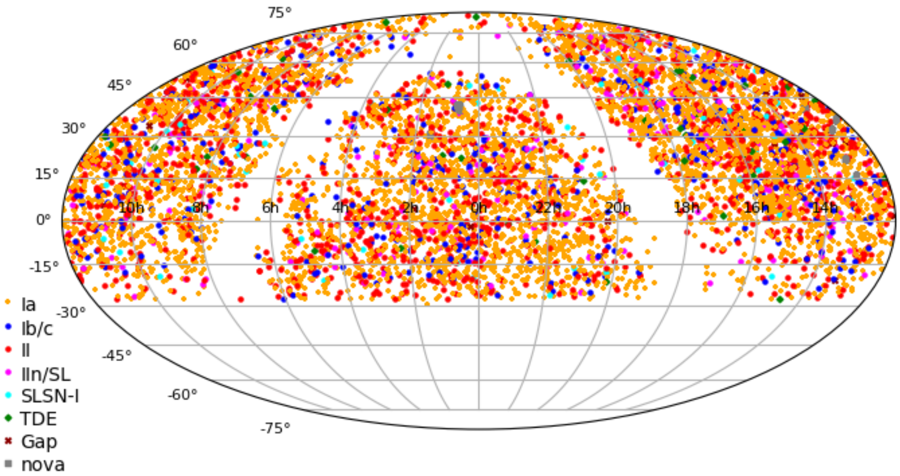

Figure 3.5: Skymap of BTS classified transients covering observations period from the start of the survey until August 2022. *Credit: BTS Working Group.*

Other transients discovered by ZTF are spectroscopically followed-up by other ZTF programs (infant SNe, superluminous SNe, superfast SNe) and external surveys like ePESSTO (extended-Public ESO Spectroscopic Survey for Transient Objects, YSE (Young Supernovae Experiment), NUTS (Nordic optical telescope Unbiased Transient Survey). All public data available are used by SNeIa working group.

3.2 The ZTF DR2 sample

ZTF has been running for more than four years, since March 2018. The first year SNeIa sample is known as the DR 1 sample, it was published in Dhawan et al. 2021, with 761 spectroscopically confirmed SNeIa. More details can be found in Section 6.1. The main focus of my work is on the ZTF DR 2. This sample collects all spectroscopically confirmed SNeIa from ZTF phase I. The data is gathered from internal and external surveys. Each

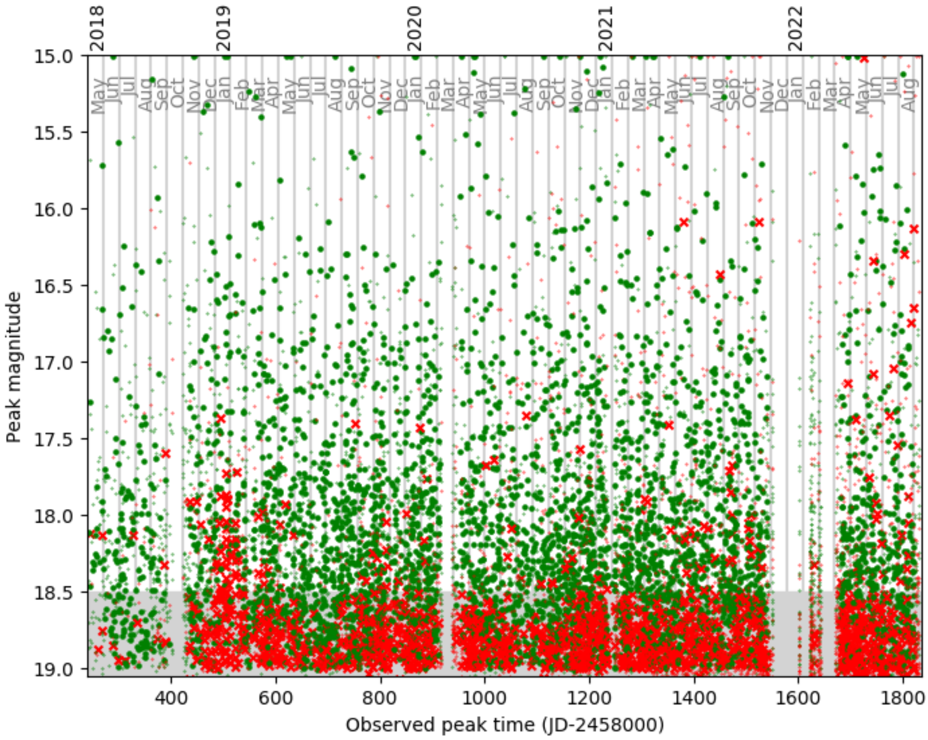

Figure 3.6: Peak brightness of BTS transients, in function of their observed peak time. The green data points are the classified ones, associated to the ones in Fig 3.5, whereas the red ones are the non-classified ones. *Credit: BTS Working Group.*

spectroscopic classification is confirmed using the typing application[3] developed by Rigault, M.

At the time the present manuscript is being written, DR2 sample construction is still under ongoing efforts. All the numbers provided about the sample are subject to change, the final ones will be reported in *Rigault et al. in prep.*

3.2.1 Sample description

The DR2 sample consists of ~ 3700 spectroscopically confirmed SNeIa. Fig 3.7 represents the cumulative evolution of the number of SNeIa during ZTF I. The blue dashed line corresponds to the number of spectroscopically classified SNeIa and the solid one is associated to the ones with host galaxy spectroscopic redshifts. The orange colored lines correspond to the SNeIa passing some cosmological quality cuts, with the dashed one for all spectroscopically confirmed SNeIa and the solid one to spectroscopically confirmed SNeIa with host spectroscopic redshifts. The cosmological quality cuts cover, from *Rigault et al. (in prep)*:

- Light-curves sampling: at least two detections at $\geqslant 5\sigma$ level flux prior and posterior to the maximum of light, in at least two ZTF bands and at least 7 points in total in all bands.

---

[3] `https://typingapp.in2p3.fr/`

- Light-curves parameters cuts: stretch range $[-4, +4]$ and color $[-0.3, 0.8]$. These light-curves parameters are further explained in Chapter 5.

More details about cosmology quality cuts can be found in the ZTF DR 2 paper *Rigault et al. (in prep).*

Within all classified objects, there are also peculiar SNeIa that can be identified by spectral properties and be can either sub or super luminous than regular ones. Among these objects, there are SNe Ia91bg (sub-luminous) and Ia91T (over-luminous). Efforts are ongoing about identifying peculiar SNeIa in the DR2 sample and removing them. We also discuss this contamination in Section 7.4.3, when we use realistic simulation framework to reproduce the DR2 sample.

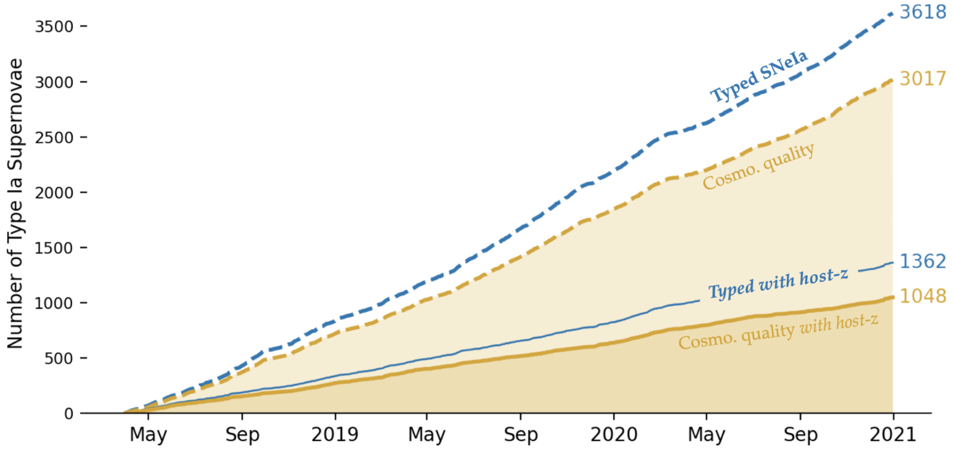

Figure 3.7: Cumulative number of SNeIa observed during ZTF phase I. In blue, we have all the spectroscopically classified SNeIa, the ones with host-galaxy redshifts in dashed lines. In orange, we have the spectroscopically classified SNeIa that passed the cosmological cuts from Section 3.2.1, the ones with host-galaxy redshift in dashed line. Preliminary figure from *(Rigault et al. in prep).*

3.2.2 Redshifts and classifications

A majority ($\sim 80\%$) of ZTF classifications come from the SEDm, through BTS, as shown in Fig 3.8. The figure also displays the other sources of ZTF DR2 spectra. The SEDm spectra for this data release were extracted using a new method "hypergal" from *Lezmy et al. in prep*, which optimally separates the host-galaxy and it transient signals.

The DR2 redshifts are obtained by matching SNeIa positions to redshift catalogues, in particular SDSS (Sloan Digital Sky Survey), NASA-IPAC Extragalactic Database (NED) and SIMBAD Astronomical Database with an associated uncertainty up to $\sigma_z = 10^{-4}$. If no redshift is found, the one used is the best fitting template of the spectrum, through SNID (Supernova Identification, Blondin and Tonry 2007), with an associated uncertainty of $\sigma_z = 2\times10^{-3}$. According to *Rigault et al. (in prep)*, around 38% of the DR2 SNeIa have host galaxy redshifts, their distribution is in fig 3.9, filled histogram. The second histogram from the same figure represents the distributions of the whole DR2 sample, it displays a median values of $\bar{z} = 0.065$. As expected, the missing host-galaxy redshifts display the higher values. Discussions between ZTF groups and DESI (Dark Energy Spectroscopic Instrument) survey are in progress to complete these ZTF missing host-galaxy redshifts .

Figure 3.8: Distribution of the spectra of ZTF DR2 objects sorted by follow-up facilities. Most of the SNeIa are classified by the SED machine and are part of the BTS program. Figure from *Rigault et al. (in prep)*.

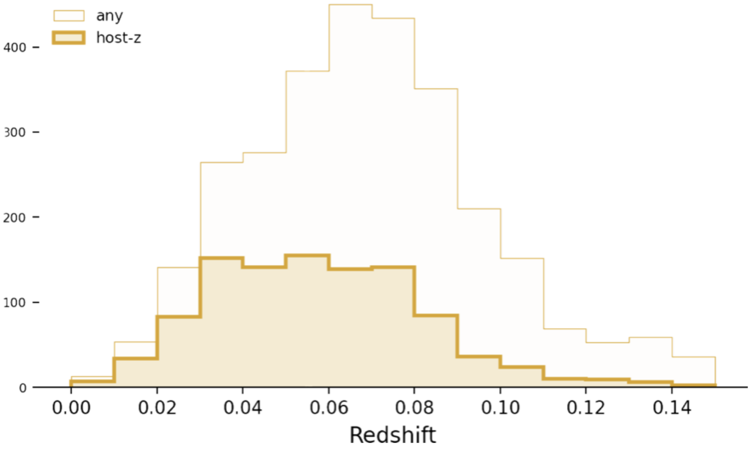

Figure 3.9: Redshift distributions of the whole DR2 sample and only SNeIa with host galaxy redshifts. Figure from *Rigault et al. (in prep)*.

3.2.3 Photometry

SNeIa are discovered using alert photometry. Each ZTF image is subtracted from a reference one, which is a stacked image of 15 to 40 high quality images (Masci et al. 2018), taken prior to the survey observations. Source extraction technique, Sextractor (Bertin, E. and Arnouts, S. 1996) is used to find all the sources in the image. Each detected source is cross-matched to previously detected sources in a 1.5 arcsec aperture (*from ZTF pipeline*). Any new source is given a ZTF name, all alerts are released to the wider community. For a given SNIa, alert photometry is only available at epochs when the SNIa is detected, the position is allowed to vary between epochs. Full details about the ZTF alert photometry in (Masci et al. 2018).

For the ZTF DR2 sample, SNeIa light-curves are derived using forced photometry. For a given SNIa, the median position of all alerts detection is computed. The PSF-flux is then measured, at this position, from the difference images for all epochs. This technique enables to recover detections that are otherwise missed by the real-time pipeline, and estimate the fluxes for all images, even when the SNeIa is not present. To correct for cases when the SNIa is found in the reference image, the median flux, from epochs when the SNIa is not present, is added to all epochs. Full details can be found in Yao et al. 2019. The implementation used to derive ZTF DR2 light-curves is available in the following github: `https://github.com/MickaelRigault/ztflc`.

Calibration for forced photometry is determined from IPAC pipeline, and is accurate at 2% flux level (Masci et al. 2018), more details can be found in Section 4. For the coming ZTF cosmology analysis, photometric measurements will be derived using scene modelling technique Holtzman et al. 2008 with sky calibration derived using ubercal method (Padmanabhan et al. 2008a). These techniques are actively being developed by IN2P3 groups. Forced photometry is used in all the results of Chapter 7.1.3.

3.3 Summary

ZTF is a transient detection machine, it discovers, follow-ups and classifies objects in the nearby Universe, observed in the Northern sky. Since its start, the survey has discovered over $50,000$ SNe. All transients brighter than ~ 18.5 mag are classified, 6000 SNe have been classified by the BTS program. The ZTF DR2 sample consists of ~ 3700 light-curves of spectroscopically classified SNeIa, each with a precisely measured redshift and a 2% level flux precision. This sample is key for SNeIa cosmology studies and can highly contribute to meet the challenges that the standard model of cosmology is facing, presented in Section 1.2.

CHAPTER 4

PHOTOMETRIC CALIBRATION

The biggest challenge for physics experiments is to relate a detector signal to the target physical quantity. For astronomical surveys it is also the case. The CCD camera, like the ZTF one described in Section 3.1, counts in Analog to Digital Units (ADU) in each pixel, a quantity proportional to the number of incident photons. This relationship needs to be calibrated to obtain physical fluxes (commonly expressed in erg $\mathrm{cm}^{-2}\,\mathrm{s}^{-1}$, with 1 erg $=$ 10^{-7} J) and magnitudes, in order to be compared to other survey physical fluxes for example, this is the role of the photometric calibration. As we stand in the era of precision SNeIa cosmology, photometric calibration is a critical and an increasingly important source of systematic uncertainties, as discussed in Section 5.3. Numerous surveys have focused their efforts on improving the calibration precision and target the 1% wich unlocks precision cosmology studies like the Dark Energy characterisation. Surveys like the Sloan Digital Sky Survey (SDSS) (Ivezić et al. 2007; Padmanabhan et al. 2008a), the Dark Energy Survey (DES) (Brout et al. 2019), the SuperNova Legacy Survey (SNLS) Regnault et al. 2009; Astier et al. 2013 and Pan-STARRS survey (Magnier et al. 2020) have tackled and succeeded to reach the 1% level precision
Knowing the importance of low-z SNeIa to cosmological studies, the critical missing piece for the ZTF sample to anchor high-z samples and unlock the most precise measurements to test ΛCDM model is the photometric calibration level. The current ZTF photometric calibration pipeline delivers a 2% level in flux (Masci et al. 2018), a lower level than required to contribute to resolve the tensions that ΛCDM is facing. In this chapter, we will introduce the notion of Zero Point (ZP) in photometry, the ZTF photometric calibration technique and the method we developed for the estimation ZTF with the associated results.

4.1 Intoduction to Zero Point in photometry

The observed magnitude m of an object whose flux is f, in a given magnitude system, like using a reference star flux f_0 and m_0 its magnitude, is written as :

$$\begin{aligned} & m - m_0 = -2.5\log\left(\frac{f}{f_0}\right) = -2.5\log f + 2.5\log f_0 \\ \Rightarrow\quad & m = m_0 + 2.5\log f_0 - 2.5\log f = ZP - 2.5\log f\,. \end{aligned}$$

With the Zero Point (ZP) defined by the reference star. Historically, Vega (α Lyrae) was used as the reference star and thus its magnitude is set to $m_0 = 0$. Fig 4.1 represents the apparent magnitude of multiple objects and the limiting magnitude of some observing instruments like the Hubble Space Telescope (HST). By definition, an object flux is the count of number of photons per unit area and per unit time. Considering S as the collecting area of the telescope (usually the one of the primary mirror) and T is the observation duration, the measured flux is :

$$f = \frac{N}{S\,T}$$

with N being the photon counts. We, therefore, can write :

$$\log\left(\frac{f}{f_0}\right) = \log\left(\frac{N}{N_0}\right)$$

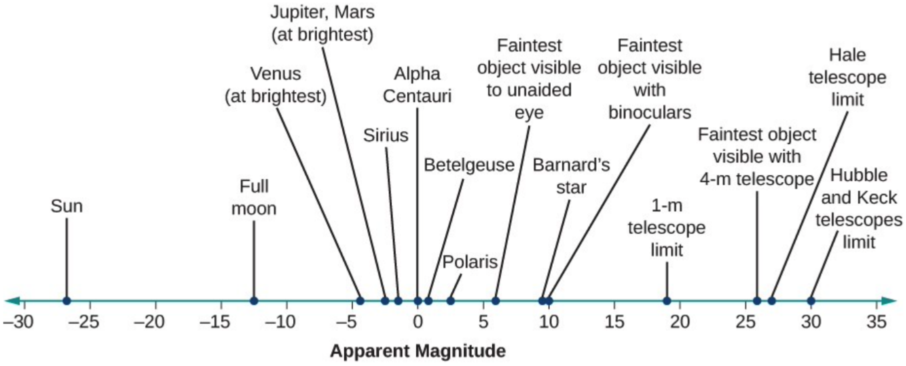

Figure 4.1: Apparent magnitude of well-known objects and the limit of different instruments.

We can find back the magnitude:

$$m = ZP - 2.5 \log N \quad \text{then} \quad ZP = m_0 + 2.5 \log N_0 \,.$$

An ideal detector has an amount of ADU (Analog-to-Digital Unit) counts equal to the amount of detected photons. In practice, we do not measure the number of photons directly but the counts in ADU recorded by the pixels of the camera. The ADU counts result from several effects like the Quantum efficiency (QE) of the CCDs. The ADU counts are related to the number of electrons by a divisive number, the gain.

4.2 ZTF photometric calibration pipeline

In this section we will describe the current ZTF photometric calibration technique and its performance.

4.2.1 Motivation

Beyond the importance of photometric calibration in cosmology measurements, multiple effects may bias SNeIa distance measurements. Working groups have identified them as instrumental uncertainties including CCD response linearity, CCD uniformity, brighter-fatter effect (Antilogus et al. 2014) and filters uniformity. Early on, this work on the photometric calibration stood in collective efforts to turn ZTF SNeIa sample to a state-of-the-art cosmological sample.

One role of the photometric calibration is to ensure that the relationship between the magnitudes and their broadband flux counterparts is not broken. To do so, in ZTF, the calibrated magnitudes m_{cal} of an object, whose measured flux is f, is defined as :

$$m_{cal} = -2.5 \log_{10} f_{ADU} + \text{calibration coefficient.} \tag{4.1}$$

The photometric calibration output is the calibration coefficient, the Zero Point (ZP). Its estimation will be explained in Section 4.2.2. More specifically, Equation (4.1) could be written :

$$m_{cal} = -2.5 \log_{10} f_{ADU} + ZP. \tag{4.2}$$

It shows that any bias in the ZP estimation or flux measurements will impact the calibrated magnitudes and the resulting cosmological measurements. On the other hand, if we aim to gain precision level in the photometric calibration, we need to better constrain the ZP estimation.

4.2.2 Current method

The current ZTF photometric calibration method is anchored on Pan-Starrs 1 $PS1$ (Chambers et al. 2016) filtered calibrator sources (Flewelling et al. 2020). The calibrators are partitioned into field/quadrant catalogue files. The selection of the calibrators is described in ZTF pipeline document. The main selection criteria to select PS1 calibrators are:

- isolated stars, *i.e.* with no other source within 3.5 arcsec,
- $PS1$ magnitudes range ($14.5 < r^{PS1} < 21$) corresponding to ZTF one,
- well-measured $PS1$ stars based on a minimum SNR (> 2) and a minimum of good single-epoch measurements (> 6) in all relevant $PS1$ filters (g, r, i, and z),
- non variable, i.e. main sequence, stars based on star color cuts.

Per image, the instrumental magnitudes (obtained from raw fluxes using Equation (4.1)) from ZTF PSF catalogue (psfcat) and the magnitude (in AB system) from the corresponding PS1 catalogue are used in a linear fit, where a Zero Point (ZP) and a color coefficient c are estimated. The following quantity is minimized, per filter :

$$g^{PS1} - g = ZP_g + c_g(g^{PS1} - r^{PS1}), \tag{4.3}$$
$$r^{PS1} - r = ZP_r + c_r(g^{PS1} - r^{PS1}), \tag{4.4}$$
$$i^{PS1} - i = ZP_i + c_i(r^{PS1} - i^{PS1}). \tag{4.5}$$
$$\tag{4.6}$$

The left side of each equation refers to $PS1$ calibrator magnitudes (first term) in g, r and i bands, the second term is the instrumental magnitude of the same calibrators in ZTF bands. ZP is the Zero Point estimated per filter, c is a color coefficient used since ZTF and $PS1$ have different filters. The color coefficient term is a first order correction to extrapolate the PS1 filters to the ZTF ones, Fig 4.2 represents the transmission function of each surey filters. For each ZTF image, the sources from ZTF psfcat are cross-matched with the corresponding quadrant PS1 catalogue. Prior to cross-matching between $PS1$ catalog and ZTF psf catalog, some set of cuts are applied to the $PS1$ calibrators :

- only calibrators falling at > 30 pixels from the image edge are kept,
- with $PS1$ r-magnitude range within : $14.5 < mag < 20.0$,

- the left side of the equation Equation(4.6) and the right side ($m_1^{PS1} - m_2^{PS1}$, 1 and 2 refer to filter index) are symmetrically trimmed to guard against outliers,

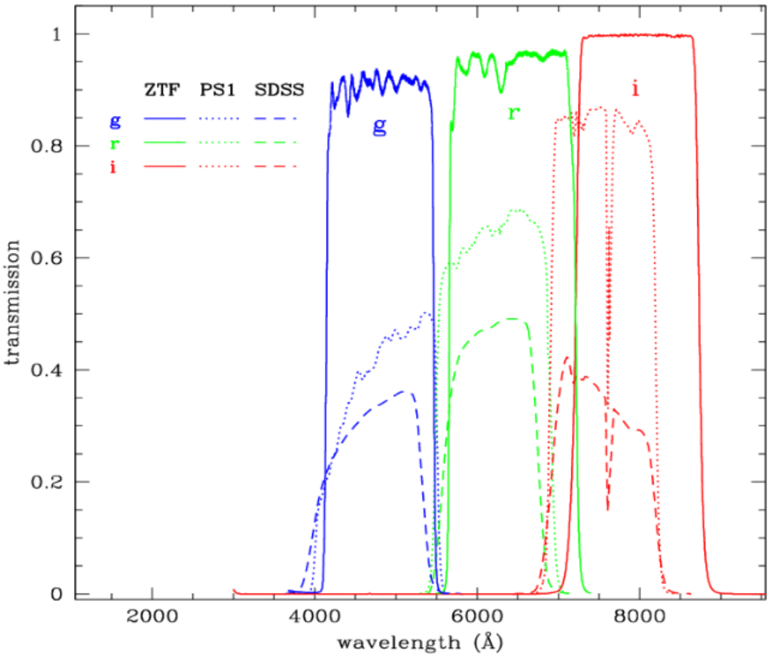

Figure 4.2: Transmission functions of ZTF (solid lines), PS1 (dotted line) and SDSS (dashed lines) in the g, r and i bands. From (Ngeow et al. 2019)

4.3 Upgraded photometric calibration

Our work on ZTF photometric calibration consists on improving the ZP estimation through two processes. We aim to implement "ubercal" state-of-the-art photometric calibration method from (Padmanabhan et al. 2008b) for ZTF images. With ubercal, calibrated magnitudes, temporal variations and spatial uniformity are fitted at the same time. We take into account true observing conditions, develop a method to better constrain the ZP and identify observations with poor photometric quality.

4.3.1 Atmospheric extinction

Airmass is the measure of the quantity of air along the line of sight when observing a celestial object from below Earth's atmosphere. It is therefore critical for ground based telescope like ZTF. As light penetrates the atmosphere, it is attenuated by scattering and absorption. The more atmosphere the light passes through, the greater the attenuation is. When we observe a star at the zenith, we have the minimum possible path length through the atmosphere, we say we are looking through "1 airmass". The flux from the star observed at the zenith is less scattered than a star observed at $45°$ from the zenith, as illustrated in Fig 4.3. From this same figure, Θ is the angle between the zenith and the observed object direction. The greater this angle is, the greater the atmospheric extinction is. Close to the zenith (Θ small), we say we look through secant Θ airmasses :

$$X = \sec\Theta \quad \text{with} \quad \sec\Theta = \frac{1}{\cos\Theta}\,. \tag{4.7}$$

X is the airmass and $\sec$ is the secant of Θ. Because of the curvature of Earth and hence the atmosphere, Equation (4.7) is replaced by the following formula, from Hiltner 1962 :

$$X = \sec\Theta - 0.0018167(\sec\theta - 1) - 0.002875(\sec\Theta - 1)^2 - 0.0008083(\sec\Theta - 1)^3. \tag{4.8}$$

In this same figure (Fig 4.3), we have represented the evolution of airmass in function of Θ, for the first half of 2019 ZTF observations. We can see the airmass values exceeding quickly 1, thus the importance of taking it into account in the estimation of the ZP. We have represented, in Fig 4.4 the difference of calibrators magnitudes in *ztfr* band, calibrated with ZTF photometric calibration pipeline and magnitudes from $PS1$ catalogue as a function of airmass calibrators computed from Equation (4.8). The magnitude differences get greater with the airmass. It shows evidence of the correlation between airmass and magnitudes estimation. In the following equation, we show how we account for the airmass in the estimation of the ZP :

$$m^{PS1}_{f,i} - m^{inst}_{f,i} = ZP_f + c_f(m^{PS1}_{f_1,i} - m^{PS1}_{f_2,i}) + \alpha_f(X_i - 1), \tag{4.9}$$

the two terms on the left side of the equation are respectively $m^{PS1}_{f,i}$ as the $PS1$ calibrator magnitude in f band and $m^{inst}_{f,i}$ refers to the ZTF instrumental magnitude of a calibrator in the corresponding f band. The first two terms of the right side are the same as in Equation (4.6), the last term correspond to the dependency of the airmass. α_f is the extinction coefficient, fitted along with the ZP_f and c_f in the multi-epoch fit. X_i corresponds to the airmass which is computed per calibrator using Equation (4.8). All the results will be presented in Section 4.4.

4.3.2 Extinction-color correlation

The airmass term added in Equation (4.9), is a first order correction to the magnitudes. We have added a second-order airmass color correlation like following :

$$m^{PS1}_{f,i} - m^{inst}_{f,i} = ZP_f + c(m^{PS1}_{f_1,i} - m^{PS1}_{f_2,i}) + \alpha_{f,i}(X_i - 1) + \beta(X_i - 1)(m^{PS1}_{f_1,i} - m^{PS1}_{f_2,i}), \tag{4.10}$$

4.3.3 Multi-epoch fit

The estimation of the ZP through a linear fit with two free parameters, like the current technique in ZTF pipeline, on a single observation can be biased by c, the color term. In order to better constrain the ZP, we have developed a multi-epoch fit. With our method the

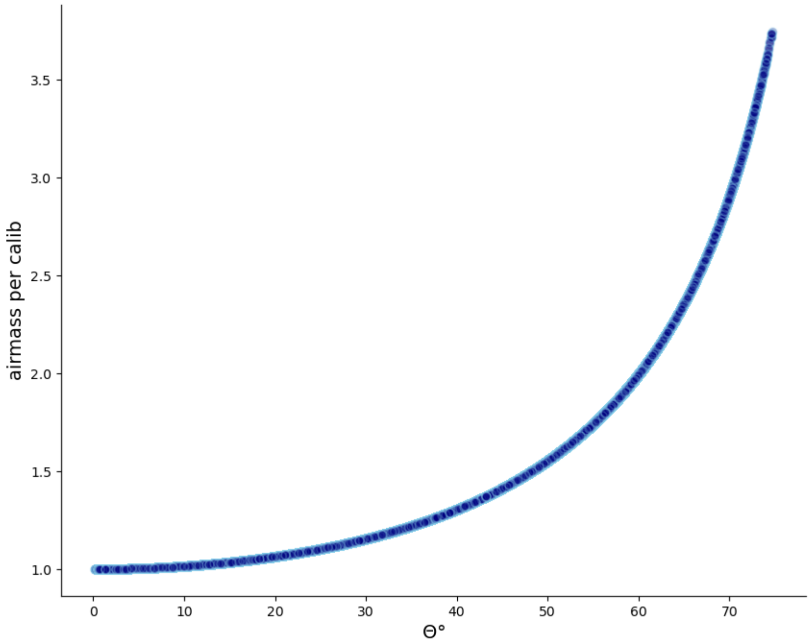

Figure 4.3: Evolution of the airmass of ZTF observations computed using Equation (4.8), from January 2019 to June of the same year, as function of θ.

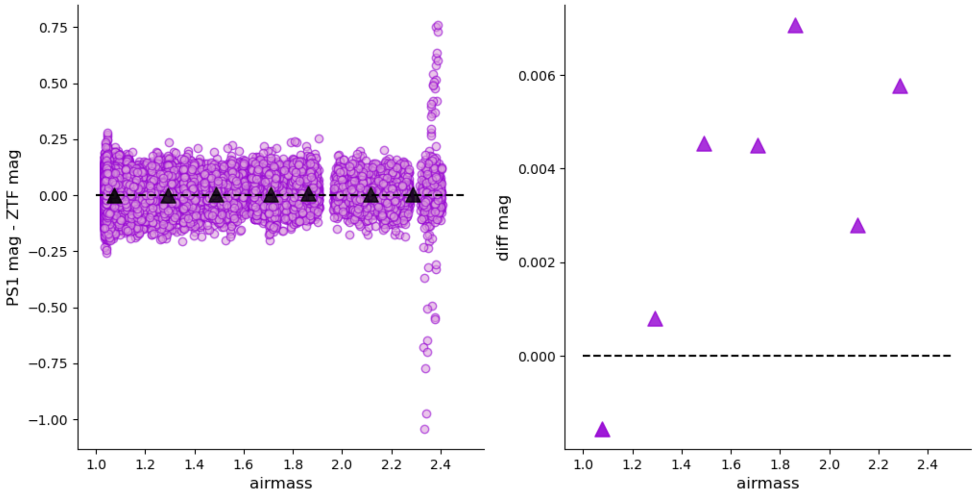

Figure 4.4: Calibrators Magnitude difference as it evolves with airmass calibrators. We have computed the difference between magnitudes calibrated with ZTF pipeline and magnitudes from $PS1$ catalogue in ZTF r band. In the right, we have only the binned data points.

ZP of all the images from the same quadrant, in a fixed period of time, are fitted together. Through ZTF observing strategy, discussed in Section 3.1.2, all the images from the same quadrant have the same calibrators and hence the same corrective color c. Driven by this idea, we fit only one c for the series of images from the same quadrant, in the multi-epoch fit. When taking into account observing conditions introduced in Section 4.3.1 and Section 4.3.2, we fit one α per image and one β for the series. The following χ^2 is minimized using *iminuit* minimizer in Python, for ZTF r band images :

$$\chi^2 = \sum_{i=0}^{N} \left(\sum_{j=0}^{K} m_{r,j}^{PS1} - m_{r,j}^{inst} - ZP_i - c(m_{g,j}^{PS1} - m_{r,j}^{PS1}) - \alpha_i (X_j - 1) \right) \tag{4.11}$$

The first sum runs over the series of N images, while the second one over the K calibrators.

Photometric observations flag

In the multi-epoch fit, all the observations of the same quadrant are used, there is no selection on the quality of the observations. As, c, the color coefficient is assumed to be the same for a set of calibrators from one ZTF quadrant, images with bad observing conditions (*e.g.* presence of clouds) can affect the color of the calibrators and thus bias the multi-epoch fit. To avoid that, a selection of good observations is required. We, therefore, need to assess the photometric quality of the observations and identify the ones we should not take into account. Our selection is based on the number of calibrators matched between $PS1$ catalog and ZTF psf catalogue. It is the most sensitive parameter to the observing conditions like the presence/absence of clouds and the moon. With a clear sky, ZTF should observe most (all, in idealistic scenario) of the calibrators in the corresponding $PS1$ catalog. The presence of the moon or clouds affects the number of sources observed by ZTF and hence the number of matched calibrators with $PS1$ catalogue. The quality criterion considered is the fraction of matched sources of ZTF images with the associated $PS1$ catalogue in the corresponding field of observation. This number could be 1 at maximum. We have represented the distribution of the proportion of matched calibrators for all the images, left of Fig 4.5. Right of the same figure, top image is a ZTF science image with a proportion of matched calibrators of more than 0.9, bottom is one with a proportion less than 0.1. We set an observation as a photometric one and use it in the multi-epoch fit if the proportion number is equal or above 0.6. For an observation to be part of the multi-epoch fit, we require that the ZTF psf catalogue should contain at least 60% of the $PS1$ calibrators listed in the reference catalogue.

4.4 Results

In this section, we will discuss the results of observing conditions modelling and our multi-epoch estimation of ZP. We have evaluated the calibrated magnitudes with our methods by comparing them to the calibrated magnitudes using ZTF pipeline photometric calibration from Section 4.2. We considered the same calibrators used by the pipeline, computed their calibrated magnitudes using ZP from the pipeline and our different suggestions for a fixed

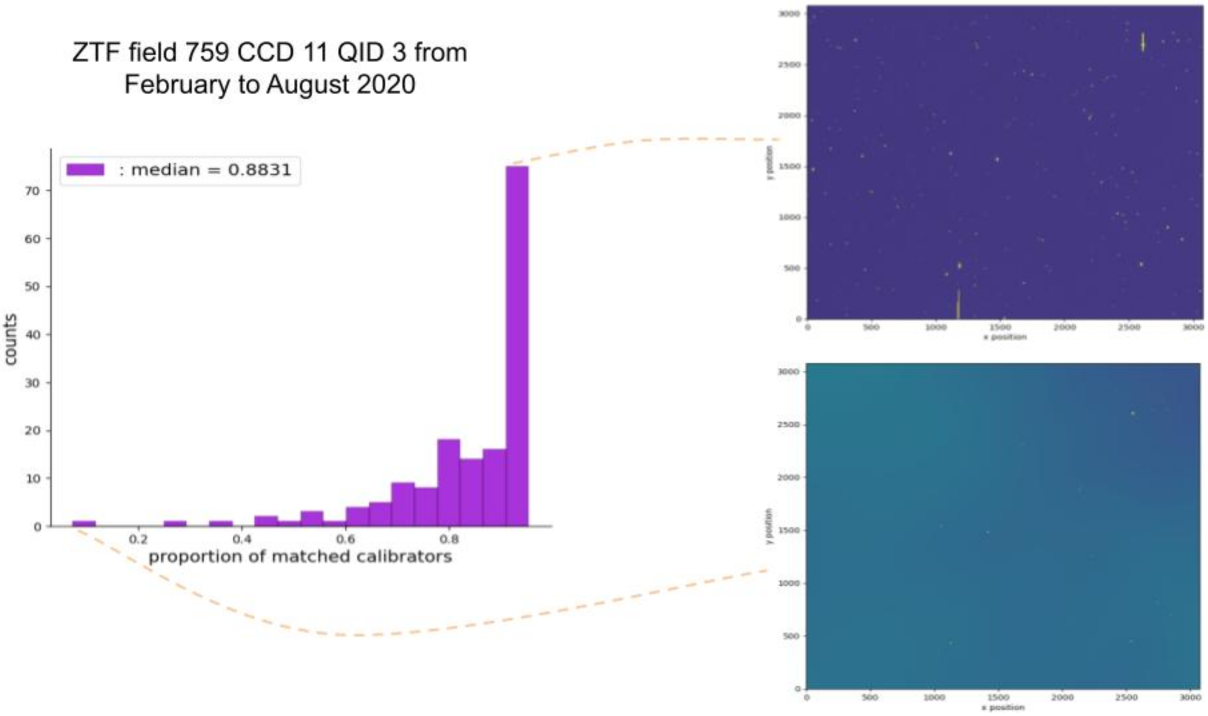

Figure 4.5: **Left:** distribution of proportion numbers of matched calibrators between ZTF PSF catalogue and $PS1$ catalogue for all the images of ZTF field 759 CCD 11 QID 3 from February, 2^{nd} 2020 to August, 30^{rd} 2020. ***Right:*** top and bottom are ZTF science images with, respectively, a high proportion number and a lower one.

period of time. Since the calibrators used are non-variable stars, their calibrated magnitudes do not vary with time. The standard deviation of the calibrators magnitude, over a period, is our measure of the precision of the photometric coefficients estimation.

4.4.1 Single epoch

We have reproduced ZTF photometric ZP estimation and added the atmospheric extinctions in our fit, as explained in Section 4.3.1. For each image, we estimate the ZP, c and α, respectively, the color coefficient and the extinction coefficient. The comparison between the dispersion of the calibrators magnitude calibrated using ZTF pipeline and our fit with atmospheric extinction is shown in Fig 4.6. We can see that the magnitudes dispersion estimated with our technique is below the ones from the pipeline. This result indicates a better precision for the photometric calibration, especially for bright objects (smaller magnitudes).

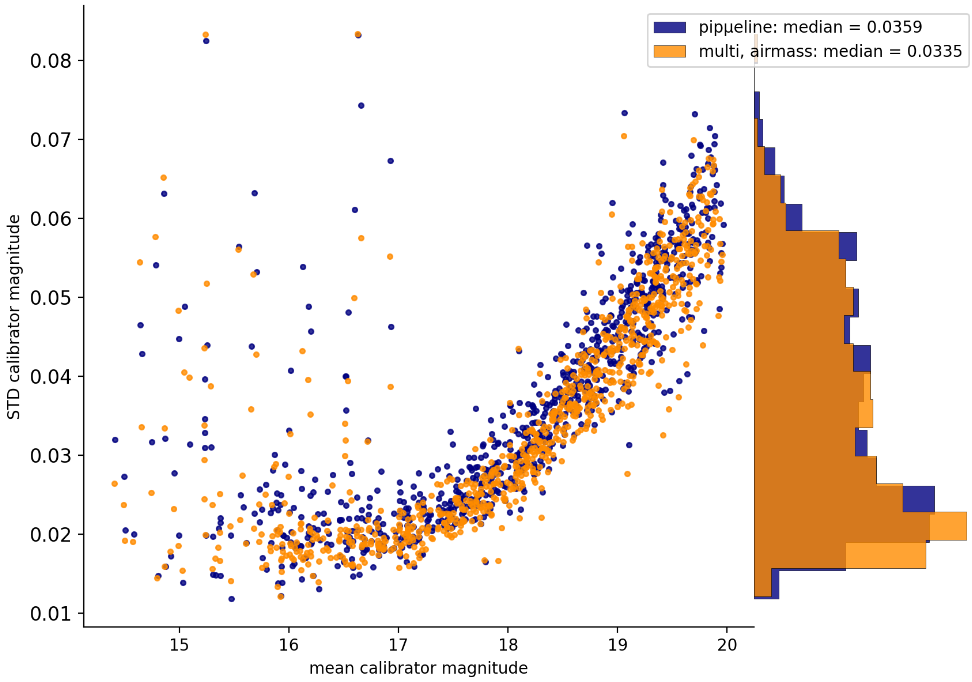

Figure 4.6: Calibrated magnitude dispersion of the calibrators as a function of their mean calibrated magnitude. In blue, the magnitudes are calibrated using the ZTF photometric calibration pipeline and in orange they are calibrated using Equation (4.9). The right part of the figure displays the distribution of the magnitudes dispersion of both estimation is displayed.

4.4.2 Multi-epoch fit and photometric observations

Based on the description of our method in Section 4.3.3, fitting all the images at the same time, we first estimate ZP and global c with and without the photometric observations selection introduced in Section 4.3.3.
Fig 4.7 and 4.8 show respectively the results with the multi-epoch fit and the multi-epoch fit with the selection of photometric observations both compared to the outputs of ZTF pipeline. We can see that the multi-epoch reduces the dispersion of the calibrators by 5%, the data points from the multi-epoch fit sitting below the pipeline ones. It is also clearly visible in the comparison of the dispersion distributions, indicating better constraints on the ZP estimation. From Fig 4.9, we can notice that the photometric observations flag allows to remove all the outliers in the bright magnitudes range ($[14.5, 17]$) which helped to reduce the dispersion by 10%.

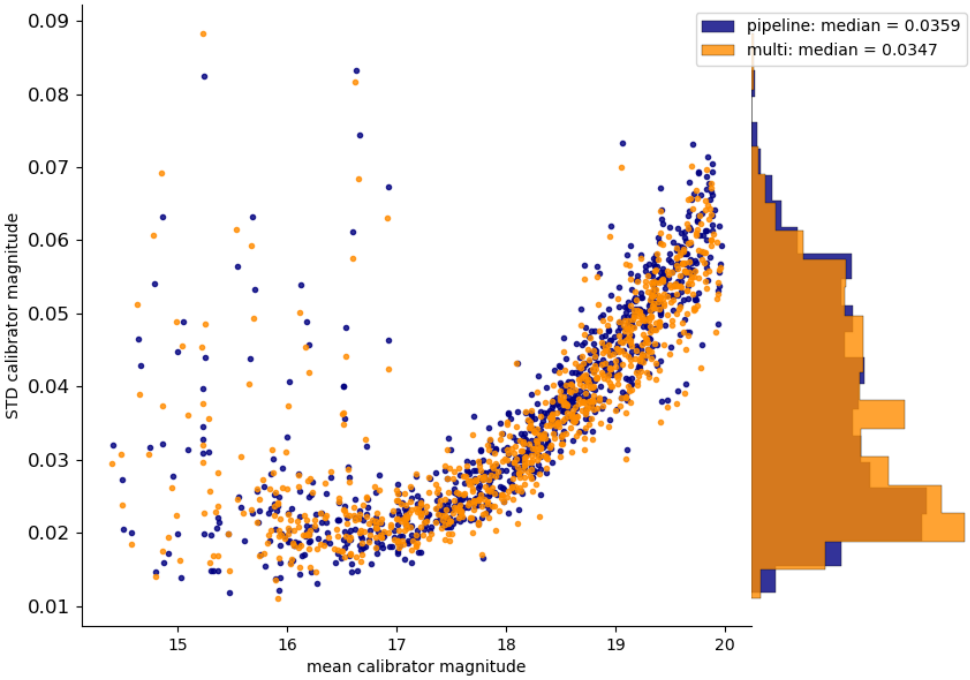

Figure 4.7: Calibrated magnitudes dispersion in function of the mean calibrated magnitudes in a fixed period of time. In blue, the magnitudes are calibrated using the ZTF photometric calibration pipeline and in orange, they are calibrated with our multi-epoch method. The right part of the figure displays the distribution of the magnitudes dispersion for both estimation is displayed.

Multi-epoch fit with atmospheric extinctions

We present here the results of the dispersion of the calibrators with the multi-epoch technique and atmospheric extinction taken into account from Section 4.3.1. We also removed

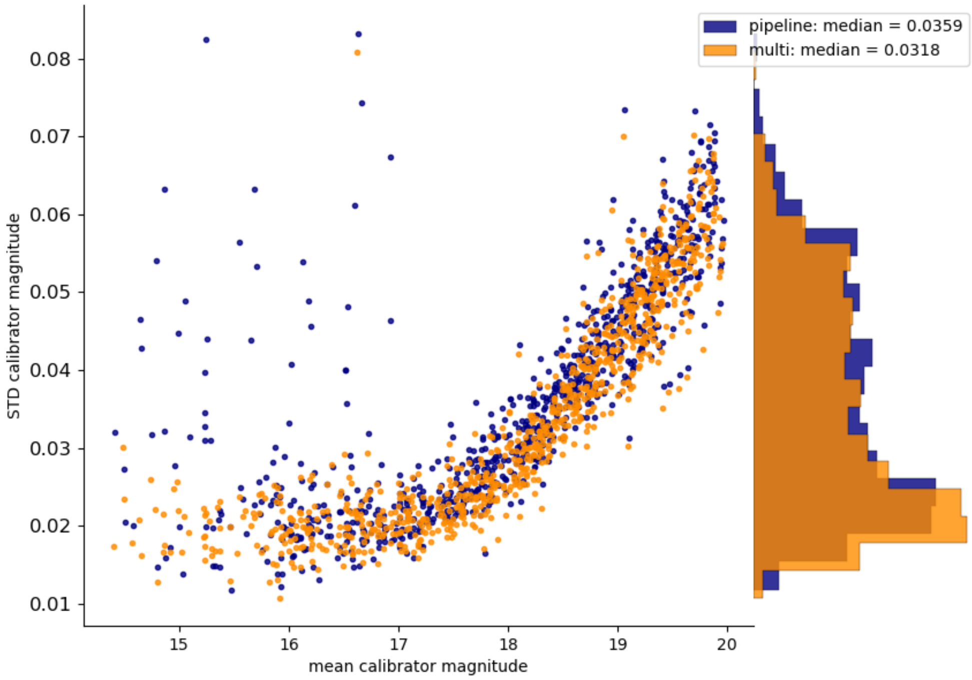

Figure 4.8: Calibrated magnitude dispersion in function of the mean calibrated magnitudes in a fixed period. In blue, the magnitudes are calibrated using the ZTF photometric calibration pipeline and in orange, they are calibrated with our multi-epoch method after removing the bad photometric observations. The right part of the figure displays the distribution of the magnitudes dispersion of both estimation is displayed.

the bad photometric observations (see Section 4.3.3), since we showed in 4.4.2 that their absence significantly reduced the dispersion of the calibrators. Fig 4.9 represents the dispersion of calibrators magnitude computed with airmass correlation in the multi-epoch fit after removing the bad photometric observations in function of their mean magnitudes. We compared our result to the ZTF pipeline method, in the same figure. Taking into account the atmospheric extinctions enables to reduce the dispersion by 15% when compared to the dispersion recorded by the pipeline and by about 10% when compared to our results in Fig 4.8 with the multi-epoch fit after removing the bad photometric observations.

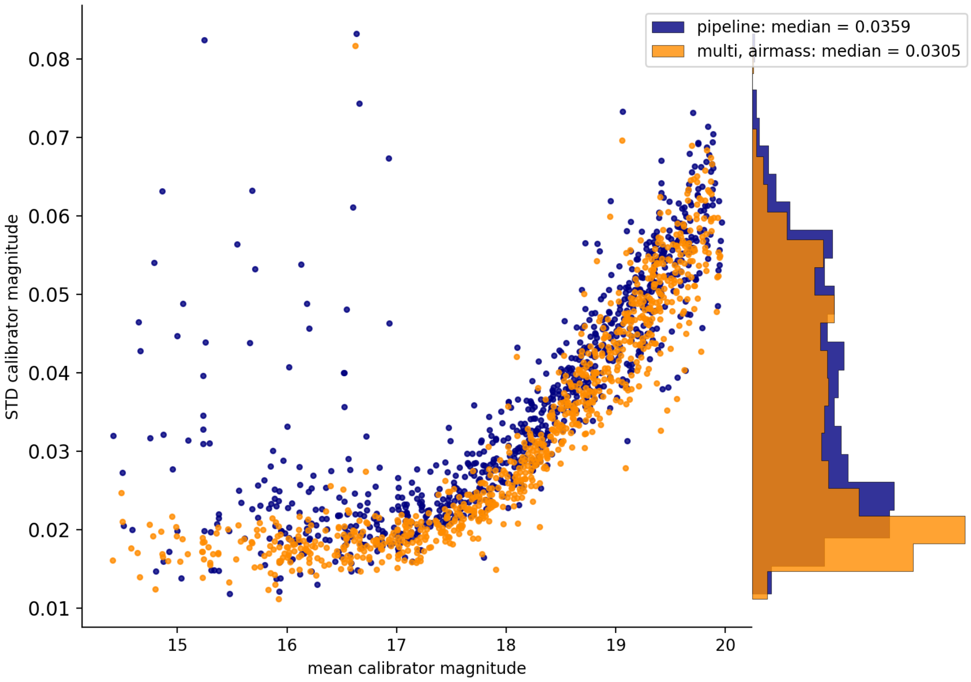

Figure 4.9: Calibrated magnitude dispersion in function of the mean calibrated magnitudes in a fixed period of time. In blue, the magnitudes are calibrated using the ZTF photometric calibration pipeline and in orange, they are calibrated with our multi-epoch method with atmospheric extinctions accounted for and removing the bad photometric observations. The right part of the figure displays the distribution of the magnitudes dispersion of both estimations.

Moreover, we applied technique described in Section 4.3.2 in a multi-epoch fit after removing the bad photometric observations. We did not notice any improvement in the magnitudes dispersion, the results are the same than in 4.4.2 when only the airmass correlation is accounted for.

4.5 Conclusions & perspectives

We aimed to improve ZTF photometric calibration to better constrain the ZP of the images. We took into account real-time observing conditions like the airmass in a single-epoch fit, similar to the ZTF pipeline technique. It slightly reduced the dispersion of the calibrators magnitude. We developed a multi-epoch fit in which we estimated simultaneously the ZP for a series of images from the same ZTF quadrant. This technique significantly improved the constraints on the ZP. We added a flag to remove bad photometric observations from the series of images which highly contributed to reduce the dispersion of the magnitudes. We added the airmass correlation to the multi-epoch fit, along with the photometric quality flag, the magnitudes dispersion is reduced by 15% when compared to the output of the pipeline.

This work was a preliminary study of applying the "ubercal" technique (Padmanabhan et al. 2008a; Padmanabhan et al. 2008b) to ZTF images. A more complete analysis is being developed by IN2P3 research groups.

CHAPTER 5

TYPE IA SUPERNOVAE IN COSMOLOGY

The term "supernova" was first introduced in 1934 by Walter Baade and Frizt Zwicky to refer to extremely bright astrophysical events in a short period of time (about a week). The origins of this kind of events are diverse, the physics behind it is the same for all of them. It is the violent explosion of a star or a part of it, like its core. The explosions can be detected in very remote galaxies, thus they are important to observational cosmology. Some sub-types of supernovae, like Type Ia Supernovae are homogeneous objects with relatively known absolute luminosity. Assuming an unique luminosity, SNeIa are known as *standardisable candles* and provide accurate distances that can be used to probe the Universe. SNeIa will be described in this chapter. SNeIa are defined, classified with their properties described in 5.1, their astrophysical origins are also discussed. In Section 5.2, we present distance measurements with SNeIa as standardisable candles and their use in cosmology. Finally in Section 5.3, we discuss the sources of uncertainty and limitations of SNeIa as distance indicators and probe of the late Universe.

5.1 Object description

SNeIa are very luminous explosive events in the sky that can last several weeks. They have been long observed and studied, however their origins remain uncertain. Their observed properties are well known and can be used to classify them. They display homogeneous spectral and photometric properties which makes them accurate distance indicators.

5.1.1 Supernovae classification

The empirical classification of SNeIa is based on their spectroscopic and photometric properties. Spectroscopic properties are obtained from the absorption lines on the SNe spectra, near maximum light (Filippenko 1997a). Photometric properties are defined through a light-curve, which is the variation of the measured flux with respect to time in one or many photometric bands. An early classification scheme was introduced in (Lundmark 1925; Minkowski 1941). There are two main categories of SNe based on the presence or absence of hydrogen in their spectra. Type II SNe exhibit hydrogen lines while SNeIa do not. Type Ib SNe show helium lines and Type Ic lack lines of helium and silicon. SNeIa spectra present silicon lines and no helium. Fig 5.1 shows the photometric and spectroscopic properties of all known types of supernovae.

5.1.2 Observational properties

SNeIa are transient objects lasting about 60 days and at their peak luminosity they outshine their host galaxy. Fig 5.2 represents a series of SNeIa images. Their spectroscopic and photometric properties are homogeneous. Therefore, their light-curves and spectra are reproducible.

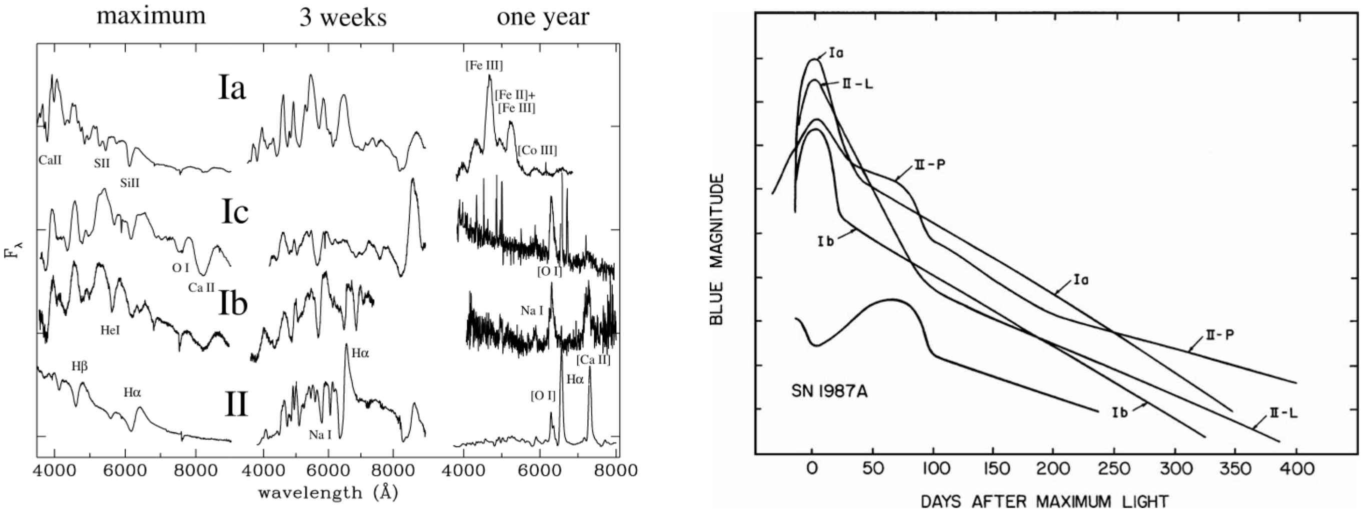

Figure 5.1: *Left:* Comparison of SNe spectra from (Turatto 2003). *Right:* SNe light-curves from (Filippenko 1997b).

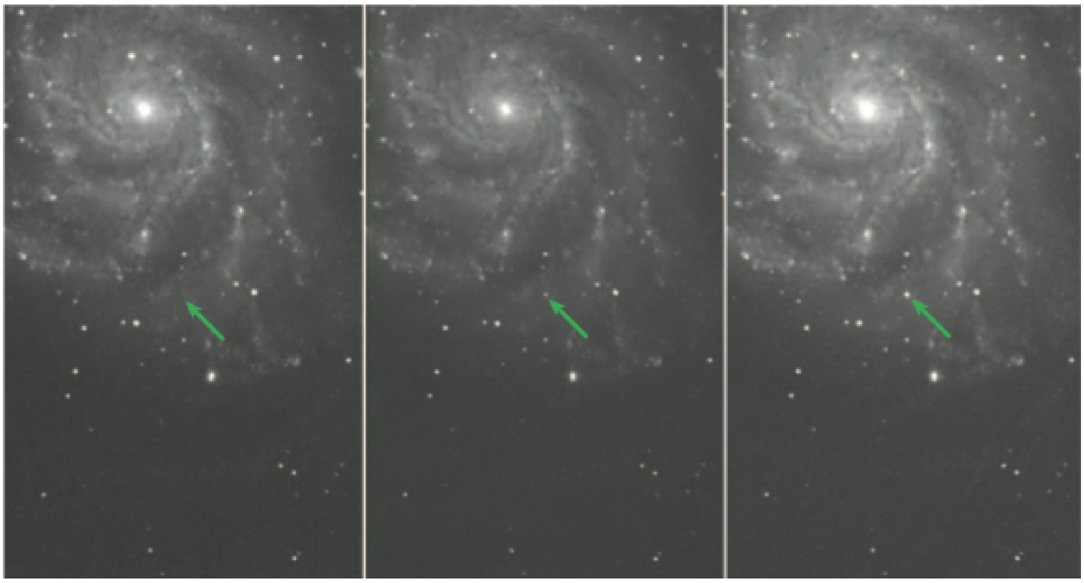

Figure 5.2: Series of images of SNIa SN2011fe in Messier 101 (M101) galaxy, detected and observed by the *Palomar Transient Factory* (Nugent et al. 2011). All the images are one night interval, they were taken respectively August the 23rd, 24th and 25th, 2011.

Spectroscopic features

SNeIa spectra lack of hydrogen and helium lines, as introduced in Section 5.1.1. These spectra are dominated by lines of intermediate mass elements such as silicon, calcium, magnesium, iron and sulfur. Even though the spectral features are homogeneous, they show some diversity. In Fig 5.3, we have an example of a regular SNIa spectrum with all the features of the intermediate mass elements. Peculiar SNeIa have different spectral evolution with/or some extra features *e.g.* stronger lines for some elements or extra lines (Branch, Baron, and Jeffery 2001).

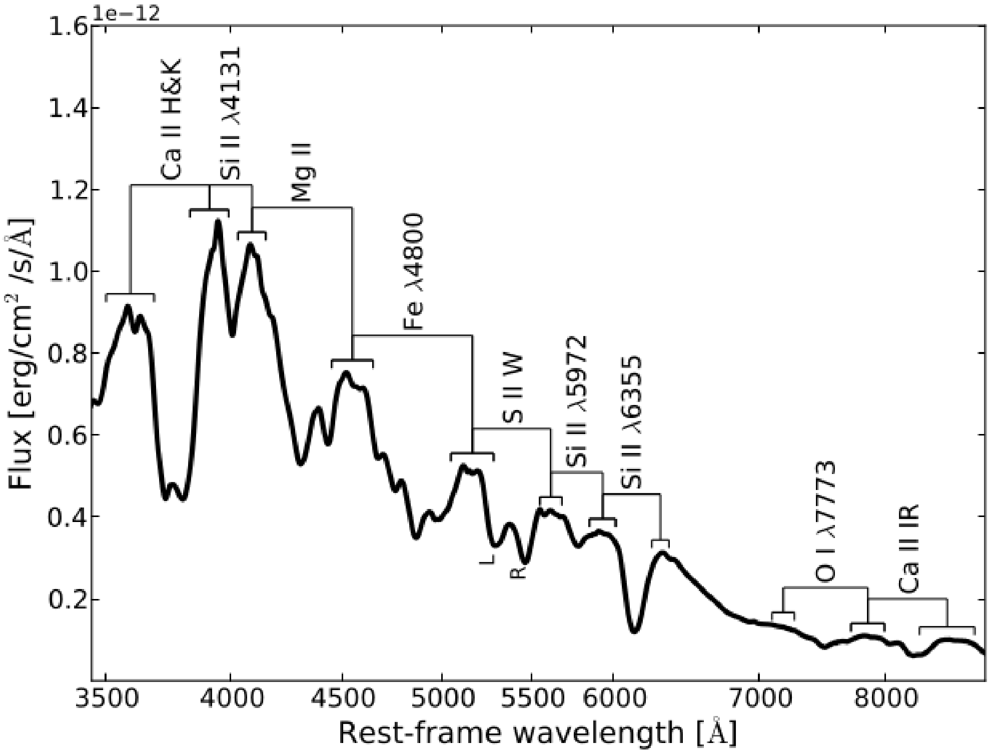

Figure 5.3: Spectrum of a SNeIa at peak luminosity. The figure is from Chotard 2011. The spectrum is dominated by the presence of Si II absorption lines at 4130Å and 6355Å.

We can sum up SNeIa spectra features:

- Lack of helium and hydrogen.
- Silicon absorption line of Si II at 4130Å. A second absorption line of Si II at 6355Å.
- Sulfur: a "W" can be observed at 5649Å, due to the doublet of S II.
- Calcium: a doublet due to Ca II at 3934Å and 3968Å.

Photometric properties

SNeIa display a varying luminosity with time, as shown in Fig 5.4. Their light-curves are characterised by a rising time of circa 15 days in B band[1], before it reaches the luminosity peak. The duration of the rising time changes from band to band. Then the luminosity starts slowly to decrease during one month or more. SNeIa light-curves also display a secondary maximum, observed, in the red and infrared bands, around 25 days after the luminosity peak in B band. The varying luminosity of SNeIa can be explained through the ballistic expansion of a sphere. The light-curves luminosity is consistent with the radioactive decay of ^{56}Ni

---

[1] Blue band in UBV photometric system

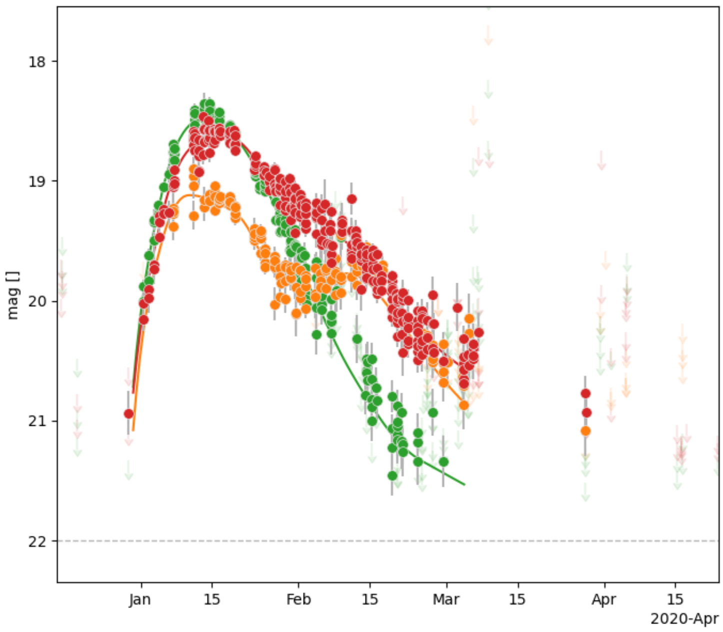

Figure 5.4: Light-curve of SNIa ZTF20aaawmxq, observed by ZTF in g (green), r (red) and i (infra-red) bands.

and varies according to the opacity of the ejecta to the decay products. This scenario could explain why the luminosity varies in two main phases. At the beginning of the explosion, the emitted photons from ^{56}Ni decay $^{56}\text{Ni} \rightarrow^{56} \text{Co} \rightarrow^{56} \text{Fe}$ will be captured by the star's high matter density. It is this phenomena that powers the rising part of the light-curves.

5.1.3 Astrophysics of SNeIa

The possible progenitor scenarios of SNeIa are still debated. The interpretation of the homogeneity of SNeIa magnitudes is that they are caused by a thermonuclear explosion of a carbon-oxygen white dwarf CO-WD. As matter of fact, SNeIa similar luminosities are explained by similar critical masses required for the stellar explosion to happen. The SNeIa light-curves timescale are consistent with the half life of ^{56}Ni, which is the end of the carbon-oxygen fusion chain. The spectra composition of SNeIa, like presence of intermediate mass elements which are the products of the carbon-oxygen fusion and the absence of helium and hydrogen are the signature of CO-WD. However, the characteristic mass of a CO-WD is up to $1.2M_{\odot}$, it needs to reach Chandrasekhar mass limit ($\sim 1.4M_{\odot}$), above which the electrons degeneracy pressure fails to balance its own gravitational self-attraction (Chandrasekhar 1931). To acquire the Chandrasekhar mass, the CO-WD needs to accrete enough matter from the surrounding environment. Based on the explosion's observables , the CO-WD accretes matter from two possible companion objects, it is either another CO-WD or a companion star. There are two types possible companion and thus scenario developed below.

Single Degenerate scenario (SD): it is a binary system (Whelan and Iben 1973; Nomoto 1982) consisting of one WD and a less compact star (*e.g.* a main sequence star, a red giant). The WD accretes matter from its less massive companion until it reaches the Chandrasekhar mass and explode as a SN Ia.

Double Degenerate scenario (DD): It is based on a binary system of two WDs merging. Before the merger, the mass of each WD are under the Chandrasekhar limit. However, their collision enables the system of two WDs to reach the needed mass limit to produce a SN Ia.

The strong point of the DD scenario is its consistency with the absence of hydrogen in SNeIa spectra since the system lacks of it, unlike the SD scenario. On the other hand, despite many observations of SNeIa with ejecta masses beyond Chandrasekhar limit, which would support the DD scenario, it shows disagreement with the homogeneity of SNeIa. In fact, this homogeneity suggests a constant initial mass to produce a SNIa which is consistent with the SD scenario.

5.1.4 Explosion rate

The SNeIa explosion rate is the number of SNeIa occuring in a space region during a time frame or in a given volume of the universe (in Mpc^{-3}yr^{-1}). Knowing the SNeIa rate is crucial to elaborate surveys observing programs. Fitting this number with a model can highly contribute to constrain the physical mechanisms of SNeIa and their progenitor. Knowing the rate of explosion is also useful to make the most realistic simulations of SNeIa samples. In Chapter 7, we used the simulations framework from Feindt et al. 2019 that based the rate of explosion of SNeIa on the one measured by Li et al. 2011 up to: $(0.301 \pm 0.062) \times 10^{-4}$ SNeIa Mpc^{-3}yr^{-1} at $z = 0$. The authors used a sample of 1000 SNe from the Lick Observatory Supernova Search (LOSS), the rate is interpolated at low-z with $(1 + z)$ factor. The number of observed SNeIa depends on the volume we observe: a combination of field of view of the telescope and its depth.

5.2 Distance measurements with SNeIa

SNeIa are standard candles, they can be used to measure distances. The maximum absolute magnitudes of SNeIa in B band are quite the same ($\simeq -19.3$, Astier et al. 2006) with a scatter of $\sigma \sim 0.4$ mag. It corresponds to a scatter of $\sim 20\%$ in distance. This dispersion can be significantly reduced when using measurable features from the SNeIa light-curves. In this section, we will introduce SNeIa light-curves variability, the state-of-the-art template that models them and how the standardised candles are used to estimate the cosmological parameters through the Hubble diagram.

5.2.1 Standardisation

SNeIa display quite uniform light-curves. However, they are not exactly standard candles; they are *standarisable candles*. Using the variability of SNeIa light-curves and their intrinsic luminosity or the correlations between photometric observables, we can reduce the scatter in SNeIa magnitudes and therefore in the measured distances. The two main correlations are : the brighter-slower and the brighter-bluer relation.

The variability of the light-curve can be expressed using its **stretch** and **color** parameters. Stretch corresponds to the time span of the curve, while the color expresses chromatic differences.

5.2.2 Brighter-slower relation

It shows that brighter SNeIa display slower decline than fainter ones (Phillips 1993). This correlation is modeled by the stretch parameter. This parameter is considered as intrinsic, it is linked to physical properties of the explosion like the progenitor metalliicity, the quantity of radioactive elements during the explosion. Top Fig 5.5, from (Goobar and Leibundgut 2011), shows the correlation between the stretch and SNeIa luminosity.

Brighter-bluer relation

It is the correlation between the color $(B - V)$[2] and SNeIa luminosity (Riess, Press, and Kirshner 1996). The color can change from one SNIa to another due to whether an extrinsic or intrinsic variability. The extrinsic variability is caused by galactic dust from SNIa host galaxy that scatters and absorbs SNIa light (Cardelli, Clayton, and Mathis 1989) and hence produce a dimming. On the other side, the intrinsic variability is caused by SNeIa progenitor variability. Bottom of Fig 5.5, from Goobar and Leibundgut 2011, shows the correlation between SNeIa luminosity and the color parameter.

5.2.3 Variability modelling: SALT2

Light-curves can be modeled using a luminosity parameter and a decline rate parameter like the stretch. This leads us to the Tripp relation (Tripp 1998) that expresses the *distance modulus* :

$$\mu = m_B^* - M_B + \alpha x_1 - \beta c, \tag{5.1}$$

where m_B^* is the observed maximum B band magnitude in rest-frame, x_1 is the stretch parameter and c is the color one. These parameters are derived from a fit of the SNeIa light-curves. M_B (absolute magnitude of the SNeIa), α (stretch coefficient) and β (color coefficient) are nuisance parameters, constrained simultaneously with the cosmological parameters in a Hubble Lemaître diagram fit (see section below in 5.2.4).

---

[2] The color of a SNIa can be defined as the magnitude difference of the SNIa, for example, in B and V bands at its maximum luminosity.

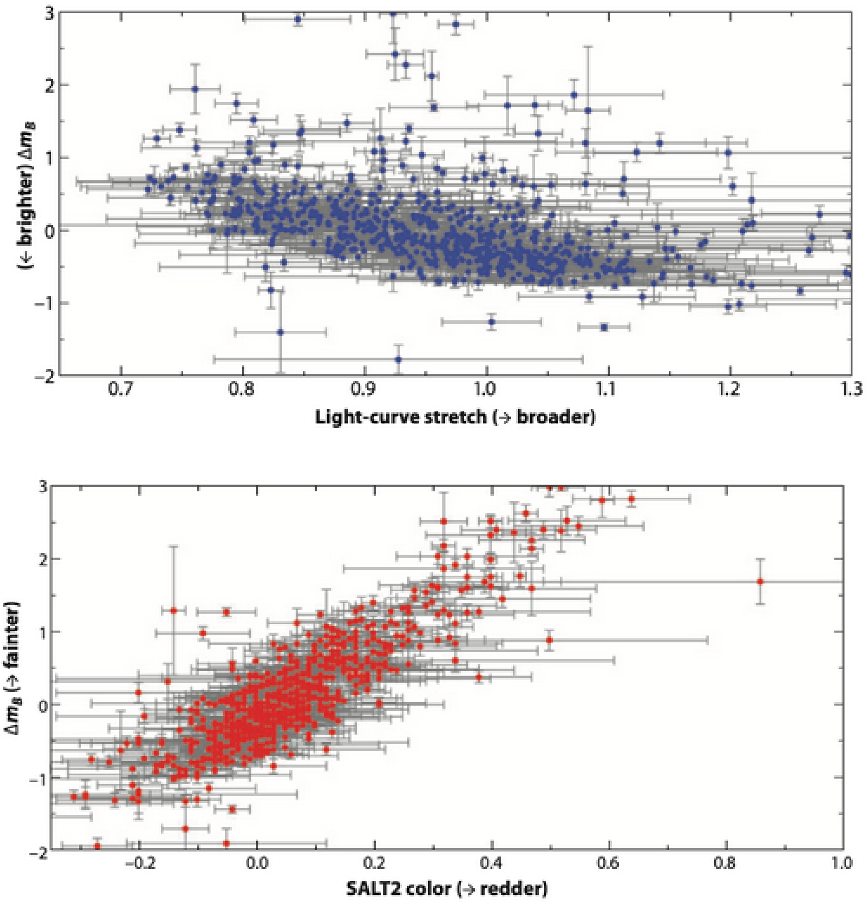

Figure 5.5: Correlations of SNeIa residual luminosities (Δm_B) with the stretch parameter in the *upper panel* and with the color parameter in the *lower panel*. There are 685 SNeIa light-curves in B band (Amanullah et al. 2010). Covering a redshift range from $0.025 < z < 1.4$. The stretch and color correlations represented here are used to correct the SNeIa distances and enable to reduce significantly the scatter in SNeIa luminosity.

Multiple light-curves fitters that estimate specific SNeIa parameters were built, among the latest ones we can cite SALT2 (Guy et al. 2007), MLCS2k2 (Jha, Riess, and Kirshner 2007), SNEMO (Saunders et al. 2018) and SUGAR (Leget et al. 2020). Since the correct mechanism that gives birth to SNeIa remains unknown, all the models are empirical. The main difference between the models is how the color parameter and the residual dispersion of SNeIa absolute magnitude are modelled.

The Spectral Adaptive Light-curves Template 2 (SALT2), constructed by (Guy et al. 2007) and later updated in Betoule et al. 2014 (known as SALT2.4), is an empirical model that fits the SNeIa light-curves and estimates the needed parameters to standardise them. It models, at the first order, the variations of the SNeIa flux as a function of time and wavelength λ. Thereby, at a p phase and a λ wavelength, the flux density for one SNIa is defined as:

$$f_{SN}(p,\lambda) = x_0 \times (M_0(p,\lambda) + x_1 M_1(p,\lambda)) \times \exp\left(c \times C_L(\lambda)\right); \tag{5.2}$$

where x_0 is a normalisation factor, $M_0(p, \lambda)$ the mean spectral sequence, $M_1(p, \lambda)$ the first order deviation around the mean sequence, $C_L(\lambda)$ is phase-independent color-law trained on spectroscopically identified SNeIa sample. To sum up, $M_0(p, \lambda)$, $M_1(p, \lambda)$ and $C_L(\lambda)$ are the model properties, whereas x_0, x_1 and c are specific to each SNIa.

To extract the parameters needed to the standardisation of SNeIa, namely m_B^*, x_1 and c, and use Equation (5.1) to estimate accurate distances, we need full light-curves of SNeIa observed in multiple bands. From these observations and their redshitfs, we can use light-curves fitters like SALT2 that provides :

- the rest-frame magnitude peak in B band m_B^*,
- the stretch parameter x_1,
- the color parameter c,
- the date of maximum luminosity in B band t_0.

By taking into account the brighter-slower and the brighter-bluer correlations for SNeIa standardisation, the scatter in magnitude has been more than half reduced, from $\sigma \sim 0.4$ mag to $\sigma \sim 0.15$ mag. Thanks to SALT2 that enables us to correct SNeIa peak luminosity and put it in common, we can perform more precise distance measurements. Such measurements, with their relation to the energy-matter content of the Universe like Equation (2.6) will ultimately allow to test ΛCDM model through bulk flows detection, probing growth of structures and dark energy characterization.

5.2.4 Hubble diagram

SNeIa as standardizable candles, indicate distances with the use of Equation (5.1). The Hubble diagram is known as the relation between the distance modulus of SNeIa (assimilated to distances in the Universe) and their redshift (assimilated to cosmic time). In Fig 5.6, an example of an Hubble diagram with SNeIa combined from several surveys, known as the Pantheon sample (Scolnic et al. 2018) is represented. To produce an Hubble diagram and estimate the cosmological parameters, we need to minimize the following function:

$$\chi^2 = \sum_n \frac{(\mu(m_{B,n}, x_{1,n}, c_n, M_B, \alpha, \beta) - \mu_{th}(z_n, \Omega_m))^2}{\sigma_n^2 + \sigma_{int}^2}, \tag{5.3}$$

where μ is the observed distance modulus as defined in Equation (5.1), μ_{th} is the theoretical distance modulus (from Section 2.1.2), the term σ_n is the propagated error from x_1 and c associated to SNIa number n and σ_{int} is the residual intrinsic scatter. In effect, without the term σ_{int}, the χ^2 per number of degrees of freedom is above 1, which indicates that the Tripp relation (Tripp 1998) do not account for all the sources of variability of SNeIa (see more in Section 5.3.2 and 5.3.2). (Betoule et al. 2014) suggested the addition of another uncertainty source known as σ_{coh} (and σ_{int} in this document) to model the scatter of the Hubble residuals. The σ_{int} quantity is estimated with the REML (*Restricted Maximum Likelihood*), defined as follows:

$$REML = \sum_n w_n(\mu_n - \mu_{th})^2 - \sum_n \log(w_n) + \log\left(\sum_n w_n\right), \tag{5.4}$$

where $w_n = C_{nn}^{-1}$ are the diagonal terms of the inverse of the covariance matrix, namely $(\sigma_n^2 + \sigma_{int}^2)$ from Equation (5.3).

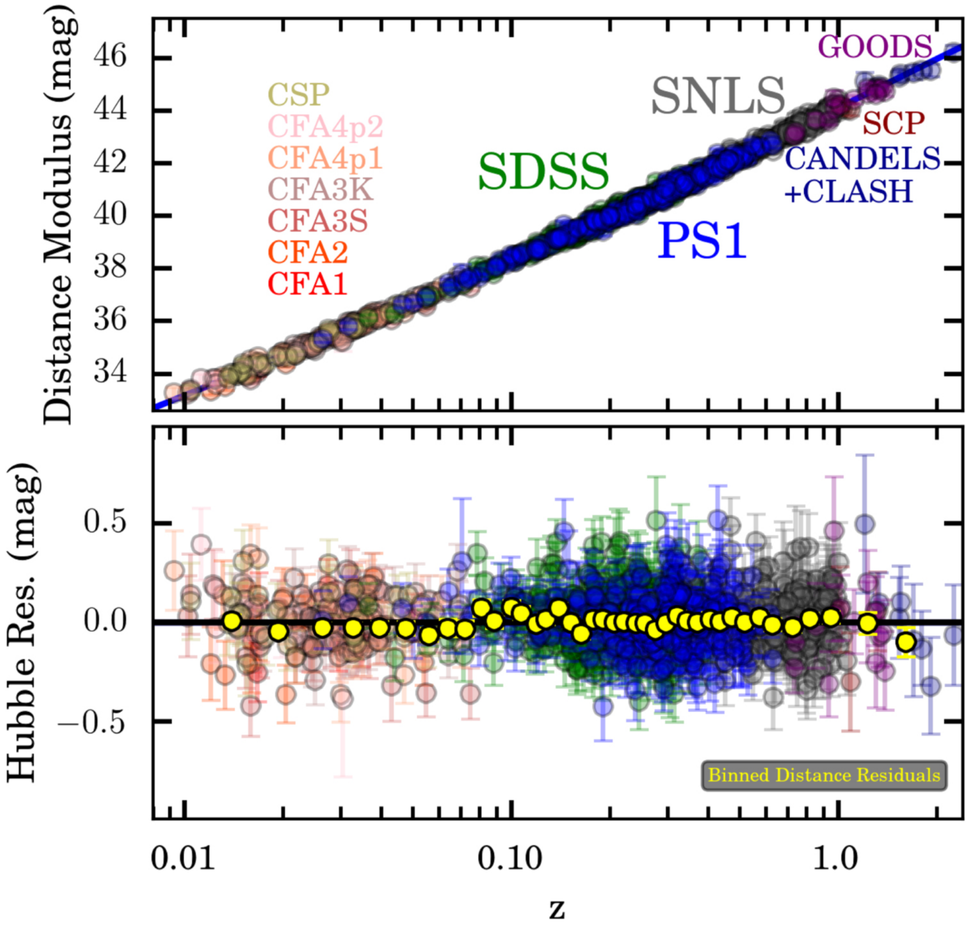

Figure 5.6: The Hubble diagram for the Pantheon sample. ***Top panel:*** the distance modulus for each SNIa as a function of redshift. ***Bottom panel:*** residuals of the Hubble diagram to the best fit cosmology. *Figure from Scolnic et al. 2018*.

5.3 Uncertainties and limitations of SNeIa

To precisely measure any cosmological quantity with SNeIa as a probe, we need to account for all known uncertainties of SNeIa measurements from observing stages with the telescope to the standardisation model passing by established correlations impacting the measurements. In this section, we will present all the known sources of uncertainty and limitations in the use of SNeIa as distance indicators.

5.3.1 Systematic and statistical errors

Photon noise

When measuring fluxes with CCDs, there are several sources of noise. It includes photon noise (or shot noise), readout noise, dark current noise and processing noise. For most observations, the photon noise dominates over all the other sources. Photon noise obeys counting statistics, modeled by Poisson process. Therefore, the scatter (σ) for the number of photons measured in the CCDs (N_{ph-e}) should follow: $\sigma = \sqrt{N_{ph-e)}}$. SNeIa flux measurements are, in fact, the contribution of fluxes from SNeIa (f_{SN}), the sky background (f_{sky}) and the host galaxy (f_{host}). Gathering all the information, we can obtain the *Signal-to-Noise Ratio* (SNR) formula for SNeIa flux:

$$SNR \equiv \frac{N_{SN}}{\sqrt{N_{SN} + N_{sky} + N_{host}}} \equiv \frac{f_{SN}}{\sqrt{f_{SN} + f_{sky} + f_{host}}}. \tag{5.5}$$

To get the evolution of the SNR with integration time, we can write the signals as $N_{SN} = tR_{SN}$, $N_{sky} = tR_{sky}$ and $N_{host} = tR_{host}$. Here, t corresponds to the integration time in seconds and (R_{SN}, R_{sky}, R_{host}) are the counting rate of respectively the SNIa, the sky and the host-galaxy in count s^{-1}. We can then write :

$$\begin{aligned} SNR &\equiv \frac{tR_{SN}}{\sqrt{tR_{SN} + tR_{sky} + tR_{host}}} \\ &\equiv \sqrt{t}\frac{R_{SN}}{\sqrt{R_{SN} + R_{sky} + R_{host}}} \end{aligned} \tag{5.6}$$

And from this, the dependence of SNR on time is:

$$SNR \propto \sqrt{t} \tag{5.7}$$

The SNR evolves as the square root of the integration time. To improve the SNR, we can observe longer. The longer we observe, the greater the sky noise, but the SNR increases since the SNIa signal increases linearly with the exposure time and the sky noise as the square root of the exposure time. In practice, the time exposure is a balance between the highest SNR, the CCD saturation level for night stars and the integrated image artefacts like aircraft/satellite tracks or cosmic rays, which increase the time exposure.

Calibration errors

The main systematic uncertainties on the measured distances from SNeIa are the calibration ones. Reviews on SNeIa calibration for cosmology purposes can be found on (Regnault et al. 2009; Betoule et al. 2013). One crucial step is the photometric calibration, namely the estimation of the Zero Point (ZP). This stage of calibration is described for the ZTF telescope in Chapter 4. With the ZTF photometric calibration pipeline, the flux precision is about 2% (Masci et al. 2018). Betoule et al. 2014 showed that the calibration uncertainties are the dominant source of systematic uncertainties on their analysis. Furthermore, they propagated the contribution of this source uncertainties to the total error in the determination of the matter density parameter Ω_m and found it at 37%. In Chapter 4, we discuss the limitations of the current ZTF flux precision, the ongoing efforts on improving ZTF calibration and where my contribution stands.

SNeIa peculiar velocities

The measured redshift of SNIa is a combination of recession velocity due to the expansion of the universe (Hubble law, more in Section 1.16) and the peculiar velocity of the object. The latter has a typical scatter which increases with decreasing redshift. The usual value used is $\sigma_v \sim 300\ \mathrm{km\,s^{-1}}$, from (Perlmutter et al. 1999; Kessler et al. 2009). At low redshift, assuming distances go as cz/H_0, we can propagate this dispersion of peculiar velocities into uncertainty on the distance modulus:

$$\sigma_{\mu|z} = \frac{5\sigma_v}{cz\log(10)}. \tag{5.8}$$

To illustrate the effect, the uncertainty on distance modulus of one SN which is at $z = 0.01$ is 0.1 mag.

Errors from the spectrophotometric model

SALT2 model was trained on a specific dataset, we need to evaluate if with this training, the model enables to estimate unbiased SNeIa standardization parameters. (Mosher et al. 2014) used simulations and showed that with an "ideal" training data set and an ideal test one, we can recover all the input parameters of the simulation. However, using a more realistic training and test data set from a cosmological analysis sample like the Joint Light-curve Analysis (JLA) from (Betoule et al. 2014), the input parameters of the simulations are not recovered (in particular in the UV). It leads to an additional source of uncertainties on the spectrophotometric model and hence uncertainties on the distance measurements, estimated to about 0.03 mag in Mosher et al. 2014. To reduce these uncertainties value, we need larger training data set at different phases in poorly explored regions.

5.3.2 Corrections

Extinction along line of sight

Similarly to extinction caused by SNeIa host-galaxies dust, dust from the Milky way affects the measured flux of the objects. The extinction caused by the dust should be corrected for. It was first observed by (Cardelli, Clayton, and Mathis 1989), the study compared the apparent color of same spectral type stars observed in different lines of sight. With infrared data from CMB characterization experiment like COBE, dust maps have been constructed

(Schlegel, Finkbeiner, and Davis 1998) and (Schlafly and Finkbeiner 2011) are used to correct SNeIa measured fluxes.

Beyond stretch and color standardization : astrophysical biases

Beyond brighter-slower and brighter-redder correlations, other correlations may be useful to reduce the remaining absolute magnitude dispersion. In fact, a dependence between SNeIa absolute luminosity and their host-galaxies stellar mass has been observed. As illustrated in Fig 5.7 from Childress et al. 2013, SNeIa from massive host galaxies ($M > 10^{10} M_{\odot}$) are in average brighter than the ones from less massive host galaxies ($M < 10^{10} M_{\odot}$). This is the so-called "mass-step" correction. It divides the SNeIa into two populations.

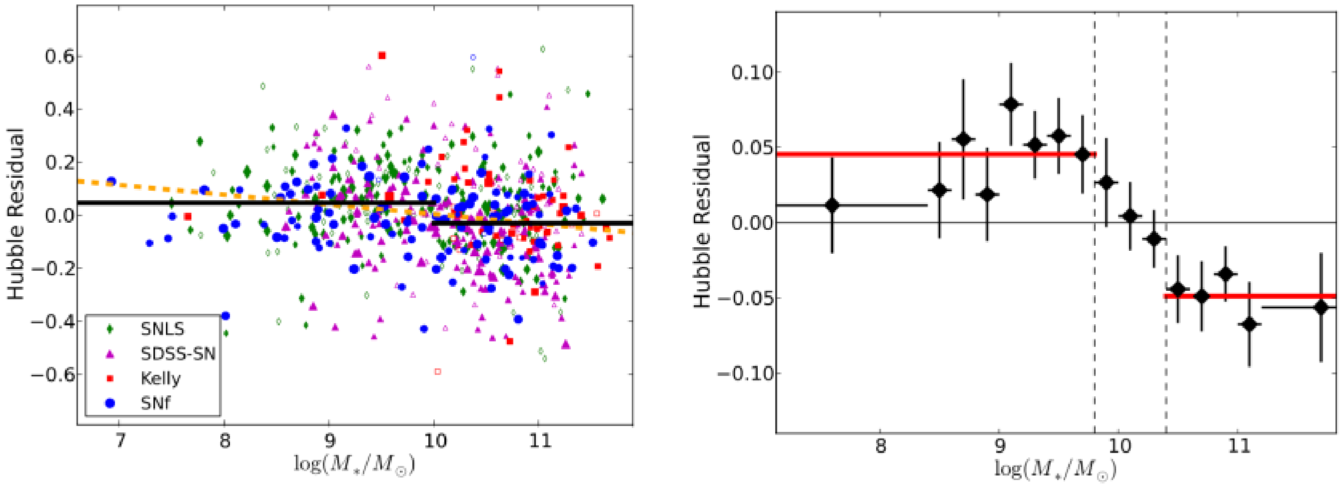

Figure 5.7: *Left:* Hubble residuals of a compilation of four SNeIa surveys showing the magnitude difference between SNeIa from host with a global stellar mass lower or higher than $10^{10} M_{\odot}$). Black lines is the mass-step and a linear trend in dashed orange line. *Right:* Binned in host mass Hubble diagram from the left figure. It illustrates the high and low-mass plateau and a transition at 10 dex. In (Childress et al. 2013), it is shown that the step function best describes the data. *Figures from Childress et al. 2013.*

A third parameter of standardisation is now accounted for in all recent cosmological analyses (Sullivan et al. 2010; Betoule et al. 2014; Scolnic et al. 2018), the standardised SNeIa absolute magnitude from Equation (5.1) for objects from massive host galaxies becomes :

$$\mu = m_B^* - M_B + \alpha x_1 - \beta c - \Delta M \tag{5.9}$$

The mass-step ΔM is fitted along with the cosmological parameters as presented before in Section 5.2.4, (Betoule et al. 2014) finds a mass step of 0.07 mag. The underlying origin of this effect remains unknown which questions the accuracy of the astrophysical bias corrections currently applied in SNeIa Cosmology.

Since this first discovery of the mass-step, significant correlation between standardised SNeIa magnitude and different host properties have been investigated (*e.g.* Kelly et al. 2010;

Sullivan et al. 2010; Lampeitl et al. 2010; Gupta et al. 2011; Childress et al. 2013; Roman et al. 2018; Smith et al. 2020; Pruzhinskaya et al. 2020; Rigault et al. 2013a). For example, Rigault et al. 2013b showed a first significant correlation between SNeIa brightness and local star formation activities (improved later in Rigault et al. 2013a). It indicates that SNeIa from old-population environments are 0.161 ± 0.031 mag brighter than these from younger environments, which constitutes the largest known environmental magnitude steps to date. The search for other correlations to reduce the absolute magnitude dispersion is a very active research field.

Residual scatter of SNeIa magnitudes

It is a source of uncertainty linked to the modelling of SNeIa. After the standardization of SNeIa using the stretch, color and host-galaxies correlation, a dispersion of about ~ 0.1 mag is found in the Hubble residuals (Betoule et al. 2014; Scolnic et al. 2018). It indicates that there are unknown sources of variability of SNeIa not accounted for with the current standardisation method using Equation (5.9). As discussed in Section 5.2.4, this effect is now taken into account following (Betoule et al. 2014).

5.4 Summary

Type Ia Supernovae are very bright transient objects, they enable us to probe the universe up to $z \sim 1$. Their luminosities are reproducible, if we take into account the existing correlations between photometric observables of SNeIa, it reduces their dispersion and makes them accurate distance indicators. Such measurements ultimately allow to test ΛCDM model in multiple but non-exhaustive ways like constraining the cosmological parameters or verify the Cosmological Principle through bulk flow measurements.

CHAPTER 6

SIMULATIONS FOR BULK FLOW MEASUREMENTS

In this chapter, we present our work on bulk flows detectability with ZTF-like simulations using the dipole method (Bonvin, Durrer, and Kunz 2006), introduced in Section 2.3. These simulations were developed in the context of ZTF first year sample (Data Release 1), referred to as DR1. In Section 6.1, we introduce the DR1 sample, followed, in Section 6.2 by the presentation of the framework of our simulations. In Section 6.3, we present our methodology to estimate bulk flows with our simulations and associated results.

6.1 DR1 sample study

In this section, we will briefly describe the DR1 sample, the fit of the light-curves with the SALT2 model (Guy et al. 2007), the standardisation of the sample and the Hubble residuals that follow from it.

6.1.1 DR1

The ZTF DR1 sample (Dhawan et al. 2021) consists of 761 spectroscopically confirmed SNeIa, with median redshift $\bar{z} = 0.057$, from first year operations. All the light-curves data are only on *ztfg* and *ztfr* bands. In this sample, 305 SNeIa have host galaxy redshifts, we apply furthermore cuts on the sample for a robust determination of the light-curves fit parameters, from (Dhawan et al. 2021).

6.1.2 Sample cuts

The following requirements applied on DR1 sample are based on (Dhawan et al. 2021). We require for SNIa at least 3 points in the light-curves within 10 days of maximum light. We fit the selected light-curves with SALT2 (Guy et al. 2007) using *SNCOSMO*[1]. Cuts on SALT2 parameters uncertainty are applied to remove objects with poor SALT2 fits: $\sigma(x_1) < 1$ or $\sigma(t_0) < 1\ day$. Furthermore, as the DR2 sample, presented in Section 3.2.1, the DR1 sample is contaminated by peculiar SNeIa, which tends to be sub-luminous. The traditional cuts to remove the peculiar SNeIa from the regular for cosmological studies are: $|x_1| < 3$ and $|c| < 3$. The redshift and SALT2 parameters of the final sample are represented in Fig 6.1. The distribution of the SALT2 parameters that we fitted on the DR1 sample is consistent with the ones driven by Dhawan et al. 2021. The distributions (from Fig 6.1) suggests more reddened SNeIa ($c > 0$).

6.1.3 Hubble residuals

From our final DR1 sample, from Section 6.1.2, constituted of 137 SNeIa displaying a median redshift of: $\bar{z} = 0.0623$, we derive the Hubble residuals (see Section 5.2.4). We use the magnitude-redshift relation on our sample to derive the intrinsic scatter (σ_{int}) value. We

---

[1] `https://sncosmo.readthedocs.io/en/stable/`

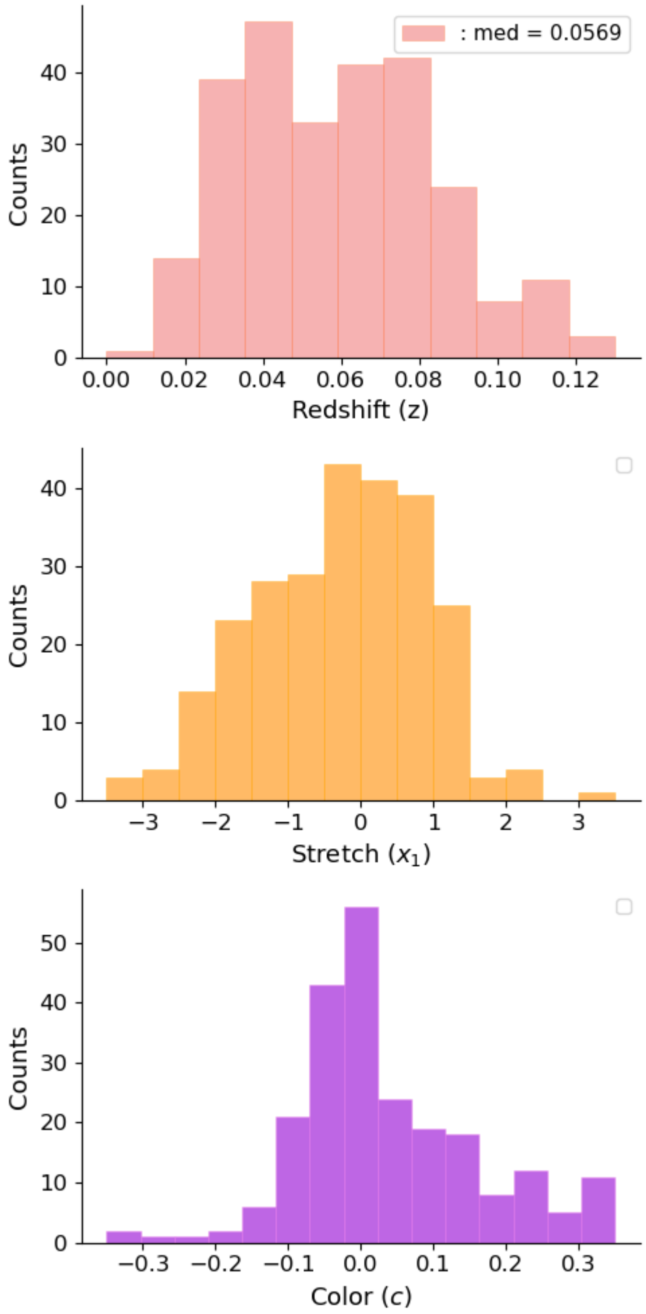

Figure 6.1: ***Top:*** redshift distribution of the DR1 sample. ***Middle:*** SALT2 stretch (x_1) distribution of the DR1 sample. ***Bottom:*** SALT2 color (c) distribution of the DR1 sample.

use the CMB redshifts that we obtain from the conversion of the heliocentric ones, following the methodology of Betoule et al. 2014. Our sample being only at low-z, we cannot estimate cosmological parameters describing the constituents of the Universe. We fix Ω_M, portion of baryonic and ordinary matter in the Universe to $\Omega_M = 0.27$ and the Hubble constant to $H_0 = 68\ \mathrm{km\,s^{-1}\,Mpc}$ (Planck Collaboration et al. 2020)

We adapted the REML (*Restricted Maximum Likelihood*) method defined in Equation (5.4) from (Betoule et al. 2013):

$$REML = \sum_n \left(\frac{\mu_{obs,n} - \mu_{th,n}}{\sigma_{\mu,n}}\right)^2 + \sum_n \log(\sigma_{\mu,n}) - \log\left(\sum_n \sigma_{\mu,n}\right), \tag{6.1}$$

with the index n corresponding to the number of SNeIa, the theoretical distance modulus (μ_{th}) is computed from distance luminosity Equation (2.6), μ_{obs} is the observed distance modulus from Equation (5.1) and $\sigma_{\mu,n}$ is the uncertainties on the distance modulus as in Dhawan et al. 2021, for each SNIa:

$$\sigma^2_{\mu,n} = \sigma^2_{fit} + \sigma^2_{\mu,z} + \sigma^2_{int}. \tag{6.2}$$

The first term (σ_{fit}) corresponds to the contribution of the SALT2 fit uncertainties, derived from the SALT2 covariance matrix for a given value of α and β. The second term ($\sigma_{\mu,z}$) is the peculiar velocity error (σ_v), propagated in the distance modulus like in Equation (5.8), see Section 5.3.1 for more details, and is set to $\sigma_v = 300 \mathrm{km\,s^{-1}}$ (Perlmutter et al. 1999; Kessler et al. 2009). The last term, σ_{int}, corresponds to the intrinsic scatter of SNeIa, detailed in Section 5.3.2. This REML inference technique allows to robustly infer σ_{int} all together with the nuisance parameters (α, β) and the absolute M_B from Equation (5.1). Combining all these elements in Equation (6.1) that we minimise, we find that the intrinsic scatter of the sample is: $\sigma_{int} = 0.135$ mag.

We used the fitted parameters to build the Hubble diagram and its residuals for our sample in Fig 6.2. Top figure shows the comparison of the ΛCDM predictions (in solid line) to the observed distance modulus, of each SNIa, from Equation (5.1) corrected with the fitted parameters, in function of the sample redshift. The data points are well distributed around the theoretical distance modulus, indicating that we have reproduced the Hubble Law with ZTF measurements and that they are all consistent with ΛCDM expectations. We can notice a stronger scatter of the data points at low redshift (z < 0.03) which is explained by the dominance of SNeIa peculiar velocities over the cosmic expansion. Bottom of the same figure (Fig 6.2) shows the evolution of the Hubble residuals from the Hubble diagram in function of the redshift and their distribution. No bias is observed in the residuals which are consistent with 0, they are distributed homogeneously following a Gaussian distribution. We compared our fitted value of σ_{int} to the one from Dhawan et al. 2021, they found $\sigma_{int} = 0.15$ mag. For the same sample we measured a smaller dispersion. This difference can be due to the fitting approach, they derive posterior distributions on the parameters and pick the best fit values.

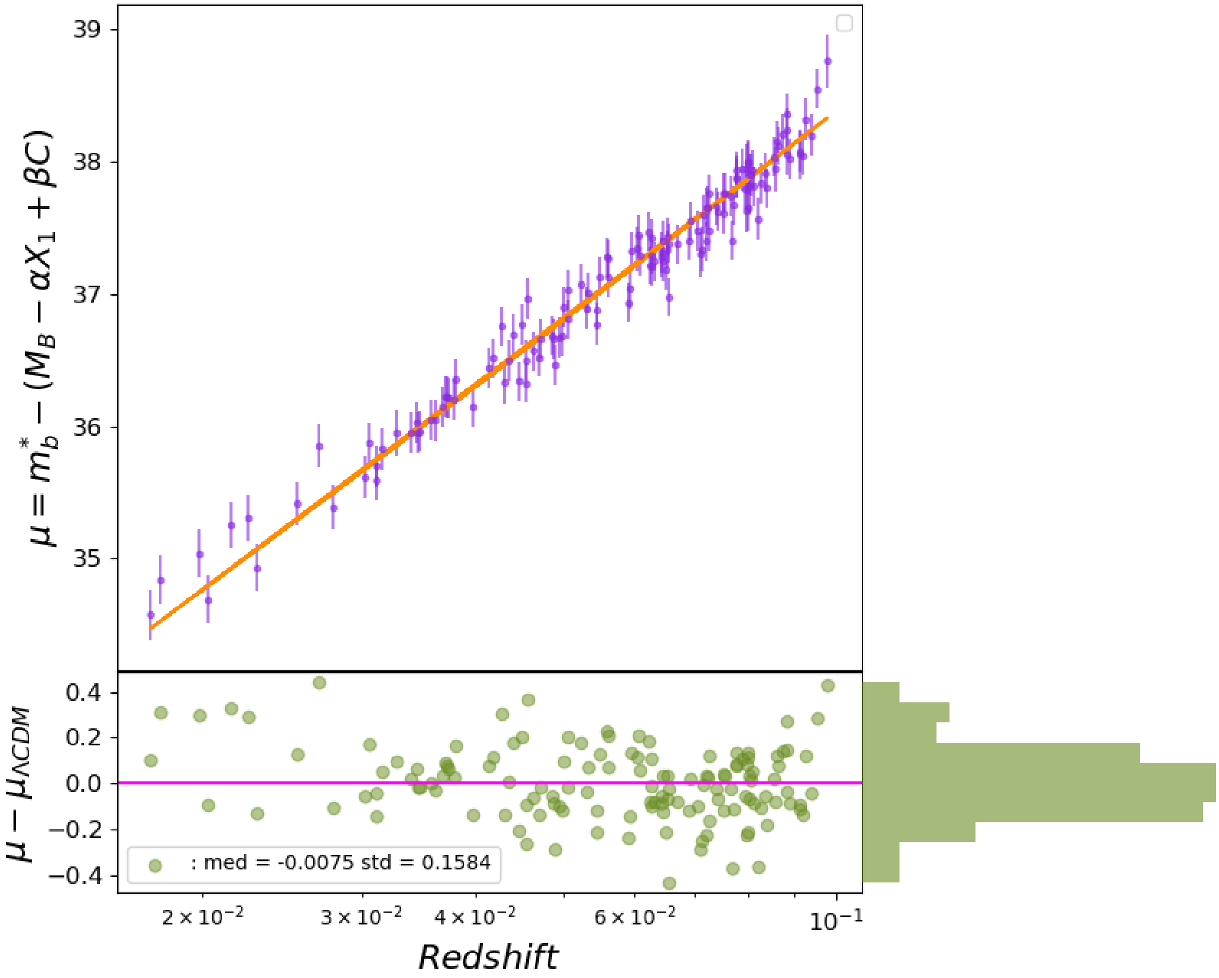

Figure 6.2: Hubble diagram and its residuals for the ZTF DR1 sample.

6.2 Simulation framework

To develop the bulk flows analysis and estimate their detectability, we started by setting up a fast simulation based on ZTF DR1 Hubble diagram. In this section, we present our simulated sample and its associated Hubble residuals.

6.2.1 Coordinates and redshifts

We generate couples of Equatorial coordinates (α, δ) using *Healpy*[2] python package, uniformly across the sky. To each couple of coordinates, we associate a heliocentric redshift

---

[2] https://healpy.readthedocs.io/en/latest/tutorial.html

driven from a uniform distribution and compute the redshifts in the CMB rest-frame, following (Betoule et al. 2014) methodology. The redshift distribution and the associated location in Galactic coordinates are represented in, respectively, left and right of Fig 6.3 for 800 SNeIa.

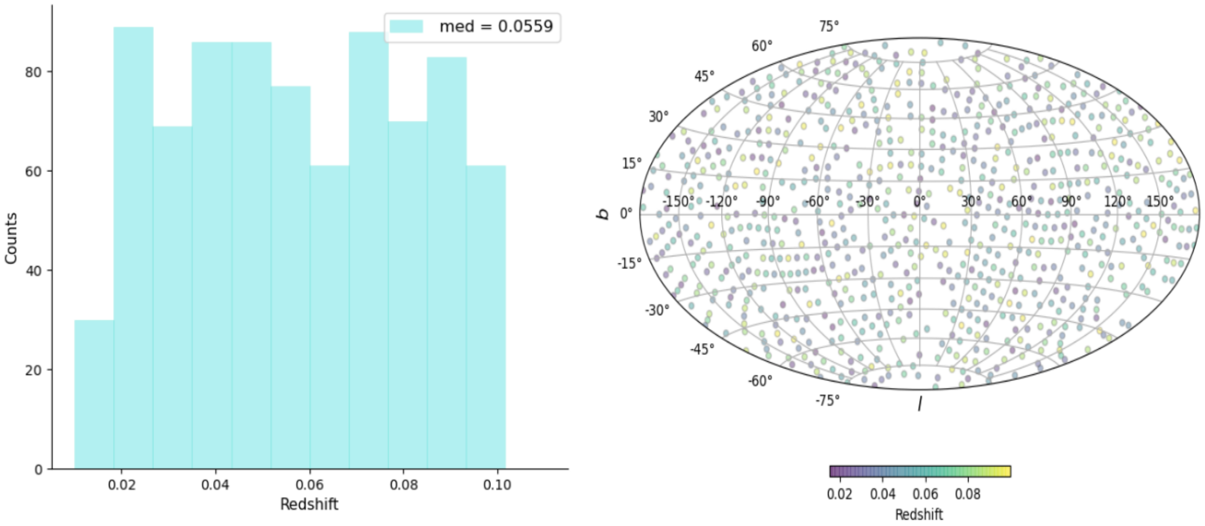

Figure 6.3: *Left:* example of redshift distribution for one set of simulations. *Right:* distribution of one set of simulation in Galactic coordinates.

6.2.2 Distances modulus and associated uncertainties

We aim to simulate faithful observed distances modulus for each set of (α, δ, z) with their associated uncertainties. From the generated redshifts, we compute luminosity-distances from Equation (2.6), then using Equation (2.8) we obtain distance modulus for each z. Since the generated distances modulus are theoretical values, we add noise to their values correlated with the measured uncertainties.
We generate distance modulus uncertainties based on the DR1 ones. As introduced in Section 6.2, there are three contributions to distance modulus uncertainties: SALT2 fit uncertainties, peculiar velocities and intrinsic scatter. Since we simulate directly standardised distances, we cannot account for the SALT2 fit uncertainties on our simulations. Therefore, we use the properties of the DR1 fit uncertainties (σ_{fit}) distribution, in Fig 6.4.

As a first approximation, we use the mean and standard deviation of the DR1 fit uncertainties in a randomised normal distribution $N(\mu, \sigma^2)$ for our simulated uncertainties. We also account for peculiar velocities uncertainties on the distance modulus as following:

$$\sigma^2_{\mu,sim} = N^2(\mu_{DR1}, \sigma_{DR1}) + \sigma^2_{\mu,z}, \tag{6.3}$$

with $N^2(\mu_{DR1}, \sigma_{DR1})$ corresponding to the equivalent of σ^2_{fit}, μ_{DR1} and σ_{DR1} are respectively the associated mean and standard deviation of DR1 (see Fig 6.4). The second term

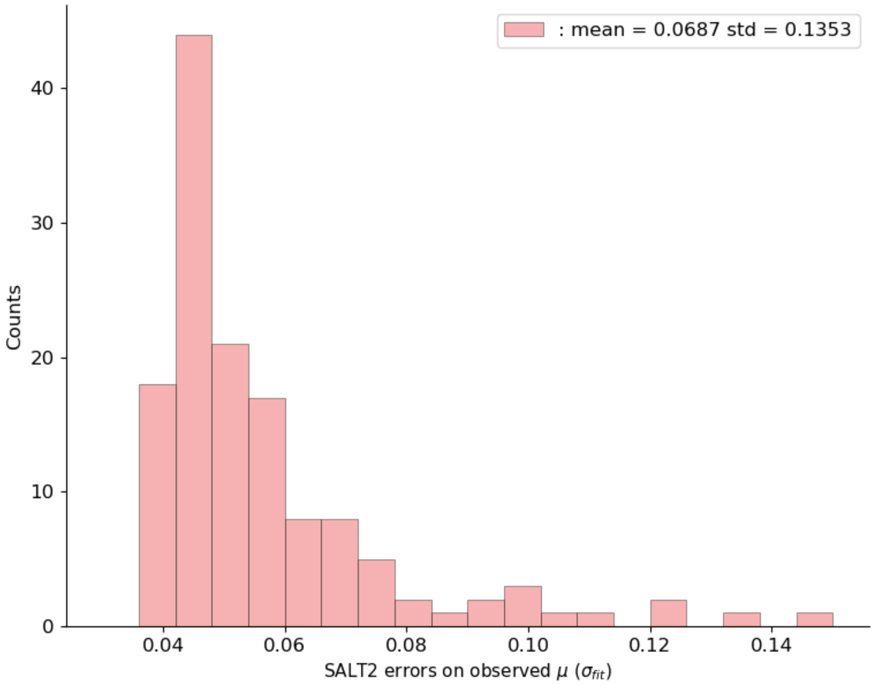

Figure 6.4: Distribution of the SALT2 fit errors on the DR1 sample used to generate the equivalent of fit uncertainties for the simulations. Std stands for standard deviation.

is the peculiar velocity error (σ_v) propagated in the distance modulus, same as in Equation (6.2) (more details in Section 5.3.1) and uncertainty on peculiar velocity is set to $\sigma_v = 300\ \mathrm{km\,s^{-1}}$ (Perlmutter et al. 1999; Kessler et al. 2009).

Once the errors are simulated, we add randomly a correlated noise to the distance modulus to make them more realistic, as following:

$$\tilde{\mu}_{sim} = \mu_{sim} + N(0, \sigma^2_{\mu,sim}) + N(0, \sigma^2_{int}), \tag{6.4}$$

with μ_{sim} the theoretical distance modulus (from Equation (2.8)), $N(0, \sigma^2_{\mu,sim})$ corresponds to a randomised normal distribution centered on 0 with the standard deviation of the simulated fit uncertainties and $N(0, \sigma^2_{\mu,int})$ normal distribution centred on 0 and its dispersion value being σ_{int}, the intrinsic scatter fitted on the DR1 sample from Section 6.1.3.

Finally, we add the intrinsic scatter to the simulated distance modulus uncertainties from Equation (6.3):

$$\sigma^2_{\mu,sim} = N^2(\mu_{DR1}, \sigma^2_{DR1}) + \sigma^2_{\mu,z} + \sigma^2_{int}. \tag{6.5}$$

We compare the normalised distributions of the simulated uncertainties on distance modulus and the DR1 ones in Fig 6.5. We can notice that the distance modulus uncertainties distribution reproduces qualitatively the one from the DR1, but with a left tail giving a smaller mean value and a bigger dispersion.

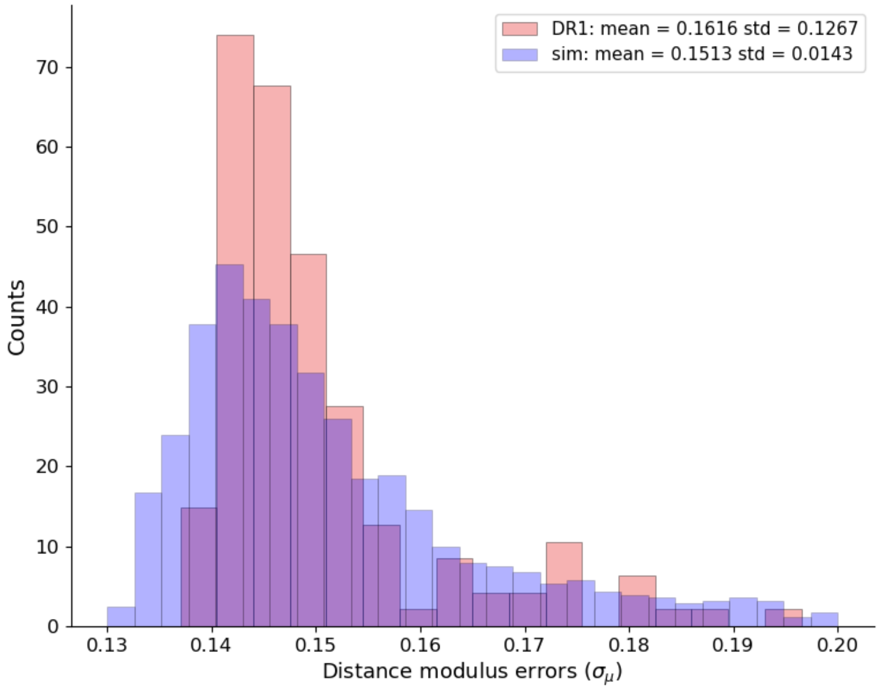

Figure 6.5: Comparison of the distributions of DR1 uncertainties on the distance modulus from Section 6.1.3 and the simulated ones from Equation (6.5).

6.2.3 Hubble diagram

We generate SNeIa redshifts, coordinates, distance modulus and associated distance modulus uncertainties. We construct the Hubble diagram and fit for the intrinsic scatter. Fig 6.6 shows an example of Hubble diagram built with one sample of our simulations. It is consistent with the DR1 Hubble diagram in Fig 6.2.

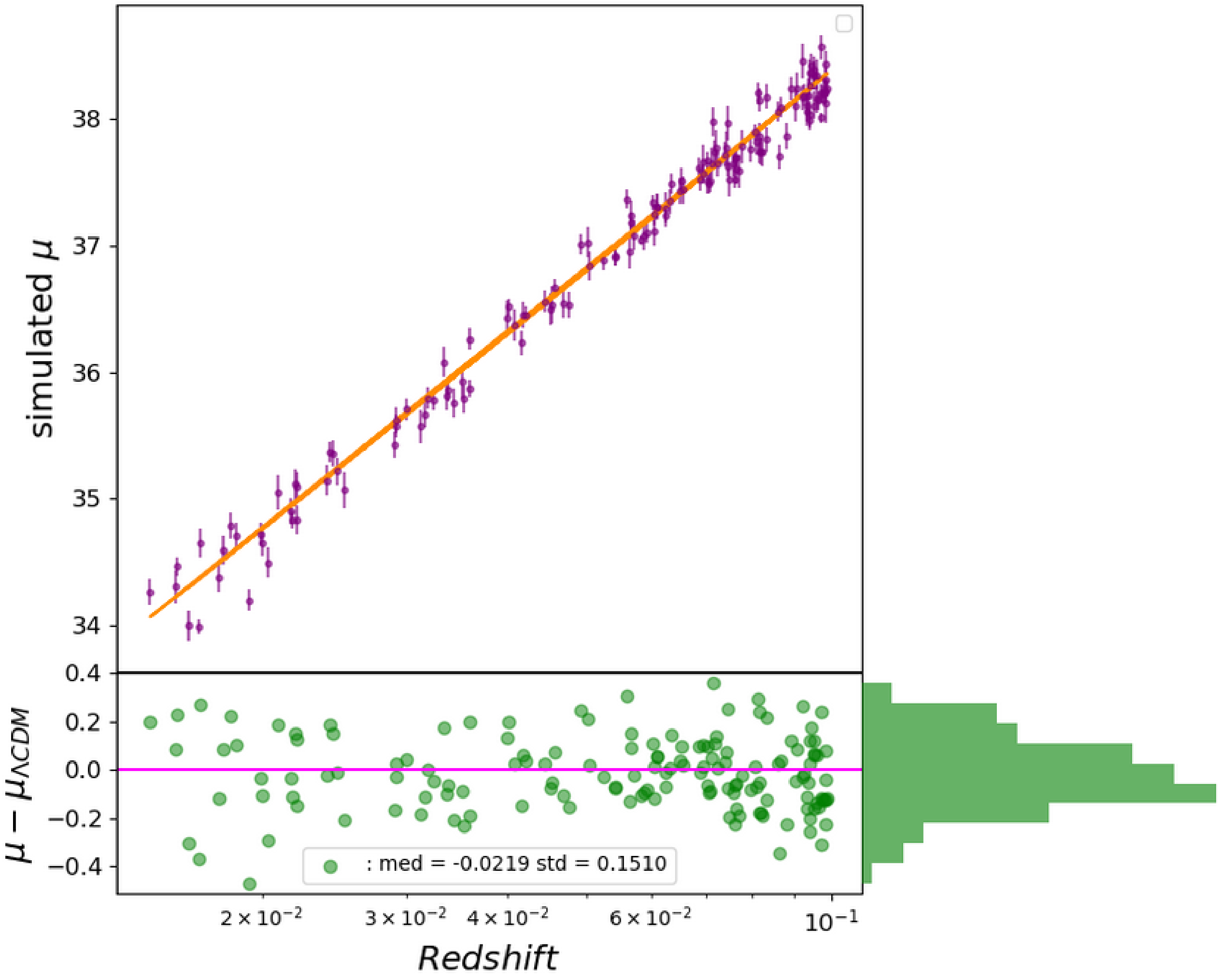

Figure 6.6: Example Hubble diagram for one sample built with our simulation framework.

6.3 Bulk flows detection

We aim to estimate the detectability of local bulk flows with ZTF SNeIa data. For this purpose, we simulate 1000 samples generated following the method described in Section 6.2. Each sample consists of 800 SNeIa with associated redshift, location in the sky, distance modulus and derived uncertainties. To ensure the accuracy of our simulated samples, we fit the Hubble residuals for each one of them and verified the intrinsic scatter of all the samples.

6.3.1 Methodology

We applied the dipole method introduced in Section 2.3 and based on (Bonvin, Durrer, and Kunz 2006), for each of the 1000 samples. As seen before, this approach consists of introducing a term in the luminosity distance of the dipole probes, SNeIa for our study. Taking one SNIa with Galactic coordinates (l_i, b_i) and redshift z_i, the dipole luminosity distance from Equation (2.22) becomes

$$d_L^{(1)}(z_i, l_i, b_i; v_d, l_d, b_d) = \frac{(1+z_i)^2 v_d}{H(z_i)} \cos\left(\Delta\Theta(l_i, b_i, l_d, b_d)\right), \tag{6.6}$$

where $\Delta\Theta$ is the angle between the SNIa position (l_i, b_i) and the direction of the dipole (l_d, b_d) in Galactic coordinates, while v_d refers to the magnitude of the dipole velocity (in $\mathrm{km\,s^{-1}}$). The angular separation can be expressed from the projection of the unit vectors

$$\cos\left(\Delta\Theta(l_i, b_i, l_d, b_d)\right) = \sin b_i \sin b_d + \cos b_i \cos b_d \cos(l_i - l_d). \tag{6.7}$$

We therefore can estimate the velocity and location of the dipole per redshift shells for each simulated sample using the minimum chi-square (χ^2) estimation. The χ^2 is expressed as:

$$\chi^2 = \sum_{i=1}^{n} \frac{\left(\mu_i - \left(5\log_{10}(d_L(z_i) - d_L^{(1)}(z_i, l_i, b_i, ; v_d, l_d, b_d)) + 25\right)\right)^2}{\sigma_i^2}. \tag{6.8}$$

The sum is over the number of SNeIa in the redshift shell, μ_i are the observed distance modulus from our simulation and σ_i their associated uncertainties (more detail in Section 6.2.2), $d_L(z)$ is the luminosity distance defined in Equation (2.6) and $d_L^{(1)}(z)$ is the dipole luminosity distance defined in Equation (6.6). We can notice the change of sign in front of $d_L^{(1)}$, when compared to Equation (2.21). This is needed because we use the observed redshifts that include the effect of peculiar velocities.

From Equation (6.6), we can see that the dipole velocity amplitude is used as a linear coefficient. Therefore, mathematically negative values are allowed. To avoid this scenario, we can set lower limit in the fit for $v_d \geq 0$. An alternative option is to express $\mathbf{v}_d$ in Cartesian coordinates (v_x, v_y, v_z) and the dipole terms becomes:

$$d_L^{(1)}(z_i, l_i, b_i; v_x, v_y, v_z) = \frac{(1+z_i)^2}{H(z_i)} \left(v_x \cos b_i \cos l_i + v_y \cos b_i \sin l_i + v_z \sin b_i\right). \tag{6.9}$$

6.3.2 Results

We minimise Equation (6.8) to estimate the Cartesian components (v_x, v_y, v_z) of the dipole velocity ($\mathbf{v}_d$) per redshift shell for each simulated sample. We use python package *iminuit* for the χ^2 minimisation. We have represented the distributions of the fitted velocity components for the 1000 samples, for each redshift shell in Fig 6.7 and their associated uncertainties (σ_{v_x}, σ_{v_y}, σ_{v_z}), derived from the minimiser, in Fig 6.8. In both figures, m and s refer to, respectively, the mean and standard deviation of the distributions. Each row, from both figures, corresponds to a redshift shell. The Cartesian components and their associated error distributions display Gaussian shape, for all the redshift shells. The velocity distributions, along with their associated uncertainties are consistent with 0, confirming the absence of any bias. The dispersion of the Cartesian velocities and the peak values of their associated uncertainties increase with the redshift as expected since the distances get noisier. We can also notice that the mean value of the velocity component uncertainties σ_{v_i} are consistent with the standard deviation of the component distributions v_i for each redshift shells.

We compute the amplitude of the dipole velocities using the fitted Cartesian components, as follows: $v_d = \sqrt{v_x^2 + v_y^2 + v_z^2}$. Left of Fig 6.9 represents v_d distributions per reshift shell, for the 1000 simulated samples. In addition to the dipole velocity magnitude, we determine the location, in Galactic coordinates (l_d, b_d), of the dipoles for all our samples with the conversion of Cartesian coordinates to spherical ones. Right of Fig 6.9, we show the distribution of the fitted dipoles, in the galactic plane, for all the samples, colored per dipole velocity magnitude. Each row of the figure corresponds to a specific redshift shell. No preferred dipole direction is found, indicating the consistency of the simulations.

Comparison with ΛCDM predictions

To assess the detectability of bulk flow measurements with our simulations, we compare the distributions of v_d from Fig 6.9 (left) to ΛCDM predictions. In Fig 6.10, we have represented bulk flow amplitudes from ΛCDM model (see Section 2.2 for more details) in function of the redshift with a Gaussian window function. In the same figure, we have represented the mean values of v_d distributions per redshift shell, the error bars on the data points are the standard deviation of the associated distributions. Our statistical analysis using a simple dipole inference (Bonvin, Durrer, and Kunz 2006) cannot allow the detection of bulk flow velocities below limits set by v_d, only values above can be interpreted as significantly inconsistent with null values.

6.4 Conclusion and perspectives

We present the ZTF DR1 sample made of 761 spectroscopically classified SNeIa, from (Dhawan et al. 2021). We fit the light-curves of this sample with the SALT2 model (Guy et al. 2007). After traditional cosmological criteria, we fit the Hubble residuals and found the intrinsic scatter of the sample at $\sigma_{int} = 0.135$, smaller than the value fitted in (Dhawan et al. 2021). We study the detectability of bulk flows with simulations DR1 like. To this end, we generate 800 SNeIa defined by their equatorial coordinates, redshift, distance modulus and their associated uncertainties. We seek to simulate the most truthful uncertainties, therefore, we use the characteristics of the DR1 distance modulus uncertainties distribution in our simulations. We apply the dipole method (Bonvin, Durrer, and Kunz 2006) to the simu-

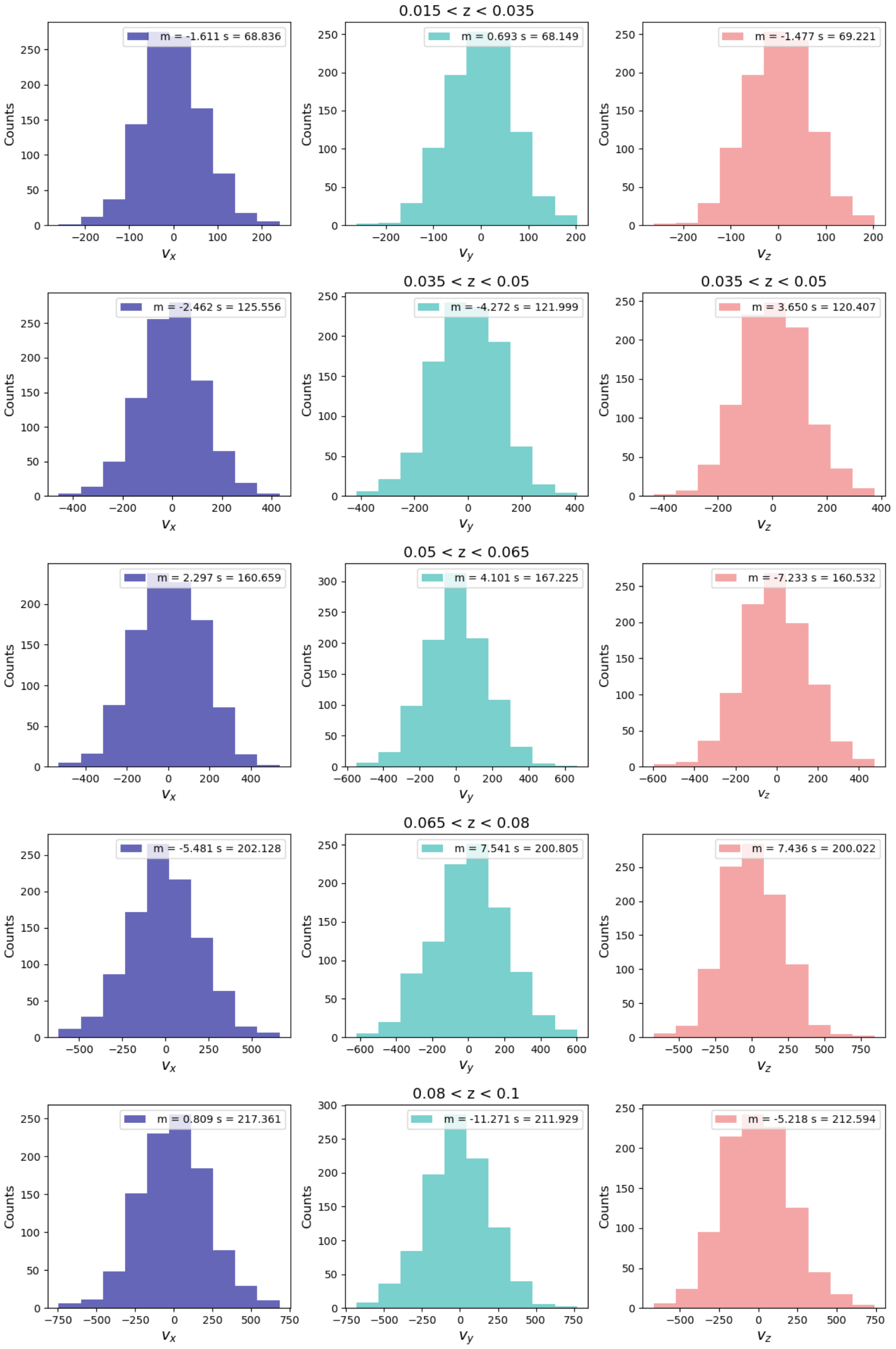

Figure 6.7: Distributions of the fitted Cartesian dipole velocities (v_x, v_y, v_z) for each redshift shell. In the legend, "m" and "s" correspond to respectively the mean and standard deviation of the distributions. Each row represent the (v_x, v_y, v_z) distributions for the same redshift shell, while each column represents the distribution of the same v_i component for different redshift shells.

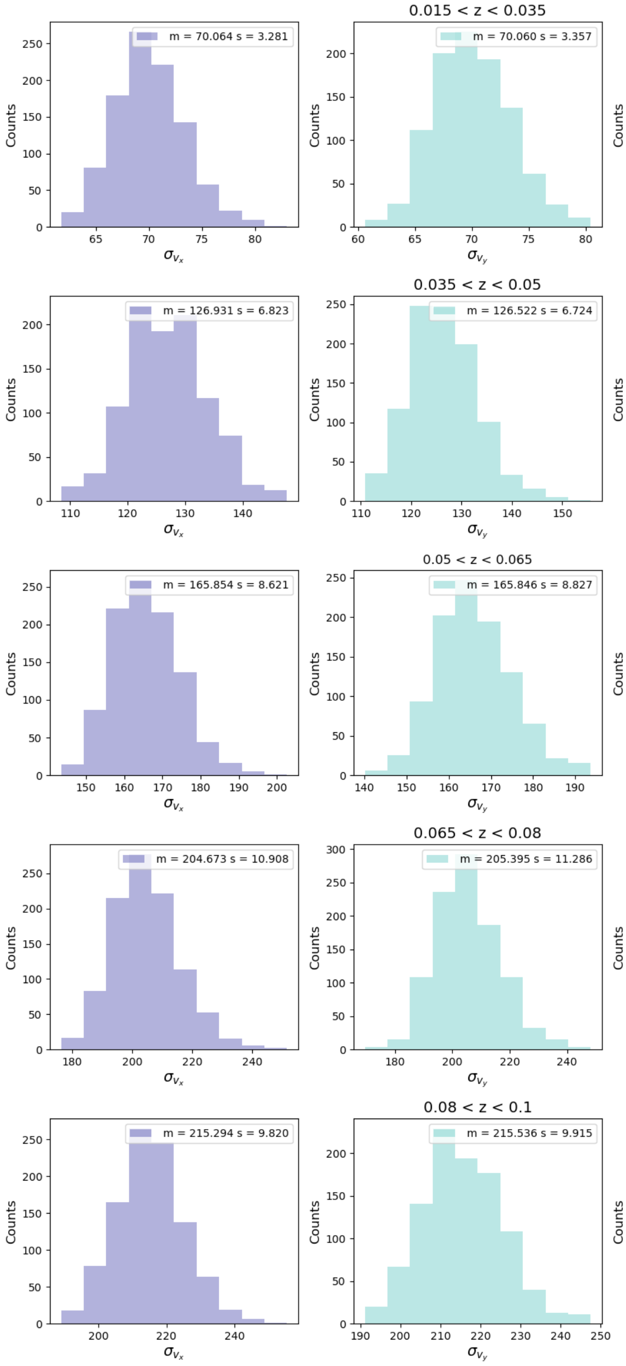

Figure 6.8: Distributions of the uncertainties on the fitted Cartesian dipole velocities (σ_{v_x}, σ_{v_y}, σ_{v_z}) for each redshift shells. In the legend, "m" and "s" correspond to respectively the mean and standard deviation of the distributions. Each row represent the (σ_{v_x}, σ_{v_y}, σ_{v_z}) distributions for the same redshift shell, while each column represents the distribution of the same σ_{v_i} component for different redshift shells. soutThe distributions are Gaussian and centered on higher values with higher redshifts. For a given redshift shell, the velocity uncertainties distributions are similar and centered on close values.

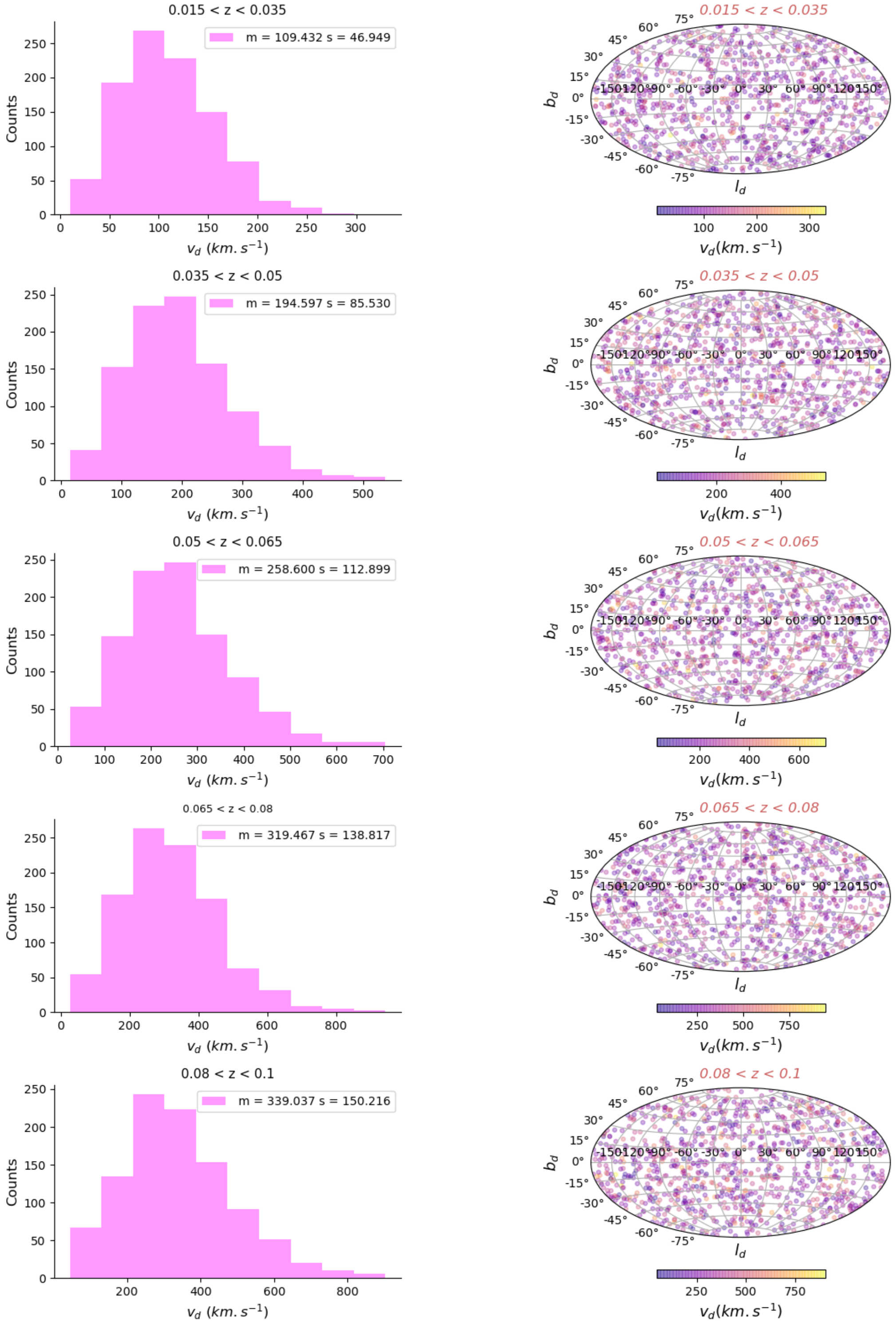

Figure 6.9: Distributions of the reconstructed dipole velocity v_d (left) and their sky position in galactic coordinates (right). In the legend, "m" and "s" correspond to respectively the mean and standard deviation of the distributions. Each row represent a redshift shell.

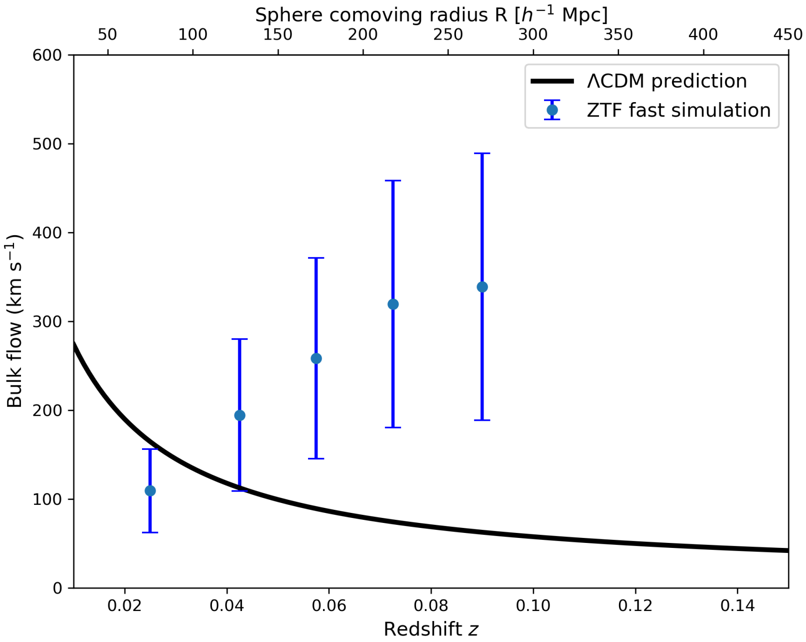

Figure 6.10: ΛCDM predictions of bulk flows amplitudes in function of the redshift or the comoving distance compared to the detections of our simulations.

lated sample that we divide per redshift shells. We estimate the Cartesian components of the dipole velocities, their distributions are consistent with 0. We reconstruct the dipole velocity v_d and coordinates (l_b, b_d) from the Cartesian components. No preferred direction of dipole is noticed with the reconstructed coordinates. With the method used to infer the bulk flow amplitudes, the detection limits of significant non-null bulk flow amplitudes are higher than ΛCDM predictions.

These results are subject to multiple changes. As mentioned before, the simulations used for this study are part of a preliminary work. We can use more realistic simulations, in particular the ones we develop in the next Chapter (7). ZTF has been running successfully for five years. This study is based on the DR1 sample, only first year of ZTF observations. For the final release of ZTF, we will have 5 times more SNeIa and therefore the errors on v_d would be $\sqrt{5}$ times smaller. This would unlock detection of bulk flows in the local Universe with ZTF. The other point that we can change in our analysis is the inference method, with which by definition v_d is always inconsistent with 0. We can apply other bulk flow estimation techniques addressed at the end of Section 2.3.

Chapter 7

ZTF SNeIa realistic simulations

In Chapter 6, we show that ZTF could measure Bulk Flows, in the nearby Universe, if we have a large and unbiased sample. Now that ZTF has been running for five years, any precision cosmology analysis requires to understand how the sample is selected, identify the biases and correct for them, where applicable. To measure Bulk Flows with ZTF data, we need to assess their biases, for example if the sample preferentially select bright SNeIa at different redshifts, it could appear like a bulk flow effect when in reality it is a selection effect. To investigate the biases in the sample, we use realistic simulations: forward model all aspects of the survey from our understanding of SNeIa to the actual survey strategy (including all known effects that dictate the survey) and compare to the data. We simulate ZTF DR2 sample (see Section 3.2) using this technique, two outcomes are possible for our studies. The first one would be that the simulations replicate the data, it implies that we understand the sample and all the effects dictating it. The second outcome, our simulations are in disagreement with the DR2. Since we accounted for all the known effects from the sample in our simulations: there must be unknown systematic errors in the sample.

In Section 7.1, we introduce the simulation framework with the SNeIa model and a full description of the observing information used. In Section 7.2, we use the measured parameters of SNeIa with the true observing cadence of ZTF to reproduce every individual object from the DR2 sample. In Section 7.3, we rely on comparison of underlying population of x_1 and c, drawn from realistic simulations, with their associated fitted values to predict biases in the distance measurements with ZTF. The DR2 sample, introduced in Section 3.2, is constituted of only spectroscopically classified SNeIa, in the final section (7.4), we aim to replicate this sample with our realistic simulations and study its selection.

7.1 Setting the simulations framework

Simsurvey (Feindt et al. 2019) was designed to generate transient light-curves, given the survey observing schedule and the model of the targeted transient. It was designed to predict transient survey discovery rate and was used to this end for ZTF. In this section, we will introduce the elements we input to simsurvey to replicate the DR2 sample and investigate the accuracy of the simulations. To make realistic simulations of ZTF SNeIa, we take physical models that account for all our knowledge about SNeIa and ZTF real-time observing conditions summarized in logs: when ZTF observed, which paths of the sky and the sky brightness. In the following section, we will present the transient model used, the observing logs and how they are combined in simsurvey to produce SNeIa light-curves.

7.1.1 Transient model

Simsurvey is focused on SNe simulations, SNeIa and core-collapse SNe like Ib/c, IIn and IIP. There are multiple transient models implemented in the code. Below are the main input to the transient model part of simsurvey:

- transient type,
- transient template,

- redshift range,
- location range in equatorial coordinates (α, δ),
- range of date of maximum luminosity (t_0, in MJD),
- map of the Milky Way dust extinction,
- number of transient to simulate (*optional*, SNeIa rate can be used).

For our work with SNeIa, we used state-of-the-art template of SNeIa : SALT2, introduced in Chapter 5, from (Guy et al. 2007). Stretch x_1 and color c parameters are driven from Gaussian distributions, represented and used to assess DR2 spectroscopic selection function in Section 7.4. Redshifts are determined from an uniform distribution, and the transient coordinates are drown from a uniform distribution down to declination $\delta = -30°$, the farthest south part that ZTF could observe.

For our work in Section 7.2, we add a feature in simsurvey to enable to input x_1, c, t_0, z and (α, δ) values for each simulated object. Therefore, we could use the measured properties of the DR2 objects as input to the simulations and compare them.

7.1.2 Survey schedule

As introduced in Section 3.2 from Chapter 3, the DR2 sample extends over the entire duration of ZTF phase-I. Since we sought to replicate the whole sample with simsurvey, we need to use all the associated true observing strategy of ZTF phase-I. The true observing strategy is all the information about the survey observations, we shall refer to it as observing logs too. They are organised in a file, compiled from metadata, each line represents one observation from one ZTF quadrant in a given band. For example, for one random night in July 2018, they are more than $40,000$ observations in *ztfg* and *ztfr* bands across all the focal plane. The observations from this file include the main public survey (MSIP) and partnership observations (see Chapter 3). These observing logs cover the entire ZTF phase-I, including all transient observations not exclusively SNeIa ones. For consistency, we checked that the DR2 objects matched the observing logs and ensured that all SNeIa observations were included. To sum up the content of the file, below are the columns used for the simulations as ZTF survey schedule in simsurvey:

- obsmjd of the observation (time in MJD),
- ccd number of the observation,
- quadrant number of the observation ,
- field number and equatorial coordinates (α, δ) of the observed patch of the sky,
- band of the observation (ZTF filter),

- limiting magnitude ($maglim$) which is the 5-σ magnitude limit of each image (see Section 3.1.2).

There are two additional, yet optional, information we can input to simsurvey: ZP and gain. The Zero Point ZP can be input whether per observation or as one global value per band. The default value that simsurvey uses, if none is given is : 30. The gain, as introduced in Chapter 4, can be input in simsurvey as one value per band for the entire observing logs. Unless a value is input for the gain, the default is set to: 1.

There are two types of limiting magnitudes mag_{lim} available in the logs. There is the science image limiting magnitude which is associated to ZTF science images. It is estimated by computing the median magnitude of PSF-fit catalog sources falling within a narrow range of signal-to-noise ratio (SNR) centered on a value of 5. And there is the difference image limiting magnitude associated to the ZTF difference images (more in Section 3.2.3), is computed with an analytic formula.

We must emphasise that simsurvey do not account for limiting magnitudes but a related quantity, the sky noise, computed as:

$$\text{skynoise} = \frac{10^{0.4\times(ZP-mag_{lim})}}{5}, \tag{7.1}$$

with ZP standing for the Zero Point of the observation. It implies that we need the ZP values to compute the sky noise from $maglim$. We could use the default value $ZP = 30$ input in simsurvey. A more accurate value to use would be the ZP median measured values per band, provided in the *ZTF pipeline deliverable*. However, we aim to simulate the most realistic sample, with all our knowledge about ZTF observations and SNeIa. Therefore, it is crucial to use the measured ZP of each observation (see Chapter 4) as input to simsurvey and to compute the sky noise, also input in simsurvey. The ZP of the observations are not included in the observing logs file we have. We needed to collect the ZP for every observation available in the observing logs for the entire ZTF phase-I. We used python software from (Rigault 2018) to access to IPAC databases, gathered from there the ZP that we matched to our observing logs. We also gathered the gain of the observations.

Using the measured ZP and the limiting magnitudes, from both the science and difference images, we computed the associated sky noise to both types of limiting magnitudes for all the observing logs.

7.1.3 Simsurvey

Simsurvey (Feindt et al. 2019) is a survey simulation software, written in Python. It generates transient light-curves based on a telescope, ZTF in our study, true observing strategy and a transient model, both described respectively in Section 7.1.2 and 7.1.1. It simulates fluxes using sncosmo python package[1] and adds random but correlated flux scatter along

---

[1] `https://sncosmo.readthedocs.io/en/stable/`

the light-curves. The SNeIa flux errors have two components, for one observation :

$$\sigma_i^{SN} = \sqrt{\text{skynoise}_{obs,i}^2 + \frac{|f|_i^{SN}}{\text{gain}}}, \tag{7.2}$$

where skynoise$_{obs,i}$ is the sky noise of the i^{th} observation that we compute using Equation (7.1) (more details in Section 7.1.2), f is the simulated flux of the SN and the gain of the instrument (more details in Section 7.2.2). Other sources of uncertainties can be added like calibration errors, we will discuss it further in Section 7.2.2.

The output of the simulation is a light-curve for each SNIa detected. A SNIa is detected if it has a minimum number of points with a signal-to-noise ratio $SNR = |f|_i^{SN}/\sigma_i^{SN} \geq 5$, otherwise no light-curve is generated. This minimal number of points is set to a default value of 2.

7.2 Individual objects

Simsurvey was designed and used to predict ZTF discoveries and observations. The work presented in this chapter is the first attempt to compare simsurvey outputs to real ZTF observations. This section is focused on the accuracy of the simulations from simsurvey in reproducing the ZTF DR2 individual objects. By taking into account the real-time observing conditions and cadence of ZTF from Section 7.1.2 and all our knowledge about the objects gathered from the sample, we compare the simulated light-curves to the DR2 ones. As presented before, they are two types of limiting magnitudes in the observing logs. We have to identify the most appropriate one to use, since this quantity is directly linked to the sky noise, which is involved in the flux errors estimation (see Section 7.1.3). As presented, there are two components input to simsurvey: observing logs and transient model. To test the observing logs, we take SNeIa whose transient model parameters are known and fix them in simsurvey to simulate light-curves. Comparing these simulated light-curves to the DR2 measured ones would indicate the accuracy of the observing logs information used.

7.2.1 Methodology

To simulate the DR2 sample, we use the observed properties of the sample, *i.e.* the parameters of their light-curves, as inputs in simsurvey. Top left of Fig 7.1 represents the redshift distribution of the DR2 SNeIa, used in our simulations. The right top distribution and the bottom ones from the same figure (7.1) are the fitted SALT2 parameters (Guy et al. 2007) of all the DR2 objects, the final parameters will be in *Rigault et al. in prep.* For each DR2 object, we use its fitted SALT2 parameters (t_0, x_1 and c) and z as transient model in simsurvey along with multiple configurations of the ZTF observing logs and simulate it 10 times. In order to estimate our simulations, we compare the simulated and measured fluxes, their associated uncertainties along with their signal-to-noise ratio (SNR) at all epochs for each object of the DR2.

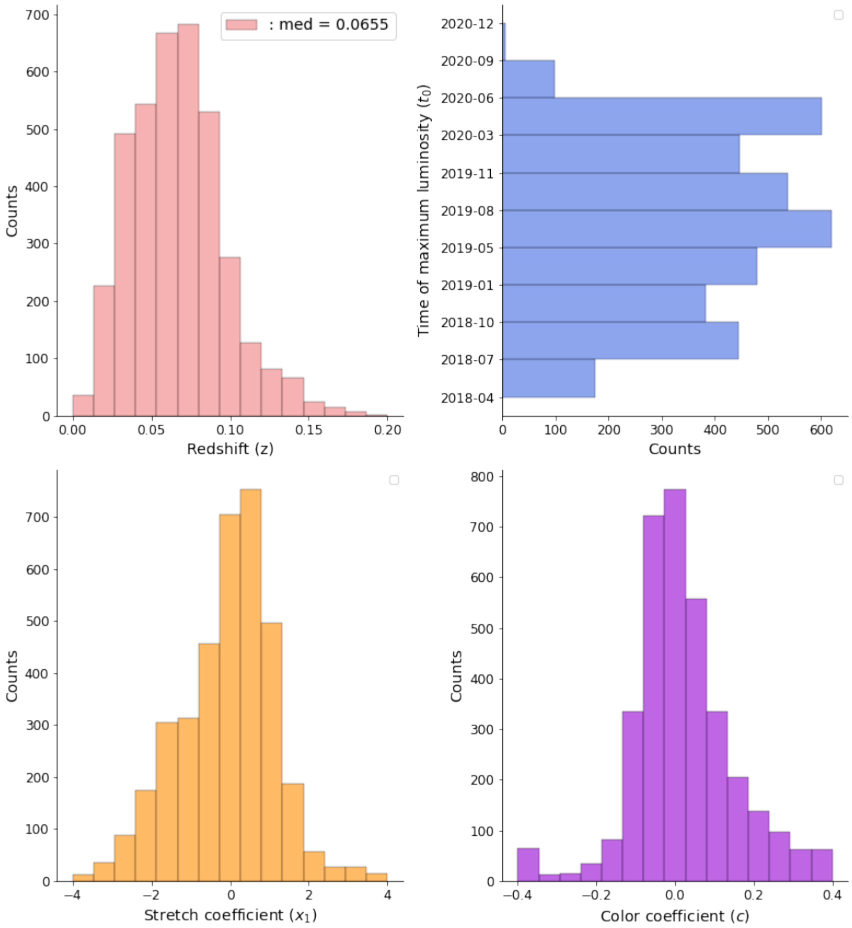

Figure 7.1: Distributions of the redshift and the SALT2 parameters fitted on the DR2 sample (final distribution in *(Rigault et al. in prep)*). ***Top left:*** redshift (z) distribution of the DR2 sample. *Top right* : time of maximum luminosity (t_0) fitted on DR2 light-curves. ***Bottom left:*** stretch (x_1) fitted values. *Bottom right* : SALT2 color (c) fitted values distribution.

7.2.2 Example case

We simulate each object from the DR2 10 times with simsurvey and compare the simulated light-curves to the DR2 observed light-curves. The first framework set for the simulations is based on sky noise computed from the limiting magnitudes of the difference images and the gain set to default value of one. The object is simulated 10 times. In Fig 7.2, we have an example of simulated light-curves with this setup compared to the ZTF DR2 light-curves of this same object, in $ztfg$ and $ztfr$ bands, along with the fluxes ratio. We can see that there is a good agreement between the simulated fluxes and the DR2 ones in both ZTF bands.

Bottom of the same figure (Fig 7.2) shows the ratio of the simulated and measured fluxes, associated to the light-curves at the top. We can notice that all the data points are around one and very little scattered, except at very early and late epochs which corresponds to when the SNIa were the faintest with high contribution from sky noise. In Fig 7.3, we represent the SNR of the simulated and measured light-curves from Fig 7.2 at top and their ratios, for both ZTF bands, at bottom. We can see that some data points at low SNR match, especially in *ztfr*. However, overall the SNR are in strong disagreement, with higher SNR values in the DR2 light-curves than the simulated ones. It suggests that with our simulations configuration, the simulated flux uncertainties are over-estimated and higher than the measured ones. It is unusual, in general, the simulations are more optimistic than the measured quantities, *i.e* they do not account for all uncertainty sources, even when they tend to be realistic. We must investigate our simulations framework for uncertainties estimation. From Equation (7.2), we know that there are two contributions to the simulated flux uncertainties: sky noise and gain. We will explore both options in Section 7.2.2.

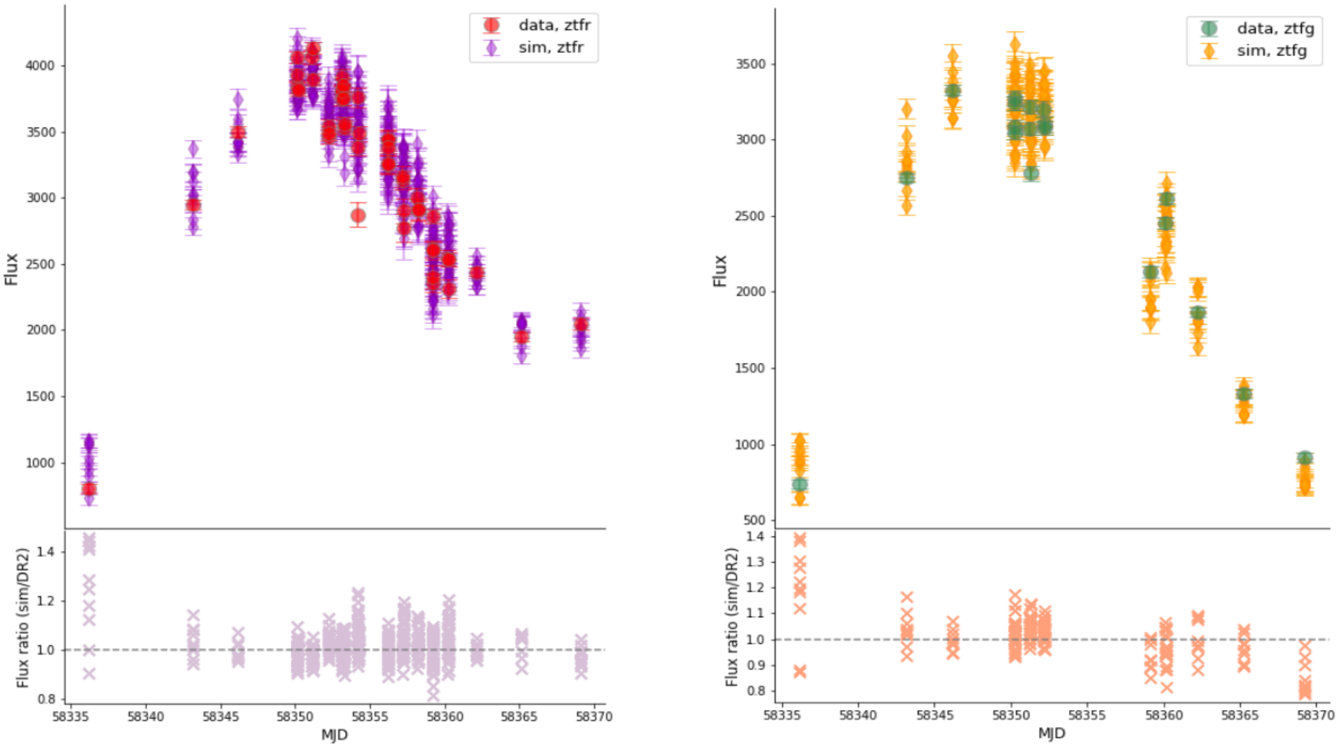

Figure 7.2: Example of ZTF18ablqlzp ($z = 0.0413$) simulated and measured light-curves with their associated fluxes ratio. The simulations are generated with a framework setting the default gain value ($gain = 1$) and limiting magnitudes from the difference images. The simulated and measured light-curves, in *ztfr* (at the left) *ztfg* (at the right) bands, are in good agreement at all epochs.

Improving the simulations

Gain issues

As the gain is set to one in simsurvey, we need the true gain value of ZTF observations and obtained it using metadata observations via ztfquery. Overall, the gain of the observations is found to be at $6.2e^{-}$/ADU, as specified by CCD performances (Dekany et al. 2020b), and thus we set the gain to this value in simsurvey and simulate the DR2 objects again.

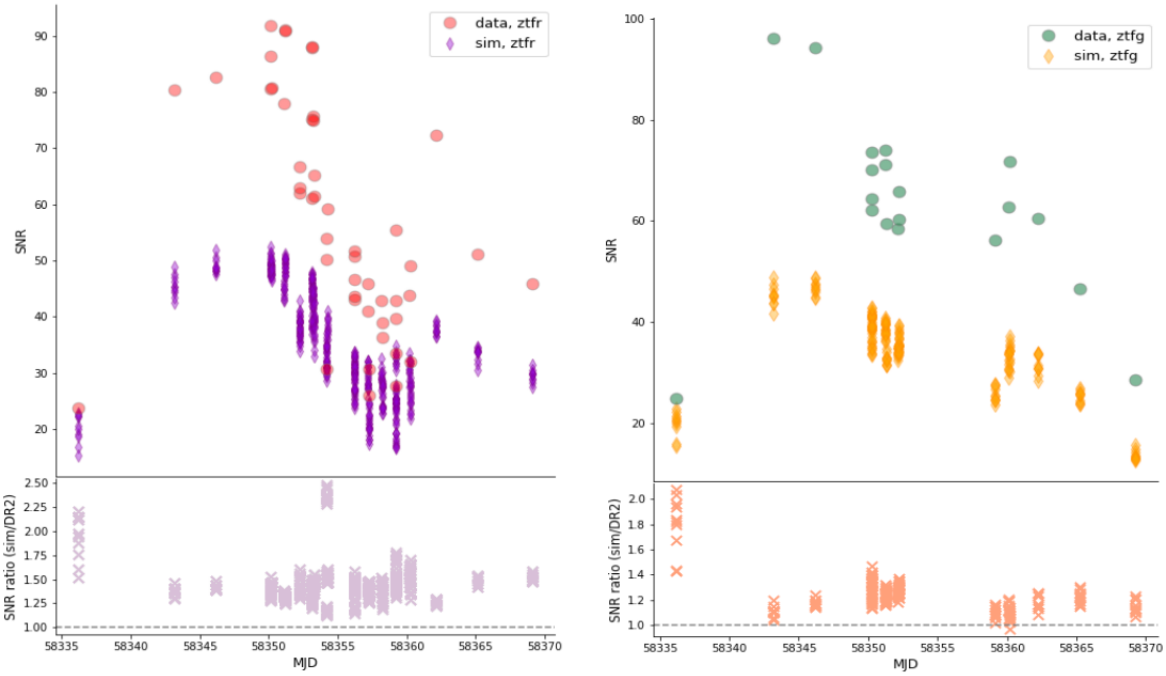

Figure 7.3: Example of ZTF18ablqlzp ($z = 0.0413$) SNR comparison of the top light-curves in function of time, in *ztfr* (at the left) and *ztfg* (at the right). The SNR do not match, with higher values in the DR2 light-curves.

Fig 7.4 shows the SNR computed for the simulated light-curves with updated value of gain and the DR2 associated light-curves in both ZTF bands. We can see that the SNR from the simulations are getting closer to the DR2 ones, especially when compared to Fig 7.3. It indicates that the simulated flux uncertainties are more consistent with the DR2 flux uncertainties. Nonetheless, there is still a disagreement between the SNR, it suggests that the simulated uncertainties of the fluxes remain overestimated. The second component to the simulated flux uncertainties is the sky noise, obtained from the limiting magnitudes and this is what we present in the following paragraph.

Impact of limiting magnitudes on flux uncertainties

There are multiple limiting magnitudes that we could use to compute the sky noise of the observations (see Section 7.1.2). Fig 7.3 and 7.4 are simulation results using sky noise from the difference images with different gain configurations. In Fig 7.5, we have represented the distribution of the limiting magnitude from difference and science images, we can see that the difference image limiting magnitudes display shallower values than the science image ones.

It implies that when the sky noise of the observations are computed with difference images limiting magnitudes, the values are higher than when computed with the science limiting magnitudes. Therefore, the simulated flux uncertainties get bigger, with the difference image limiting magnitudes, according to Equation (7.2), they are overestimated and hence the SNR of the simulations get smaller. In consequence, using smaller values of sky noise to simulate ZTF DR2 SNeIa would make the flux uncertainties smaller and closer to match the

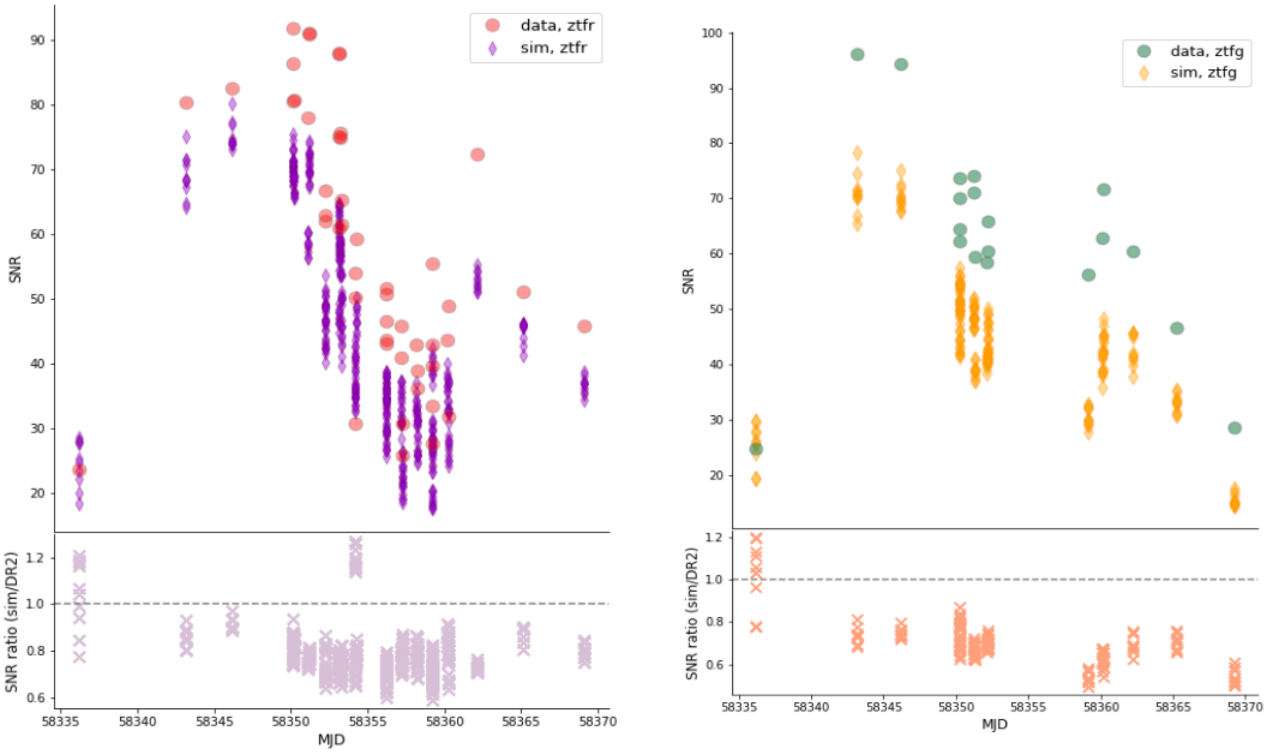

Figure 7.4: SNR of the simulated and measured light-curves of ZTF18ablqlzp ($z = 0.0413$) and their ratios, in the left in *ztfr* band and *ztfg* band in the right. The simulations gain is set to ZTF value 6.2 and the skynoise is computed using difference image limiting magnitudes. The simulations and DR2 SNR are getting closer, especially compared to bottom of Fig 7.2.

data flux uncertainties.

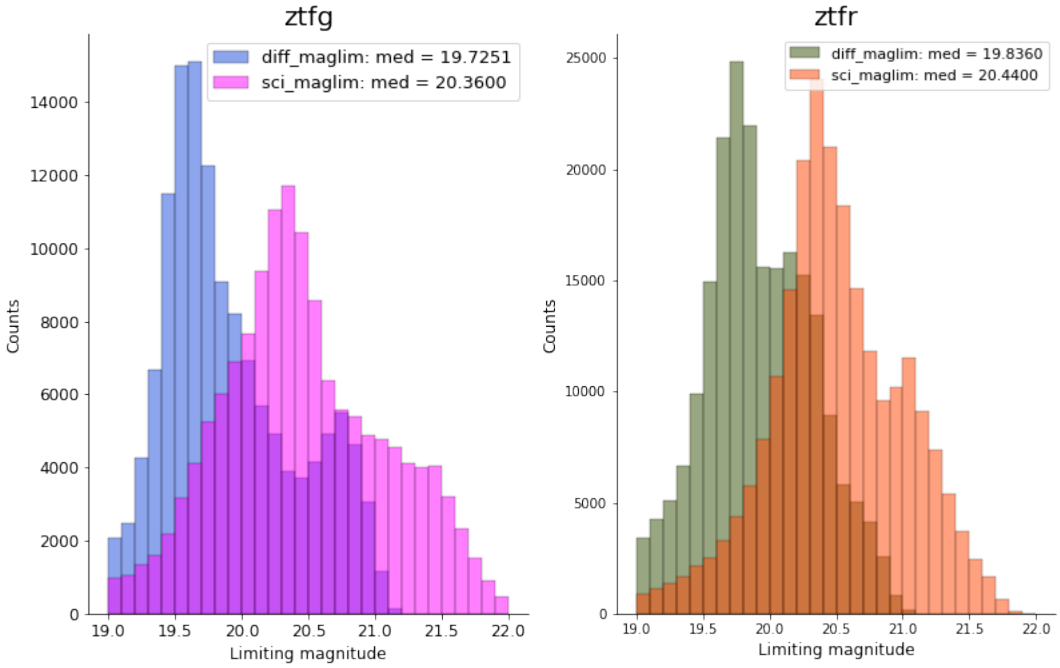

Figure 7.5: Distributions of limiting magnitudes, in *ztfg* (left) and *ztfr* (right) bands, from science and difference images for all the focal plan of the camera for July, 2018.

Using the science limiting magnitudes, we compute the associated sky noise to our observing logs and simulate the same object ZTF18ablqlzp. Fig 7.6 with gain set to simsurvey default value (which is one) and 7.7 with gain set to 6.2 represent the SNR of the simulated light-curves and from DR2 with the associated ratios. For the latter, the SNR of the simulations are higher than the DR2 ones, the difference is bigger for *ztfr*.

We test the latest configuration for the whole DR2 sample, gain set to 6.2 and sky noise computed from the science image limiting magnitudes, since it provides the most realistic outputs.

Calibration errors

Calibration uncertainties are accounted for in simsurvey as follows :

$$\sigma_i^{SN} = \sqrt{\text{skynoise}_{obs,i}^2 + \frac{|f|_i^{SN}}{\text{gain}} + (f_i^{SN} \times \sigma_{calib})^2}, \tag{7.3}$$

where the first two terms are from Equation (7.2) and σ_{calib} is the flux precision level deduced from the photometric calibration (Chapter 4).

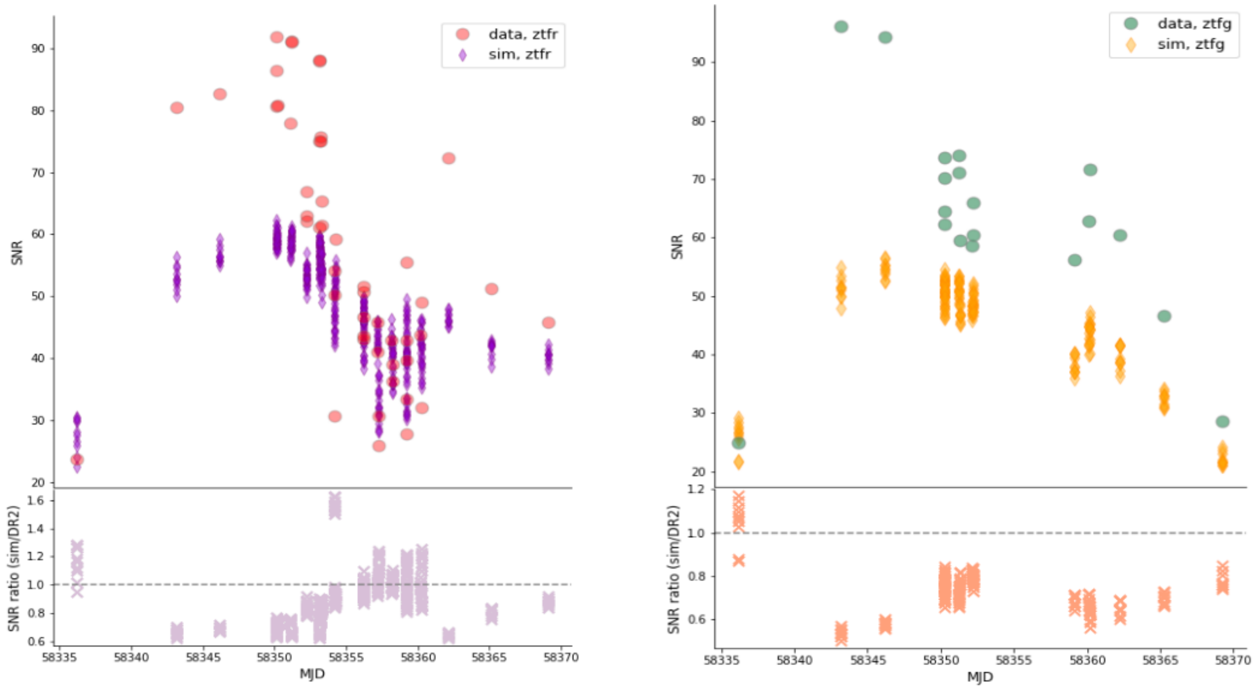

Figure 7.6: Example of ZTF18ablqlzp ($z = 0.0413$) SNR of the measured and simulated lightcurves, with gain $= 1$ and sky noise computed from science images limiting magnitudes in both *ztfr* (left) and *ztfg* (right) bands.

7.2.3 Simulating all DR2 objects

We simulate the whole DR2 sample, which makes 3613 SNeIa, following Section 7.2.1, with their SALT2 parameters, in Fig. 7.1, as ground truth. We compare the simulated fluxes along with the uncertainties to the DR2 ones. We perform our simulations using observing logs with skynoise computed from science image limiting magnitudes. We compare the fluxes, flux uncertainties and SNR between each observed and simulated data points of every DR2 SNIa.

Science image limiting magnitudes

Fluxes comparison
We simulate each SNeIa from the ZTF DR2 sample with our observing logs, skynoise is obtained from limiting magnitudes of the science images along with a gain set to 6.2. The simulated and measured fluxes and their ratios distributions are represented in Fig 7.8. The top plots represent the simulated flux of the DR2 SNeIa as a function of their measured ones, in both ZTF bands. The color of the points correspond to their associated redshift. The data points are scattered around the black solid line, it shows a good agreement between the simulated and measured quantities. Nonetheless, we can notice some data points display higher measured flux values than the simulated ones, with an accumula-

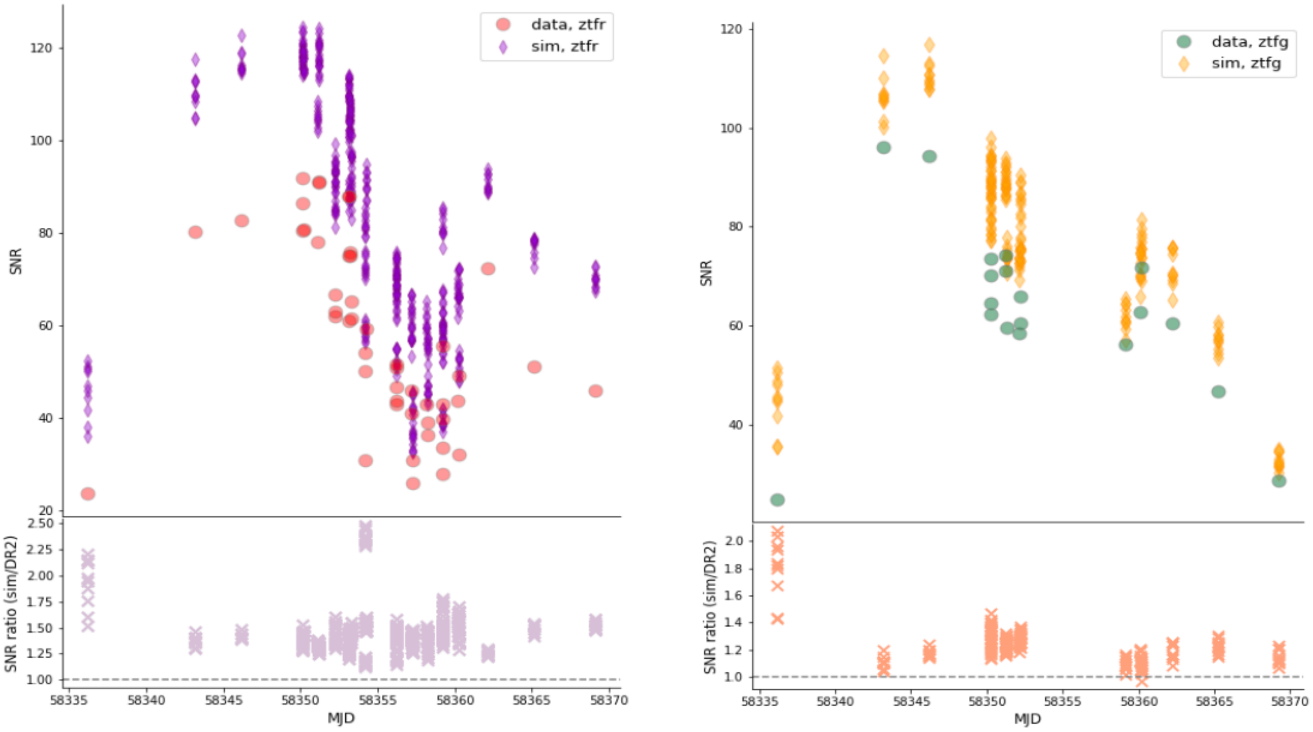

Figure 7.7: Example of ZTF18ablqlzp ($z = 0.0413$) SNR from the DR2 and our simulated light-curves with gain $= 6.2$ and sky noise computed from science images limiting magnitudes and their associated ratios in both *ztfr* (left) and *ztfg* (right) bands.

tion of points with simulated fluxes close to zero. We investigate the case of these data points in Section 7.2.4. In the same Figure (Fig 7.8), we have represented the distributions of the ratio of the simulated and measured fluxes for different ranges of data fluxes. For the first flux range ($flux_{data} < 5000$), in both bands, the fluxes ratio distributions are centred near one, evidence of matching fluxes. They are, however, asymmetric which shows that the simulated fluxes are under-estimated for some data points. For the second flux range ($5000 < flux_{data} < 10000$), we observe narrower and more symmetric distributions. For the last flux range ($flux_{data} > 10000$), we can see the distribution peaks around zero, showing a strong disagreement between our simulated fluxes and the DR2 measured ones.

Flux uncertainties comparison

We compare the simulated flux uncertainties (associated to the SNeIa fluxes discussed in 7.2.3) to the measured flux uncertainties, results are shown at top of Fig 7.9 in both ZTF bands. We can notice that the data points are strongly scattered around the solid black line, with several of them displaying higher measured flux uncertainties. To understand the origin of this scattering, we have represented the distribution of the ratio of the simulated flux uncertainties and the measured ones for three flux ranges. The first fluxes range ($flux_{data} < 5000$) gathers most of the data points and we can notice that their distributions (in *ztfg* and *ztfr* bands) are centred on ~ 0.85. It shows that our simulated flux errors are under-estimated. The distribution of the flux uncertainties ratio for the second fluxes range ($5000 < flux_{data} < 10000$), in both ZTF bands, shows centred distribution around ~ 1 with some asymmetries displaying outliers. For the ratio distributions of the last fluxes range, we observe a peak of the ratio distribution at ~ 0 showing a complete disagreement between the simulated flux uncertainties and the measured ones for the highest measured fluxes and hence the brightest points. With our simulations framework, the simulated flux uncertainties are smaller than the measured ones. It could indicate that other sources of uncertainties are missing in our framework. To support this hypothesis, we need to compare the SNR from our simulated data points to their associated DR2 measurements.

SNR comparison

The simulated and measured fluxes match, as shown in 7.2.3. However, the comparison of the flux uncertainties showed a strong disagreement (see 7.2.3). To ensure the accuracy of our simulation in replicating the data, we need to compare the SNR values. To this end, we compute the SNR for all the simulated and measured light-curves at all epochs.

Fig 7.10 shows the results of this comparison. Top figure is the SNR of the simulated data points in function of the DR2 measured SNR, in both ZTF bands. At low SNR values, the data points are well distributed around the solid black line, overall it indicates a great match between the SNR of the simulations and the DR2 sample. However, we can notice more data points scattered above the solid line, revealing higher SNR values in the simulations than in the DR2 sample; along with few data points standing further below the black solid line. At higher SNR values, we can see that the slope of the scatter of the data points changes and the data points take off from the solid line. It clearly shows higher values of SNR in the DR2 sample than in the simulations. This effect is more noticeable in a binned version of this scatter plot, shown in Fig 7.11. To build the binned data points, we compute the median values of SNR from the data for several magnitude ranges. We then compute the

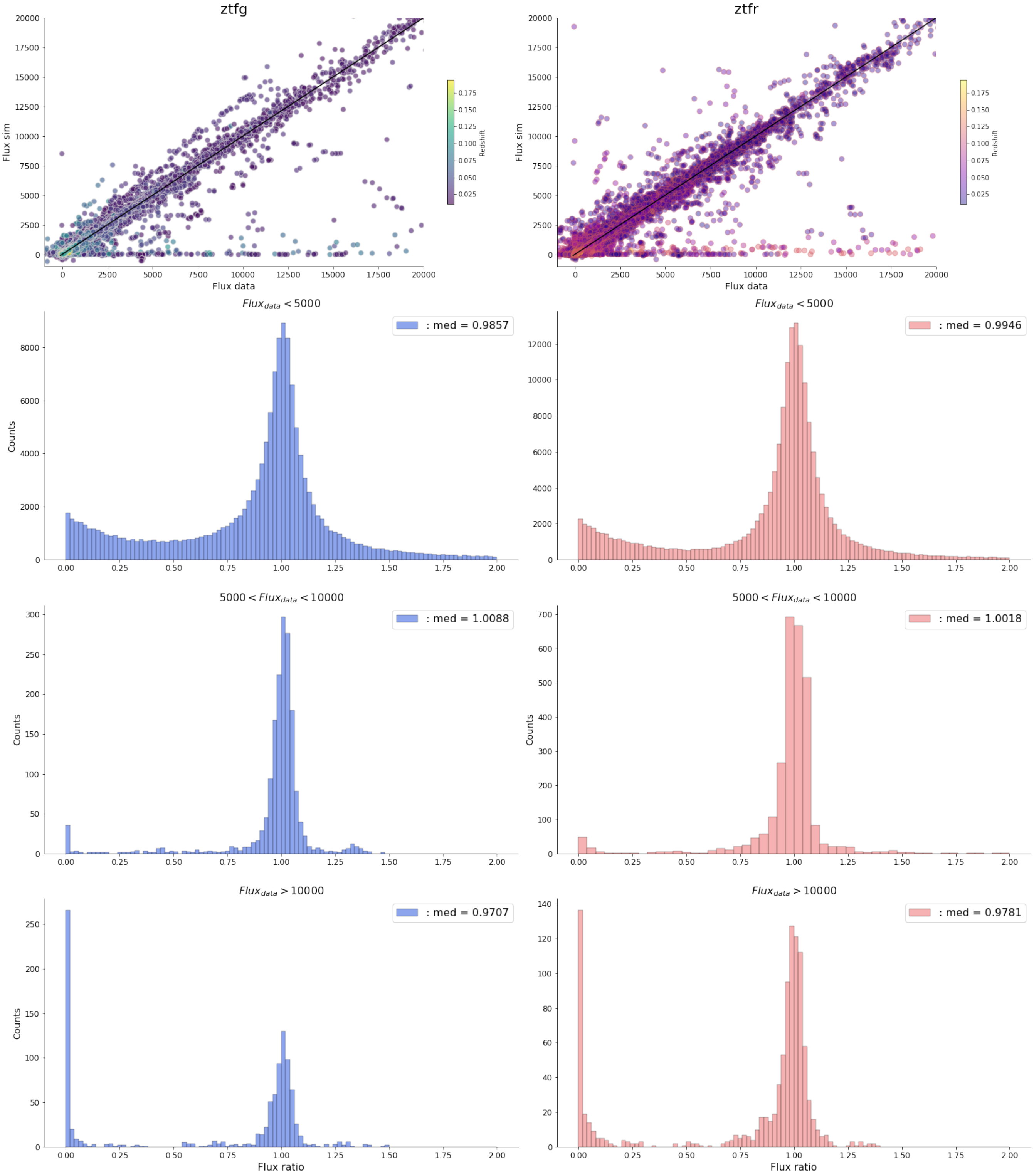

Figure 7.8: ***Top:*** all DR2 SNeIa simulated fluxes in function of the ZTF measured fluxes in *ztfg* (left) and in *ztfr* (right) bands. The colors in each correspond to the objects redshift. ***Bottom:*** the histograms represent the distributions of the ratio of simulated fluxes and the measured ones, for three ranges of data flux values.

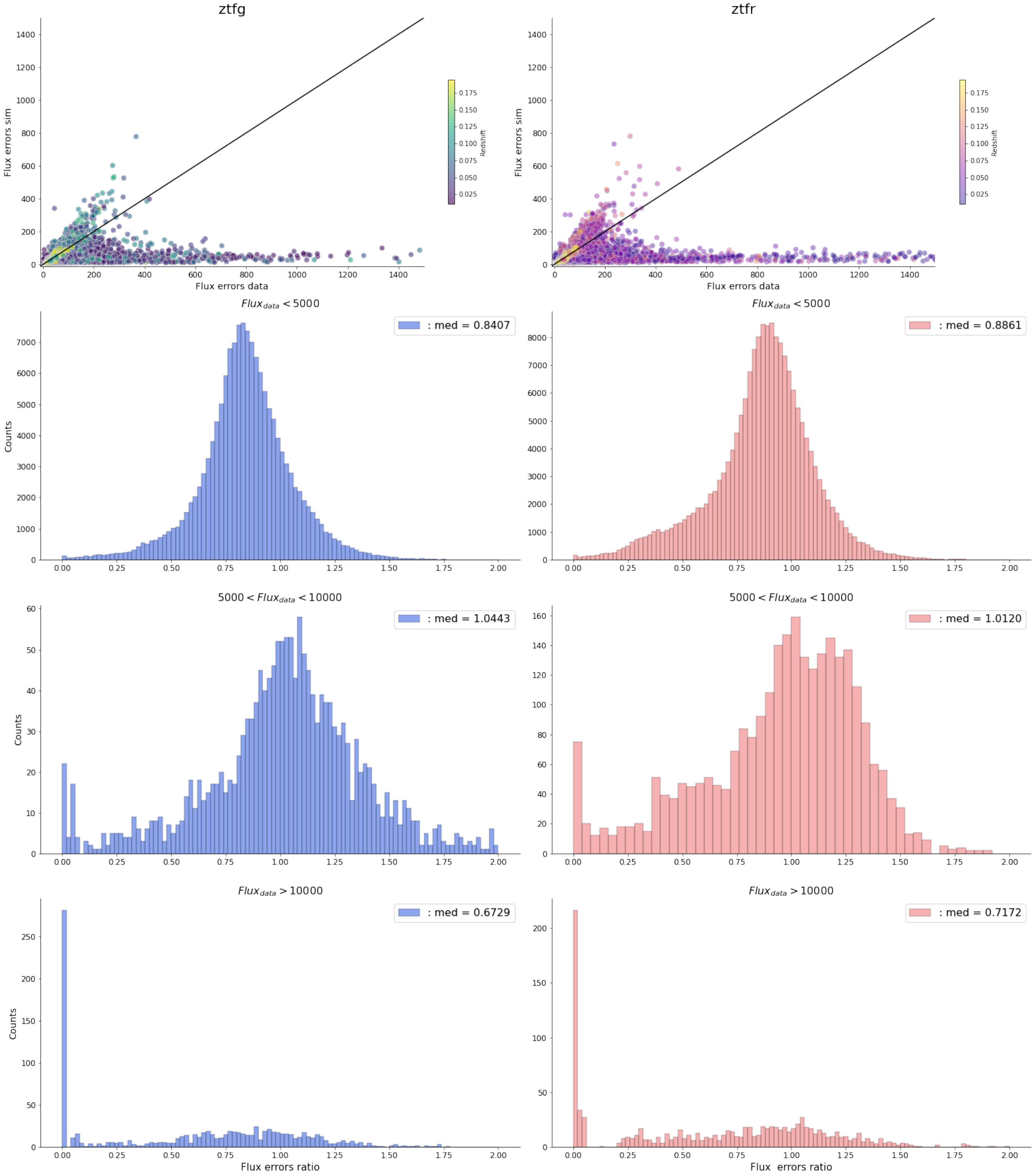

Figure 7.9: ***Top:*** simulated SNeIa flux uncertainties compared in function of the ZTF measured ones, in *ztfg* (left) and *ztfr* (right) bands. ***Bottom:*** the histograms represent the ratios of simulated and measured flux uncertainties for three flux ranges.

median value of the SNR in the associated magnitudes range in the simulations. In the same figure, we can see that the simulated SNR match the measured ones until SNR < 100. After this value, the SNR is higher in the data. The distributions of the SNR ratios are shown in Fig 7.10, for three flux ranges. We notice that the distributions are off-centred on values greater than one for the last flux range and display asymmetries which correspond to higher SNR in the DR2 sample.

We combine the true observing strategy of ZTF and the measured properties of SNeIa in simsurvey. We are able to reproduce all ZTF SNeIa photometrically measured data points with a SNR < 100. For data points with higher SNR values, the measured flux uncertainties are higher than the simulated ones. In the following section, we aim to match the simulated and DR2 objects flux uncertainties at high SNR.

Science image limiting magnitudes with calibration errors

As extensively discussed in Chapter 4, flux calibration uncertainties are crucial in SNeIa distance measurements. It is key to account for this source of uncertainties to make our simulations the most realistic. Therefore, we have simulated the DR2 SNeIa and accounted for the 2% precision flux level, from (Masci et al. 2018), in simsurvey (see Section 7.2.2), along with skynoise computed from science images limiting magnitudes, gain value set to 6.2.

Fig 7.12 shows the SNR of the simulated objects with calibration uncertainties in function of the DR2 SNR for *ztfr* in the left and *ztfg* in the right. At low SNR (> 30), the data points are scattered around the solid line, with many of them standing above the solid black line, yet, the binned data points match the line, indicating a good agreement in SNR between the simulated and DR2 samples. At higher SNR (> 30), all the data points along with the binned ones are below the solid line and form a plateau. It shows a strong disagreement between the simulations and the data. To properly compare the SNR of our simulations to the DR2 sample, especially at high SNR, we need to account for the calibration uncertainties in the DR2 measurements.

Precision flux estimation for the DR2 sample

We aim to include the calibration uncertainties in the DR2 errors budget. From the photometric calibration performances discussed in Chapter 4, the calibration uncertainties based on calibrators magnitude dispersion is around $\sim 2\%$. We investigate a new estimation based on SNeIa light-curves. For that, we compared the fluxes of the entire DR2 light-curves, at all epochs, to a baseline generated fluxes. We generate the baseline fluxes with a function from *sncosmo*. It uses a transient model, set as SALT2 (Guy et al. 2007) for our study, and its associated parameters along with observing information : dates and ZP values. For each SNIa from our sample, we set its associated fitted SALT2 parameters, redshift and observing information. We also take into account the Milky Way dust extinction (more in Section **??**. Once the baseline fluxes generated, we compute the normalised residuals : $(f^{dr2} - f^{sncosmo})/f^{sncosmo}$, for the whole sample at all epochs. We then compute the median absolute deviation (nmad) of the residuals per magnitude bin. They are represented in

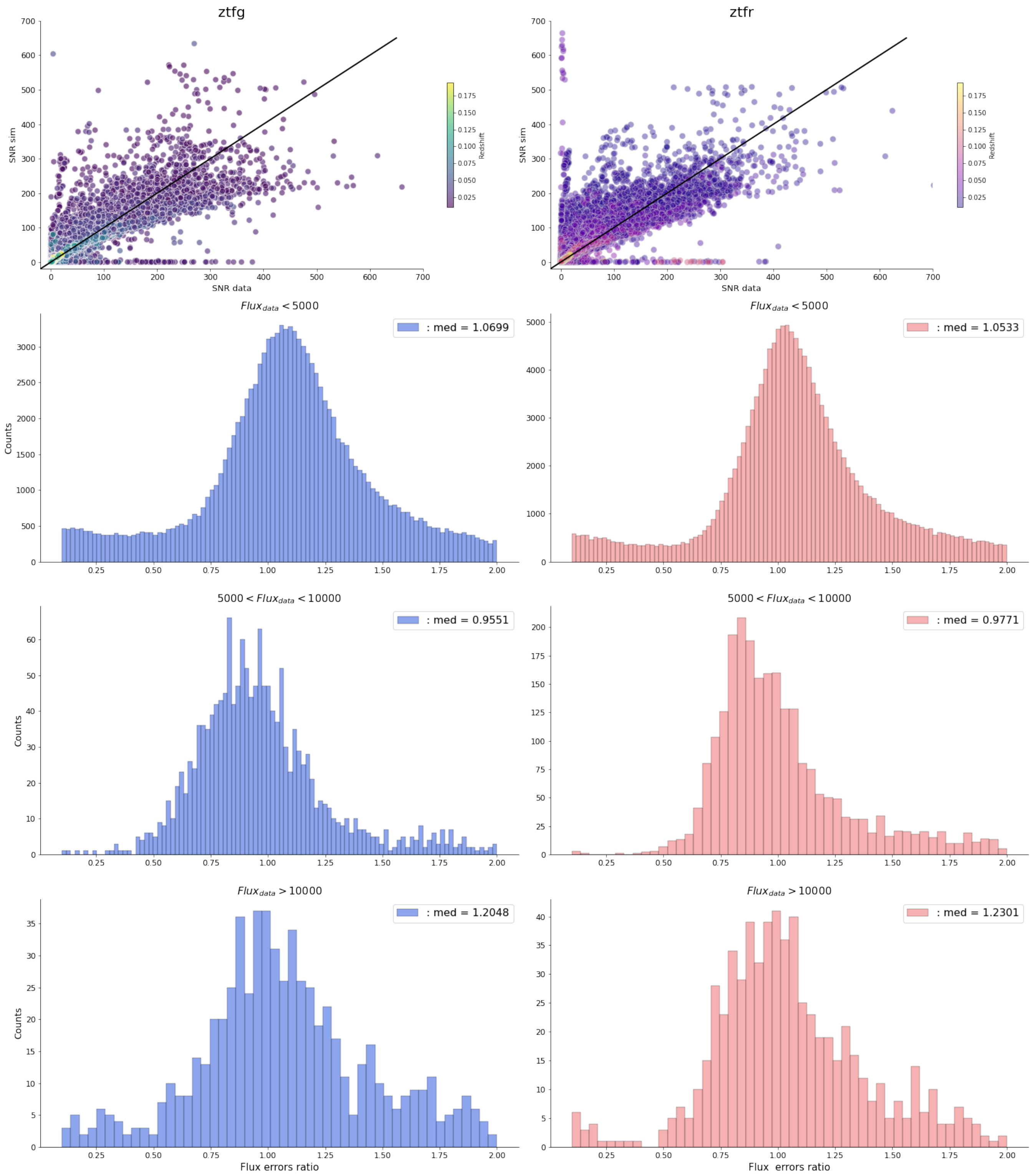

Figure 7.10: *Top:* SNR of the simulated SNeIa in function of their corresponding DR2 SNR, in *ztfg* at the left and *ztfr* at the right. The histograms represent the ratios of both SNR for three flux ranges.

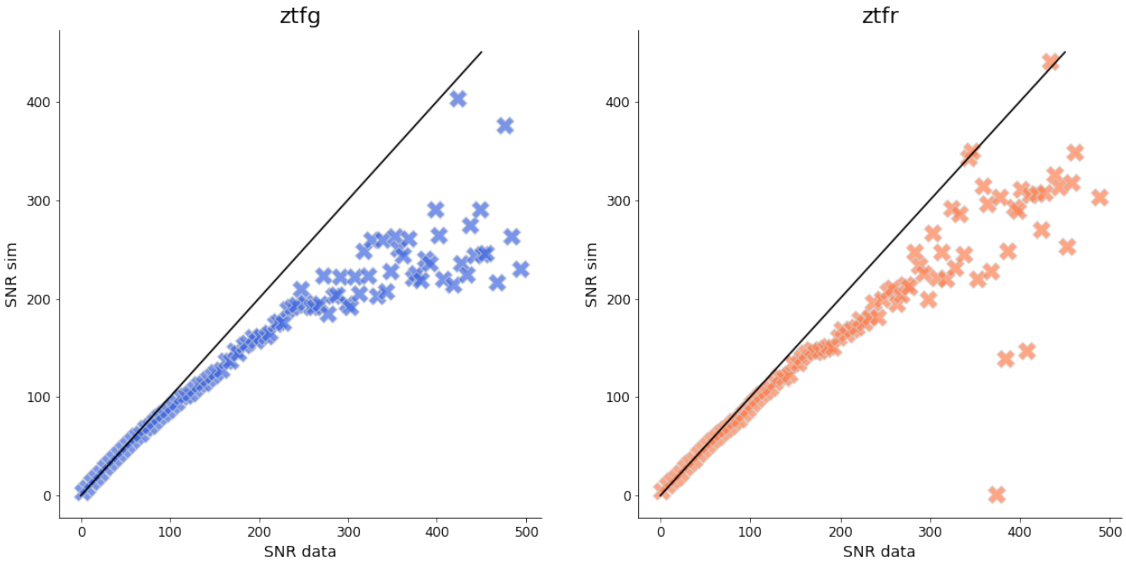

Figure 7.11: Binned SNR comparison between the simulations and the DR2 sample.

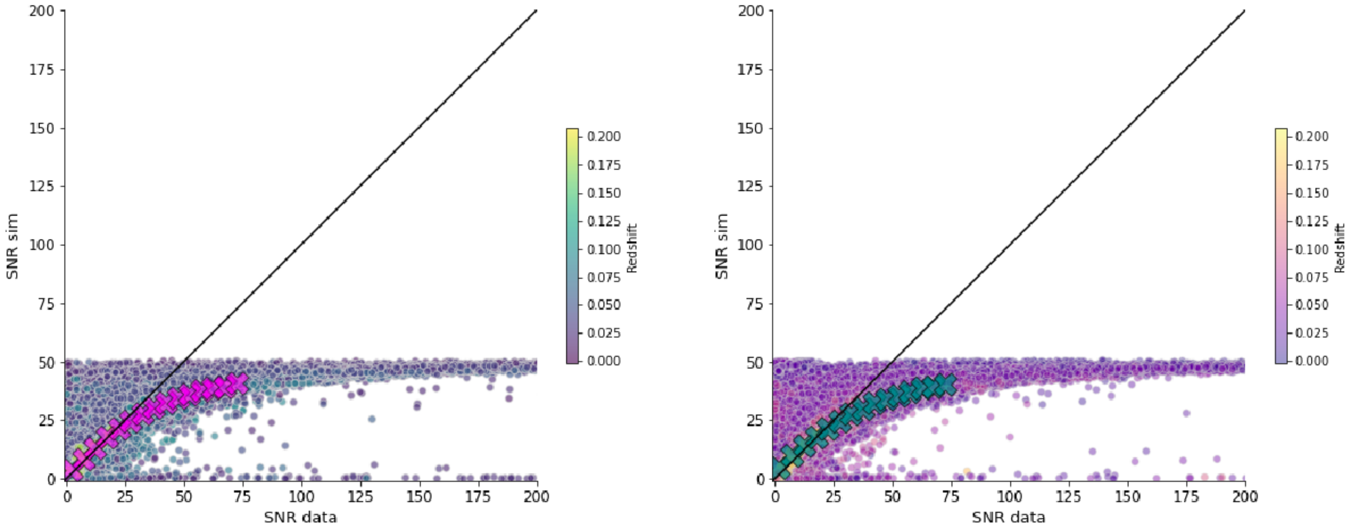

Figure 7.12: Binned and non-binned SNR of simulated light-curves in function of the SNR from the DR2 one.

Fig 7.13. The residuals get bigger with the magnitudes, as expected. From study we set the precision flux level in the DR2 to 3%.

Calibration errors in simulations and DR2

In regard of our investigations, we account quadratically for the 3% precision in the DR2 flux uncertainties, compute the new SNR of the DR2 sample and compare both quantities to the simulated ones, from 7.2.3, in Fig 7.14, along with their binned values in *ztfg* in the left and in*ztfr* in the right. It shows that the simulations are in good agreement with the

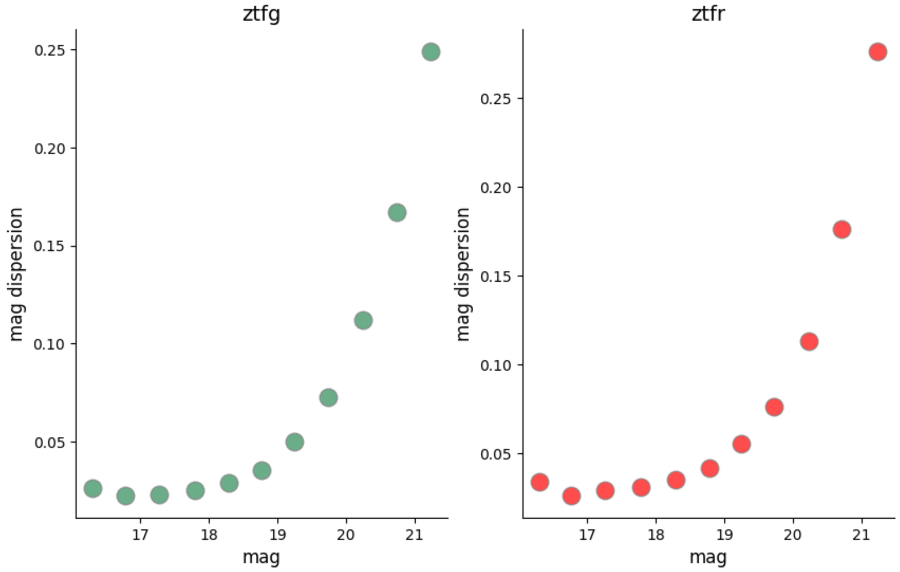

Figure 7.13: Normalised residuals of the DR2 fluxes binned in magnitude for *ztfg* and *ztfr* bands respectively in the left and right.

DR2 sample for low SNR values then the simulated SNR is overestimated. It indicates that the simulated errors remain under-estimated.

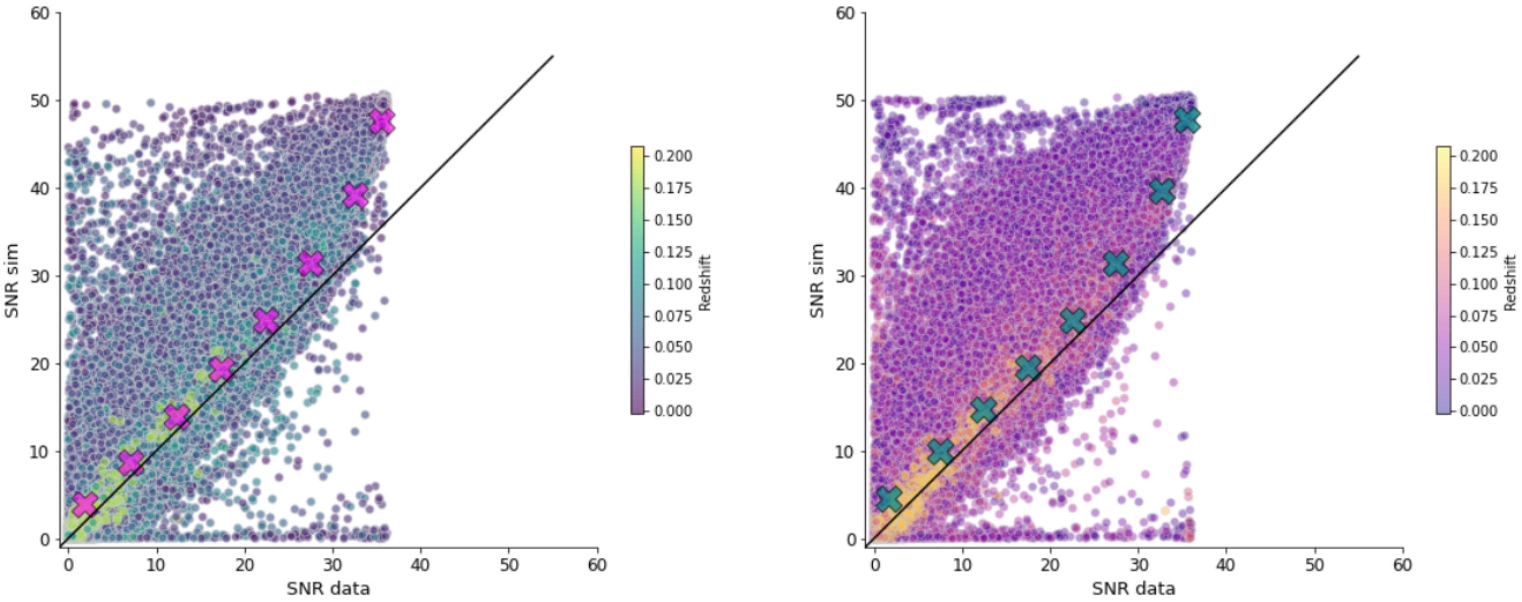

Figure 7.14: SNR of the simulated objects in function of the SNR from the DR2 sample left for *ztfg* band and right for *ztfr*, with calibration uncertainties.

The missing piece in the simulations

To make the SNR of the simulations and the DR2 measurements match we need an extra term to the simulated errors, in addition to the calibration errors. We found that adding an additional 2% flux level to the simulated light-curves make their SNR match with the DR2 ones, as shown in fig 7.15. The agreement between the simulated and measured quantities is clearly visible with the binned data points, in the same figure.

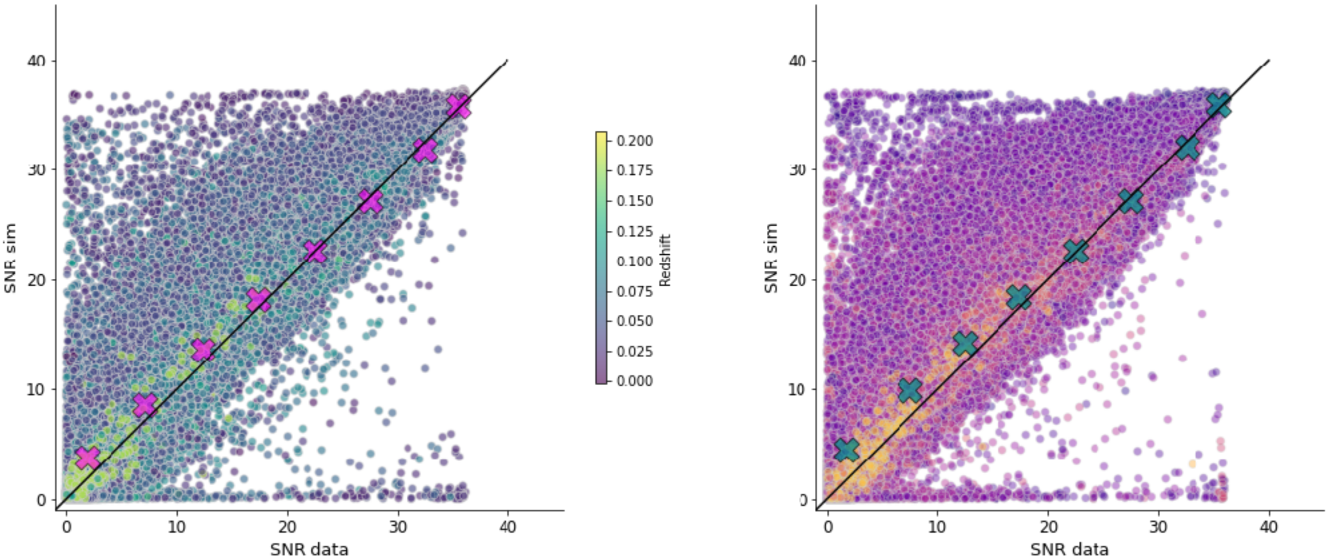

Figure 7.15: SNR of the simulated objects in function of the SNR from the DR2 sample with extra uncertainties in the simulations, in addition to calibration uncertainties in *ztfg* (left) and *ztfr* (right) bands.

7.2.4 Flux outlier data points

From the fluxes comparison, Fig 7.16 and Section 7.2.3, we can notice that some measured data points are incompatible with the simulated ones. We are interested in the data points with a very small simulated fluxes (~ 0) compared to the measured. They constitute a plateau, they are surrounded by black lozenges.
We investigate the behaviour of these data points to understand the origin of this issue and correct for it. We probe the limiting magnitudes of the difference images for the observations of the data points and report the distributions in Fig 7.17 (top plots), in *ztfg* in the left and in *ztfr* in the right. We can notice that the limiting magnitudes range around uncommon values, when compared to the distribution of ZTF limiting magnitudes shown in Fig 7.5. The limiting magnitude values range indicates a poor photometric quality night, which impacts the measured fluxes and their associated uncertainties. The bottom plots from the same figure (Fig 7.17) represent the phase distribution of our data points, in both ZTF bands. To computed the phase, we identify to which SNeIa belongs each data point in black lozenges (from Fig 7.16) and their observed time t_{obs}. We then use the fitted t_0 of the SNIa, time at maximum luminosity, to compute the phase of the data points : $phase = t_0 - t_{obs}$. We can notice that the distributions display peaks corresponding to early and late phases, namely, early and late LC data points.

To avoid flux outliers, a requirement on the observations quality should be established in the selection of the light-curves data points. The observations quality could be assessed with the limiting magnitude and the seeing. We must ensure that no bias is introduced when the selection is made.

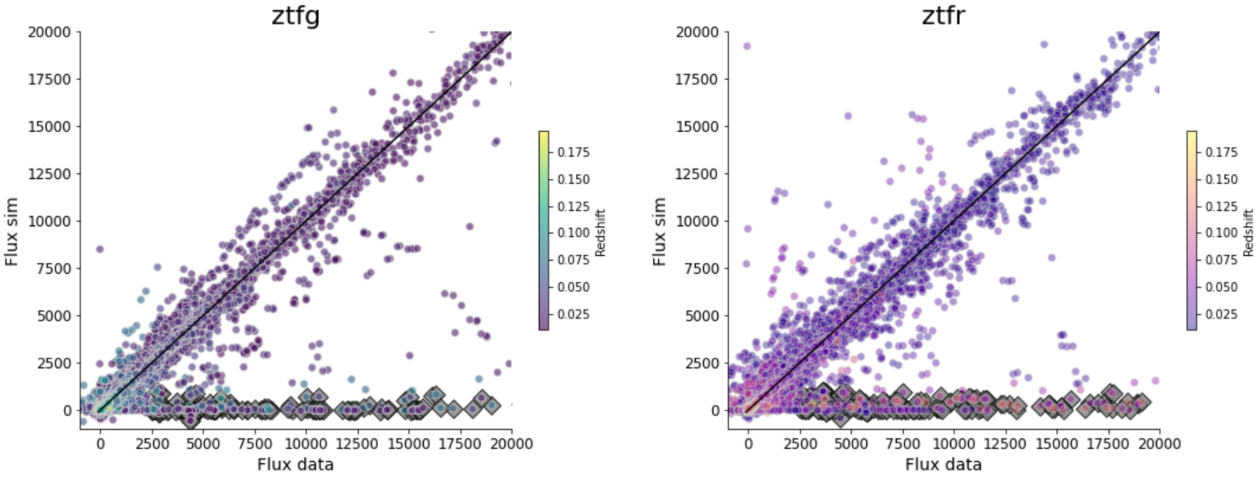

Figure 7.16: DR2 measured fluxes in function of the simulated ones in *ztfg* in the left and *ztfr* in the right. Flux outlier data points are surrounded in lozenges.

7.2.5 Summary

We aimed to simulate the most realistic DR2 sample, with all our knowledge of ZTF observations and SNeIa. We used the ZTF true observing strategy and state-of-the-art SNeIa template in simsurvey to replicate the whole DR2 sample. We simulated 3613 SNeIa and tested multiple configurations for the simulations framework. We replicated the DR2 fluxes, associated uncertainties and SNR using in our simulations the science limiting magnitude with gain $= 6.2$ and accounting for calibration uncertainties in both the DR2 sample and the simulations. We found that we need to account for 3% flux level in DR2 uncertainties and 2% in the simulations, in addition to the 2% calibration uncertainties in simsurvey.

7.3 Biases study

Now that the framework to reproduce DR2 objects is validated, we can use it to estimate biases in the distance measurements with ZTF. To this end, we simulate realistic SNeIa light-curves, fit them and compare their underlying $x_{1,in}$ and c_{in} distributions with the fitted values ($x_{1,out}$, c_{out}).

7.3.1 Sample simulation

We have simulated $20,000$ SNeIa with simsurvey, using the three years ZTF observing logs from Section 7.1.2 and SNeIa transient model from Section 7.1.1. We set a requirement of

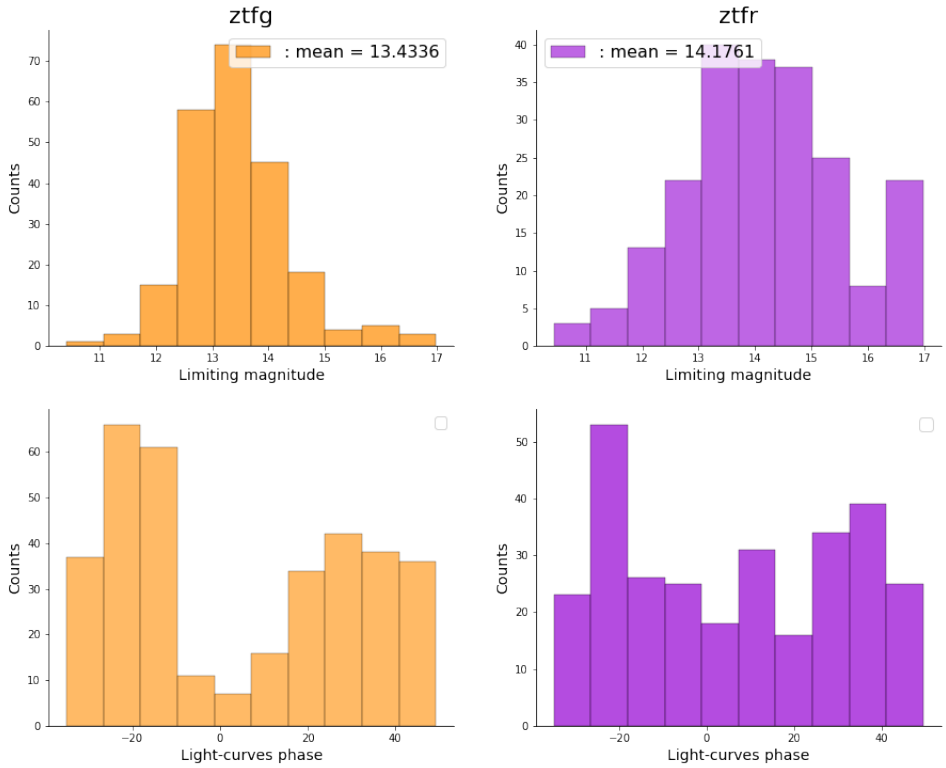

Figure 7.17: *Top:* distributions of the limiting magnitudes from the difference images where the incompatible data points were observed, in *ztfg* band (left) and in *ztfr* band. *Bottom:* incompatible data points phase distribution, in both ZTF bands.

four-point detections ($SNR > 5$) for an object to be part of our sample. Only $10,555$ SNeIa passed this requirement, they constitute our sample study. We fit the simulated light-curves with the SALT2 model (Guy et al. 2007).

7.3.2 SALT2 parameters comparison

For each object of our sample, we compare ($x_{1,out} - x_{1,out}$) and ($c_{out} - c_{in}$) per redshift range. Top of Fig 7.18 shows the results of x_1 comparison in the left and c comparison in the right, for the first redshift bin ($z < 0.05$). Both distributions are centered on zero and display some outliers, more visible in the scatter plots, bottom of Fig 7.18 ($x_{1,in}$ in function of ($x_{1,out} - x_{1,in}$), same for c). No bias is found in the x_1 comparison, the scatter of the difference is small (~ 0.6). For c comparison, we can notice a population of objects, sitting in the right of the associated scatter plot, also visible in the distribution above. This population of objects was not simulated as red but after the SALT2 fit, the objects are found red. We can check if the bias remains, after some quality cuts on the light-curves. The same comparison plots for the intermediate-z ($0.05 < z < 0.1$) and high-z ($z > 0.1$) are available in Appendix 7.5. We use the Bright Transient Survey (BTS) (see Section 3.1.3) requirement

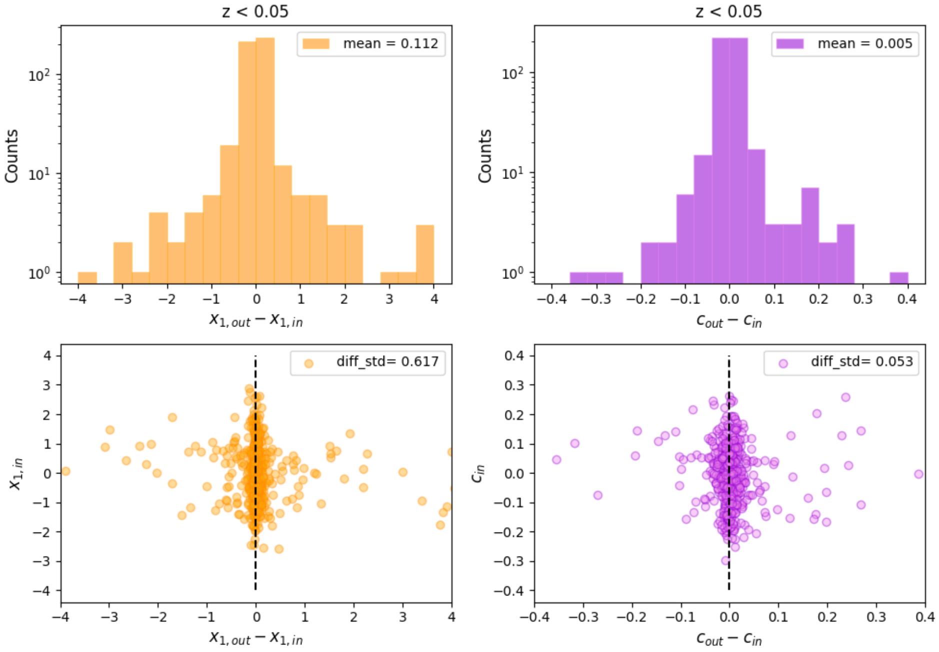

Figure 7.18: *Top:* difference distributions of x_1, in the left and c in the right. *Bottom:* $x_{1,in}$ in the left and c_{in} in the right in function of their differences for $z < 0.05$.

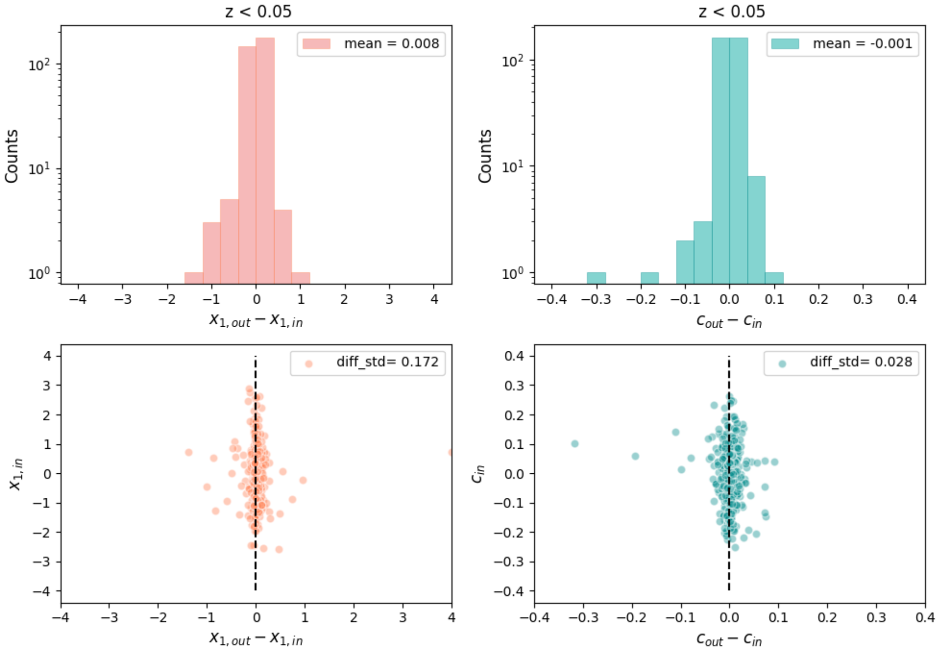

Figure 7.19: *Top:* after BTS cuts difference distributions of x_1, in the left and c in the right. *Bottom:* after BTS cuts$x_{1,in}$ in the left and c_{in} in the right in function of their differences for $z < 0.05$.

on the number of points in the light-curves per epochs and bands, the requirements are detailed in 7.4.2, on our simulated light-curves. We do the same comparison of x_1 and c for the light-curves after the BTS cuts. Fig 7.18 shows for low-z objects, in the left, $x_{1,out} - x_{1,in}$ distribution and scatter, in the right we show the same quantities for c. The dispersion of x_1 and c are reduced and the objects simulated non-red but fitted red noticed from right of Fig 7.18. The distributions and scatter plots after BTS cuts for intermediate and high redshift ranges are available in Appendix 7.5.

Fig 7.20 sum up all the the dispersion of $(x_{1,out} - x_{1,in})$ in the left and $(c_{out} - c_{in})$ in the right measured with and without BTS cuts binned in redshift. The mean redshift was taken per range. Overall, the dispersion increases with increasing redshifts and BTS cuts allow to reduce the dispersion for both x_1 and c for all redshift bins. Here are the details:

- low-z: the dispersion in x_1 is reduced from about ~ 0.61 without any cuts to ~ 0.17. For $(c_{out} - c_{in})$, the dispersion is reduced from ~ 0.05 to ~ 0.03.
- Intermediate-z: the dispersion is x_1 is ~ 0.7 and is reduced to ~ 0.4 with the applied cuts. The c dispersion goes from ~ 0.065 to ~ 0.045 after the BTS cuts.
- High-z: x_1 dispersion is reduced from ~ 0.8 to 0.6 with the application of BTS cuts. For the c dispersion it goes from > 0.07 to < 0.06.

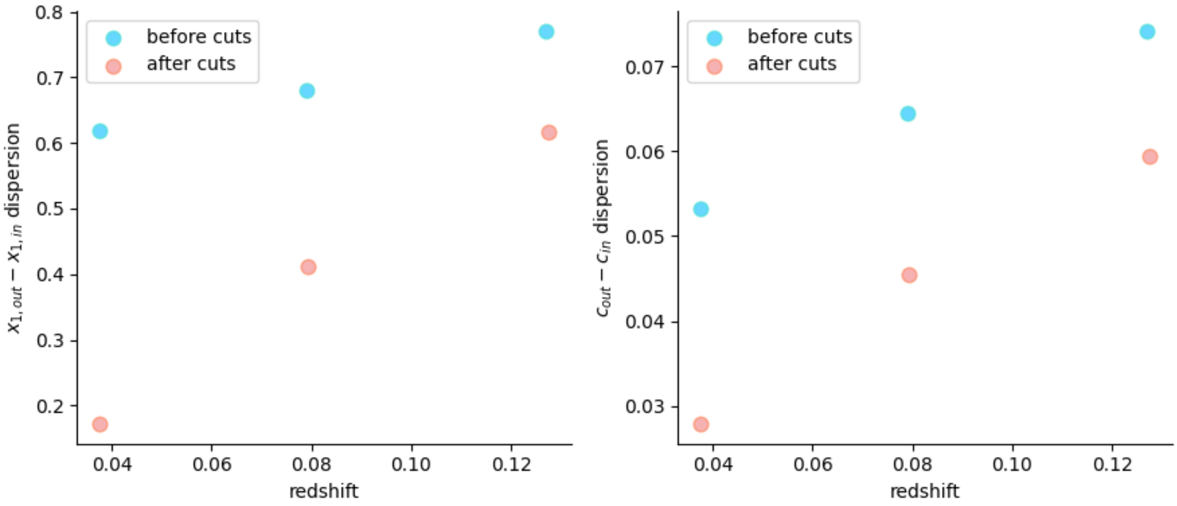

Figure 7.20: *Left:* binned dispersion of $x_{1,out} - x_{1,in}$ in function of the redshift, before and after quality cuts on the light-curves. *Right:* binned dispersion of $c_{out} - c_{in}$ in function of the redshift, before and after quality cuts on the light-curves.

7.3.3 Summary

We simulate $10,555$ SNeIa using simsurvey to which we have input the true observing strategy and realistic transient model. We fit the light-curves with SALT2 model and compute for the whole sample the difference between the fitted stretch $x_{1,out}$ and the input one to simulate the light-curves $x_{1,in}$. We compute the same difference for SAlT2 c. We applied BTS sampling light-curves requirements, the dispersion in the difference of the parameters is significantly reduced, no evidence of bias is found.

7.4 Replicating the DR2 sample

We have used simsurvey to simulate individual DR2 objects of known transient model to validate the observing logs. We also have used the simulations to study the biases, in the same way we use them is this section to assess ZTF DR2 sample selection. We must emphasise that simsurvey simulates all the objects that ZTF should have observed, given the observing logs input to simsurvey, without any selection. ZTF as a limited magnitude survey (see Section 3.1.2) finds objects photometrically up to a given limiting magnitude per band. However, it misses most of these objects because they are too faint to trigger the classification process, therefore they are not classified. This is what we call spectroscopic selection. The DR2 sample, described in 3.2, is made of only spectroscopically confirmed SNeIa, the sample is missing, preferentially, the faintest objects, the non-classified ones. Since no spectroscopic selection is implemented in simsurvey, we can simulate all the objects that ZTF has observed photometrically. It includes the non-classified and thus the missing ones. With the application of the spectroscopic selection function of the DR2 sample to the associated simulated sample, we could compare both samples and investigate the sample selection.

7.4.1 Simulations framework

For our simulations, we used the observing logs described in 7.1.2, DR2 transients location and realistic transient model. In Section 7.2, we have shown that the fluxes and associated uncertainties of the DR2 sample and the simulations match, if we take into account the calibration uncertainties in both samples. Based on that, we added 3% flux precision level to the measured flux uncertainties and accounted for this precision level in the simulations. The transient model parameters that we have input to simsurvey are shown in Fig 7.21. We set the minimum and maximum of the redshift of the simulations from the DR2 sample and represented the redshifts of all the simulated SNeIa in Fig 7.22 and the DR2 ones.

Number of SNeIa

As discussed in Section 5.1.4, the rate of SNeIa is imprecisely defined. To prevent any bias in the number of SNeIa we simulate, we tune the rate by matching data and simulation at low-z ($z \leq 0.04$), assuming that the number of SNeIa at low-z in DR2 is complete. However, at this redshift range, the DR2 sample is contaminated by non-regular SNeIa which are subluminous objects (SNeIa91bg). We can find in the literature Scolnic et al. 2018; Guy et al. 2010 criteria on sALT2 parameters to apply to the sample that should remove non-regular SNeIa: $|x_1| < -3$ and $|c| < 0.3$. These cosmological criteria were chosen because the

SALT2 model Guy et al. 2007 is only valid on these values. In the following comparison, we applied these cuts to the DR2 sample.

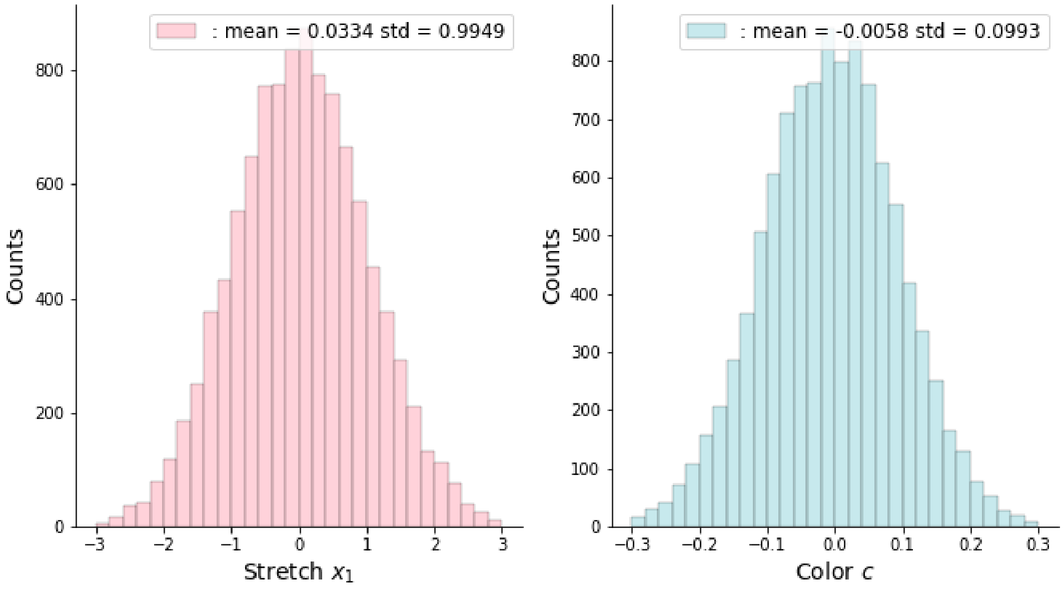

Figure 7.21: Distributions of SALT2 parameters, stretch (x_1) and color (c) used to simulate the DR2 sample.

Moreover, we set up for the simulations a requirement of four-points detection in whether *ztfg* or *ztfr*. We also require it for the DR2 sample.

Samples redshift comparison

The redshift distributions of the simulated and the DR2 objects passing this requirement are represented in Fig 7.23. We can see that at low-$z < 0.02$ the distributions match by construction, but at higher redshift many more objects are observed in the simulations than in the data. This is after considering photometric selection, the DR2 objects are what ZTF has observed, and the simulated distribution corresponds to what is expected to be detected by ZTF. However, as discussed in Section 3.2 DR2 sample is a spectroscopically selected one. All objects in the DR2 redshifts distribution are spectroscopically classified. With only the brightest objects being spectroscopically classified, as presented in Section 3.1.3, this introduces a second selection that needs to be accounted for in our simulations: spectroscopic efficiency function.

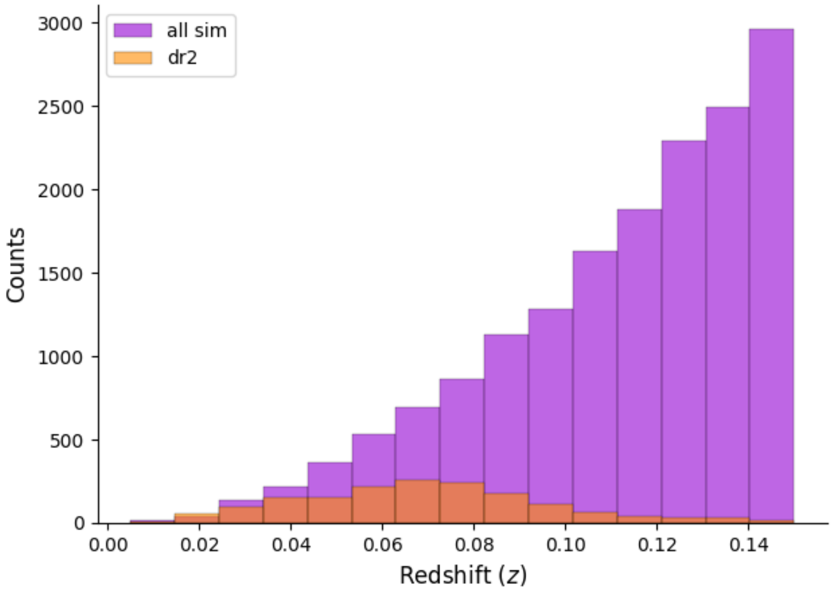

Figure 7.22: Redshift distributions of the simulated sample and the DR2 objects.

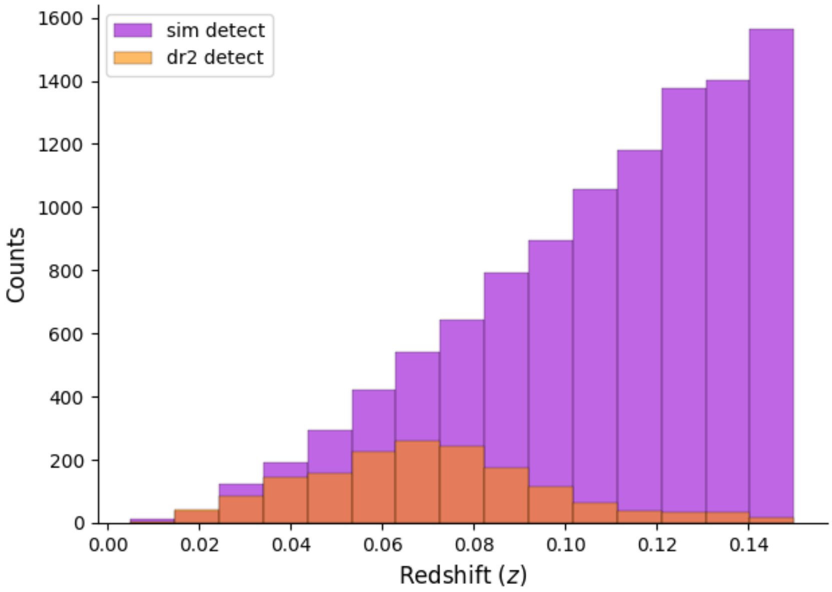

Figure 7.23: Redshift distributions of simulated sample and the DR2 objects passing the four-point detections requirement.

7.4.2 Simulating BTS

The spectroscopic efficiency assigns a probability to an object to be spectroscopically classified. The chances for any SNeIa to be sepctroscopically targeted and added to the final sample depend on a wide range of factors including telescope availability, weather conditions, transient brightness and human ability or machine-learning performance. This probability map can be parameterised and expressed in a functional form commonly known as a *spectroscopic selection function.*

As discussed in Section 3.1.3, the classifications of the DR2 SNeIa come from multiple surveys and instruments, each with different capabilities and priorities. Therefore, there is not only one selection function or parameter that describes the entire ZTF DR2 sample. Nonetheless, from *Rigault et al. (in prep)* we know that 80% of the objects of the DR2 sample were classified by the Bright Transient Survey (BTS) program (Fremling et al. 2019; Perley et al. 2020). This program is well-defined with a measured selection function. To test the accuracy of our simulations, we thus compare the BTS sample to our simulated one with the BTS selection applied.

Selection criteria for BTS

The BTS program classifies bright transients, discovered by the main survey program of ZTF (MSIP). Transients are selected for spectroscopic observations based on their peak brightness and light-curves sampling. The selection criteria are a set of quality requirements on the number of observations of the transient, the detailed list can be found in Perley et al. 2020. For our simulations, the following cuts are relevant and will be referred to as BTS cuts:

- one observation between 7.5 and 16.5 days prior to the time when the brightest detection in the transient light-curve was recorded.
- In addition to the detection at peak magnitude, the transient must have an observation either $2.5-7.5$ days before *or* $2.5-7.5$ days after the peak magnitude measurements.
- The transient must have an observation posterior to the peak magnitude time. There must be one observation at $7.5-16.5$ days after the peak magnitude observation time or alternatively an observation $2.5-7.5$ days after maximum and an observation between 16.5 and 28.5 days after maximum.

Classification probability

As discussed above, the BTS sample is photometrically selected from ZTF light-curves information. A full list of all objects passing the criteria is available online[2]. Spectroscopic follow-up for the sample is performed on SEDm (see Section 3.2.2 and Section 3.1.3) . The

---

[2] `http://sites.astro.caltech.edu/ztf/rcf/explorer.php`

survey aims to classify all transient brighter than 18.5 mag. With a simple selection criteria based on mostly transient brightness, the success rate of this survey can be parameterised through one parameter, the maximum observed brightness in any ZTF band. The efficiency of classifying a transient is defined as the number of classified transients divided by total number of transients in a bin of peak magnitude.

$$\epsilon_{mag} = \frac{N_{class}}{N_{total}}. \tag{7.4}$$

The BTS program is extremely stable over the lifetime of ZTF, therefore only one function is required to describe the BTS sample. This function, for the BTS program, was first calculated from 2018 data Perley et al. 2020 and has been recalculated to include all data from ZTF phase-I. The updated efficiency curve is represented on Fig 7.24. We can notice that for events with a peak brightness less than 18.5 mag, the classification efficiency is greater than 90%. For events with a peak brightness of 18.7, the classification efficiency is around 55% . At 19 mag, less than 40% of events are classified. BTS transients with peak brightness values $>$ 19 are not classified, their classification efficiency is zero.

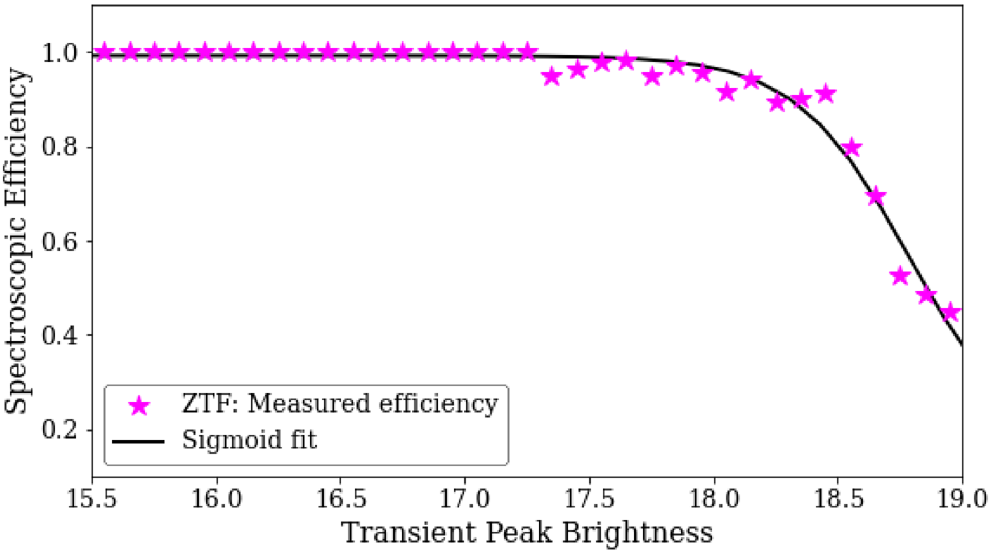

Figure 7.24: BTS spectroscopic efficiency in function of magnitude bins, the solid black line corresponds to a sigmoid fit. Th efficiency function was calculated from ZTF phase-I data and was obtained from *BTS working group*.

To include this efficiency in our simulation, for any event passing the BTS selection criteria (see Section 7.4.2), we calculate the peak observed magnitude from ZTF and determine the classification efficiency associated to the transient according to the magnitude bin of its peak brightness, Fig 7.24. We, then, draw a random number between zero and one from a uniform distribution. If the drawn value is less than the classification efficiency, the event is considered classified and added to the final sample. If the value is greater than the classification efficiency, the event is considered unclassified and is not included in the final sample.

7.4.3 Samples selection

To the simulated and DR2 objects, from Fig 7.23, that passed the four-points detection requirement, we apply the BTS spectroscopic selection function (see Section 7.4.2).

Application of BTS criteria

We apply BTS cuts, described in Section 7.4.2, to every simulated and DR2 object represented in Fig 7.23. The redshift distributions of the selected samples are represented in Fig 7.25. We can notice that the number of simulated objects drop down, SNeIa with bad sampled light-curves are removed. However, the distributions do not match yet. We need to use the spectroscopic efficiency function on this simulated sample that passed the BTS cuts.

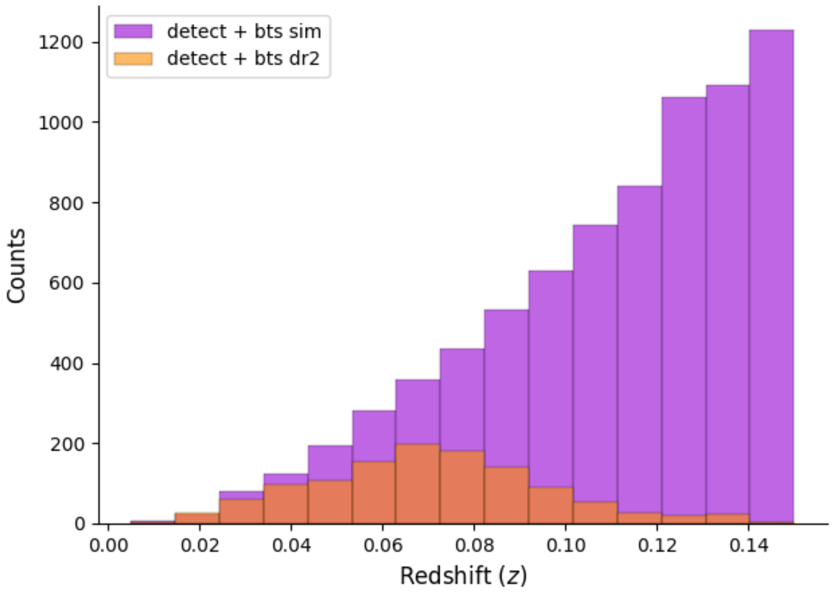

Figure 7.25: Redshift distributions of the simulated and DR2 objects that passed the BTS cuts (see 7.4.2).

Application of BTS efficency function

The last step in the implementation of BTS selection function on our simulations is to apply the BTS classification efficiency (see Section 7.4.2) to the simulated objects that passed the BTS cuts from Section 7.4.3. Fig 7.26 represents the redshift distribution of the simulated and selected sample, from Section 7.4.3 after the application of classification efficiency compared to the DR2 sample that passed the same BTS cuts from Section 7.4.3 and the cosmological ones from end of Section 7.4.1. Fig 7.27 shows the peak magnitude of the those objects in function of the redshift. We can see that both distributions display the same shape. We notice three cases, in the comparison, that we will develop per redshift range.

- **At low-z** ($0 < z < 0.04$): the distributions are not consistent with each other, the number of SNeIa in the DR2 sample is higher than in the simulations. Despite the cosmological cuts we applied on the DR2 sample (in 7.4.1), some SNeIa passed the cuts even though they are not well-defined by the SALT2 model, they are known as SNeIa91bg (see Section 3.2.1). They are faint and observed at low-z. We must emphasise that since the SNeIa simulations are based on SALT2 template, the simulated sample include only regular SNeIa. Therefore, the additional objects we notice in the DR2 distribution and not in the simulations would be this population of sub-luminous SNeIa. They are two possible approaches to match the distributions: identify the sub-luminous objects and remove them from the DR2 sample or include them in the simulations. The first approach is ideal, we would look at the every DR2 object (its spectra and light-curve), identify the SNeIa91bg and discard them from the DR2. However, this method is challenging since SNeIa91bg are difficult to distinguish from regular SNeIa. The second approach is to add this population in the simulations, (Nugent, Kim, and Perlmutter 2002) could be used as a transient model (the same way SALT2 is used for regular SNeIa). This method has its challenging sides as well, since the rate of sub-luminous population remains imprecisely estimated.

- **Intermediate-z** ($0.04 < z < 0.12$): we see a higher number of objects in the simulated sample than in the observed ones. This difference shows the missing objects, the transients that were detected but were not classified and thus are not in the DR2 sample.

- **At high-z** ($z > 0.12$): intriguingly, the number of observed SNeIa in the DR2 sample is higher than the simulated ones. It implies that classified SNeIa in the simulated sample are missing. This difference is due to the fact that we compare a simulated sample with BTS selection to the DR2 one with unknown selection function. BTS classifies bright transients, as clearly shown with the efficiency function (Fig 7.24), any transient fainter than 19 mag is not classified. It is noticeable in Fig 7.27, where many of DR2 objects from this redshift range display a peak magnitude > 19 mag. These objects, too faint to be classified by the BTS program, were classified by other spectroscopic resources. A sum-up of the spectroscopic resources that carried out the classification of the DR2 sample is presented in Section 3.2.2. Moreover, some DR2 objects, in addition to main survey, can have data points in their light-curves observed with partnership time. The latter are not available in the main survey data and thus are not used when the transient is classified by BTS. However, these data points are in the DR2 light-curves that we used and may pass the BTS cuts in Section 7.4.2. This part of Fig 7.26 shows that we need an extension to the selection function used in the simulations.

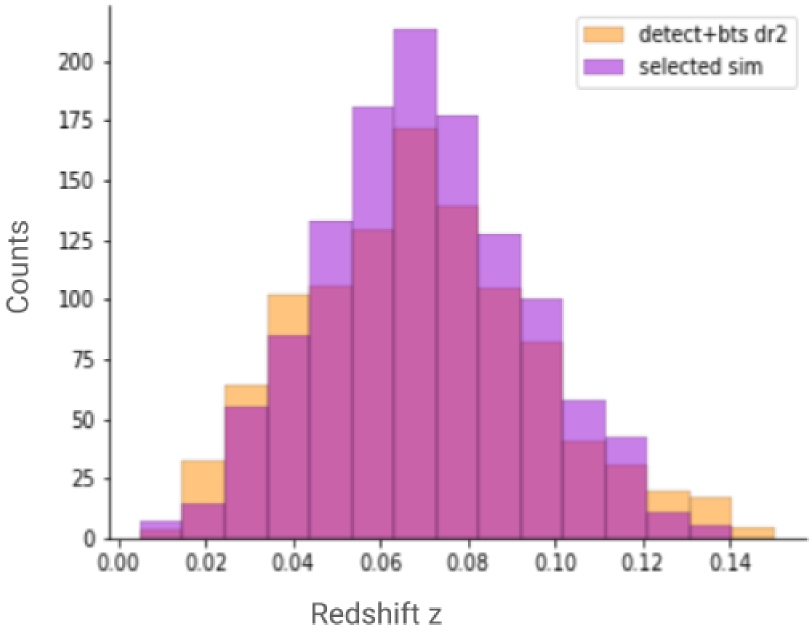

Figure 7.26: Application of the spectroscopic efficiency on the selected sample and comparison to the selected DR2.

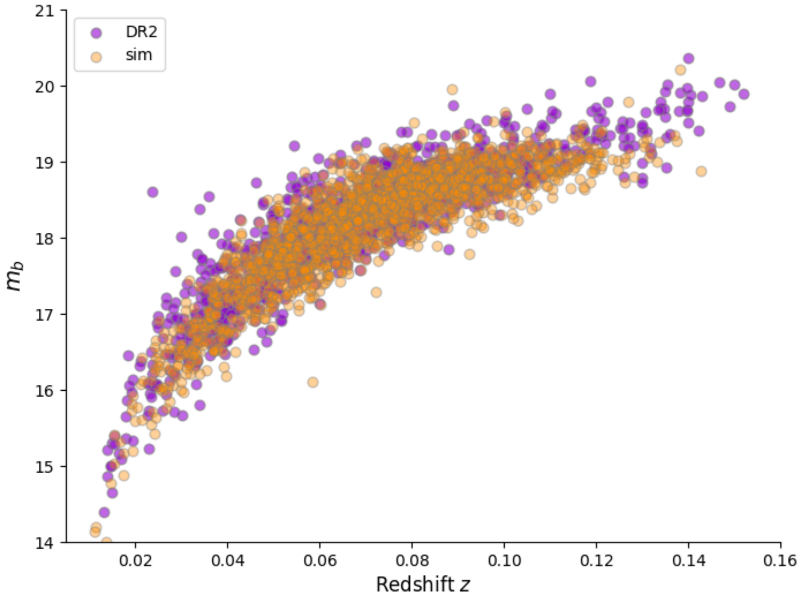

Figure 7.27: Peak apparent magnitudes in B band in function of the redshifts for the DR2 and simulated selected samples from Fig 7.26.

7.4.4 Summary

We use simsurvey with ZTF observing information and realistic transient model to study ZTF spectroscopic selection of the DR2 sample. Most of the DR2 SNeIa are classified by the Bright Transient Survey (BTS). We apply the BTS spectroscopic selection function on our simulated one. We compare the redshift distributions of the DR2 sample and the simulated selected one. The comparison enable us to recover missing SNeIa in the DR2 sample. We also identify incompatibilities, at low-z with DR2 contamination by sub-luminous population and at high-z with the limit of BTS spectroscopic efficiency. ZTF DR2 sample is unbiased to $z = 0.05$, given a set of criteria and SNeIa model.

7.5 Conclusion

In this chapter, we used simsurvey to build realistic simulations framework based on true ZTF cadence to reproduce individual objects from the ZTF DR2 sample, investigate biases in distance measurements and study the DR2 sample selection.

We used the DR2 light-curves measured parameters in simsurvey to simulate 3613 SNeIa from the DR2. We found that the fluxes, uncertainties and SNR are in excellent agreement between the simulations and the DR2 objects if we account for 2% flux level in the simulated uncertainties, in addition to the calibration errors for the DR2 and the simulated sample. The origin of the extra flux level we need to add to make the simulations and DR2 match is unknown. In the future, there is a set of improvements we will make for our realistic simulations to be more accurate. We will add more sources of uncertainties in the simulations including background from host-galaxies and ensure that SNeIa from massive host galaxies are simulated brighter and account for redshift uncertainties. We have seen that the photometric calibration precision varies from one ZTF band to the other, we will reproduce the DR2 sample with different photometric precision for *ztfg* and *ztfr* bands. (Pierel et al. 2022) developed a new SED model for SNeIa (SALT3), trained on dataset on the Near Infra-Red (NIR). We can use this new extended SNeIa model in to generate light-curves in simsurvey. A further approach would be to compare our simulated light-curves to new ZTF ones extracted from scene-modelling technique (Holtzman et al. 2008).

In Section 7.3.1, we used our simulations framework to study biases in the distance measurements. We compared the underlying population of x_1 and c, from realistic distribution input to simsurvey, to the fitted values. We found no evidence of bias in x_1 or c parameters. ZTF will measure SALT2 parameters c and x_1 to respectively 0.035 and 0.4 to $z = 0.1$. Based on (Gris et al. 2022), we can infer that ZTF will measure distances with a precision of 0.16 mag, comparable for an individual object to the intrinsic scatter (σ_{int}). For ZTF SNeIa of an average $z = 0.07$, we will measure distances at the same accuracy as SNeIa from the Legacy Survey of Space and Time (LSST) at $z = 0.7$.

DR2 SNeIa are all spectroscopically classified, multiple spectroscopic resources were involved in their classifications. We know from Section 3.2.2 that the majority of DR2 objects were classified by the Bright Transient Survey (BTS) program. In order to study the

DR2 sample selection, we applied the BTS spectroscopic selection function on our simulations. We compared the redshift distributions of the DR2 and selected simulated samples. We found a good match between the distributions, the DR2 sample is unbiased up to $z = 0.05$. However, we notice more objects in the DR2 sample at very low and high redshift. The excess of DR2 objects at low-z is explained by the contamination of the sample by sub-luminous SNeIa. We suggested two approaches to fix this issue: identify all the sub-luminous SNeIa in the sample and remove them or include this population in our simulations. At high-z, we found more DR2 objects than simulated ones because these objects were too faint to be classified by BTS. We need to extend the selection function to account for faint objects.

For the simulations used in biases and selection studies (Section 7.3.1 and 7.4), one relevant improvement is the use of more realistic underlying populations distribution like SK16 (Scolnic and Kessler 2016). Furthermore, we should account for dependence of SNeIa on their host-galaxies like in (Nicolas, N. et al. 2021; Popovic et al. 2021).

Outlook

In this chapter, we elaborate the most realistic ZTF simulations to understand our sample, its biases and selection. We have a large, homogeneous and unbiased SNeIa sample. Fig 7.28 shows the sky map in Galactic coordinates with objects of the DR2 sample, in the left and the associated simulations after applying the BTS spectroscopic selection function in the right. This sample will be used to test ΛCDM in the local universe and provide one of the first most precise bulk flow measurements with SNeIa. Moreover, this sample can be used to contribute to solve H_0 and σ_8 tensions, introduced in Section 1.2.

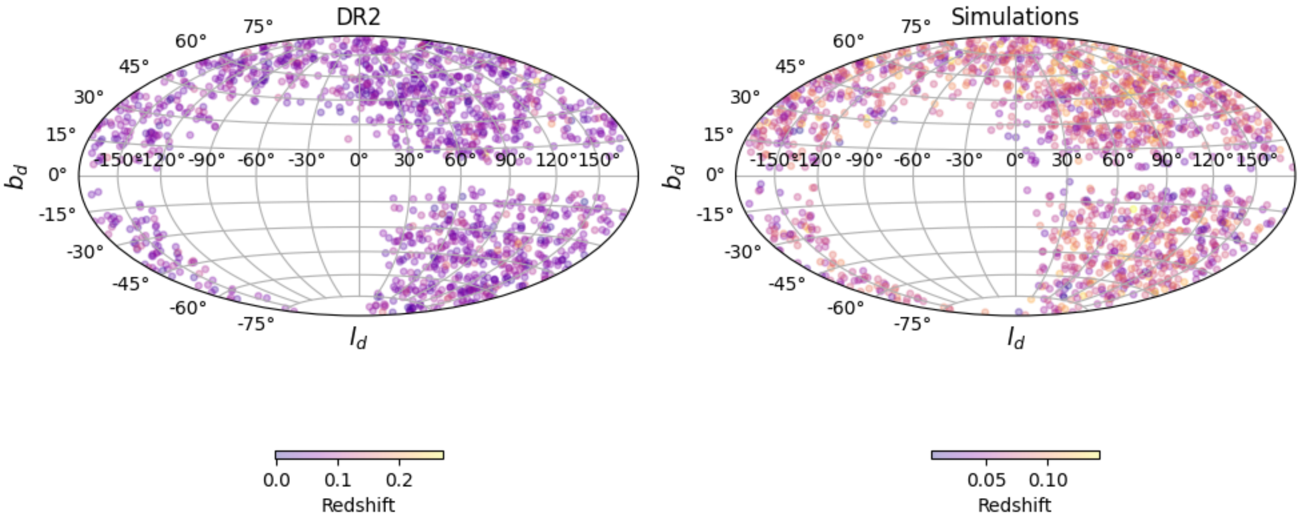

Figure 7.28: ***Left:*** DR2 sky map after BTS requirements, in Galactic coordinates. *Right:* simulated selected sample sky map in Galactic coordinates. Both maps are colored per redshift.

CONCLUSION AND PERSPECTIVES

SNeIa are excellent distance indicators. They enable us to probe the Universe and test the ΛCDM model at multiple redshift ranges. In this thesis, we focused our efforts on the Zwicky Transient Facility (ZTF) SNeIa data, collected to a redshift limit of $z = 0.12$. Low-z SNeIa are critical to cosmological studies, for instance, anchored with high-z data they are used to characterise Dark Energy (DE) equation of state. However, the critical missing piece for ZTF sample to contribute to unveil the most precise measurements of DE is the photometric calibration at the sub-percent level. In Chapter 4, we introduced our work on improving the photometric calibration. We showed how we took into account ZTF true observing conditions in the estimation of the Zero Point (ZP) images. We compared the dispersion of calibrators magnitude computed with the pipeline method and computed with our approach. It reduced the dispersion of the magnitude calibrators. We also developed a multi-epoch fit in which we estimated the ZP for a set of images at the same time, in addition to consider observing conditions. We found an approach to identify bad observing nights. When they are removed from the images of the multi-epoch fit, the dispersion is decreased by 15%. All this work was a preliminary study of bigger efforts ongoing on (Padmanabhan et al. 2008b) development for ZTF.

Another part of the thesis was to investigate bulk flows detectability with ZTF data. We developed, in Chapter 6, fast simulations distances modulus and their associated uncertainties based on ZTF Data Release 1 (DR1), first year of ZTF observations. We applied the dipole method, from (Bonvin, Durrer, and Kunz 2006), to constrain the bulk flow velocity and location for 1000 samples of 800 SNeIa. We did the estimation per redshift shell. We found high limits of bulk flow detection when compared with ΛCDM predictions. It indicates that using only the first year of ZTF data to detect bulk flow with the dipole method is inconclusive. ZTF survey has been successfully running for five years, the use of the final sample will significantly reduce the uncertainties on bulk flow measurements with SNeIa data.

To ensure that the SNeIa distances are well measured to be used in bulk flow measurements, we need to understand the biases and selection of the sample used. The only way to do this is through realistic simulations. In Chapter 7.1.3, we sought to develop the most realistic simulations. To this end, we have used all our knowledge on ZTF observations and SNeIa model and input it to a simulation tool, simsurvey from (Feindt et al. 2019). We used this framework to reproduce the whole ZTF DR2 sample, namely 3613 objects. We compared their measured and simulated fluxes, uncertainties and Signal-to-Noise Ratios. We found that all the quantities are in excellent agreement when we account for 2% flux level in the simulations, in addition to considering calibration uncertainties. In a second study, we used this simulation framework to estimate biases in the distance measurements. We did a comparison of the underlying population of the SALT2 x_1 and c parameters to the fitted ones. We found no evidence of biases resulting from this comparison. We showed that ZTF will measure x_1 and c to 0.4 and 0.035 respectively, up to $z = 0.1$. We used (Gris et al. 2022) to infer that ZTF can measure distances with a precision of 0.16 mag, comparable for an individual object to the intrinsic scatter (σ_{int}). The last study we completed with the simulations framework is the assessment of the DR2 spectroscopic selection. We aimed to apply the DR2 spectroscopic selection function to the simulated sample and compare them in order to investigate the DR2 selection. We applied the Bright Transient Survey (BTS) spectrsocopic selection function, since the majority of DR2 SNeIa were classified by this program, to the simulations and the DR2 sample. We compared the redshift distribution of both selected samples. We found a good match between the distributions and no bias up to $z = 0.05$. Some disagreements at very low and very high redshift were noticed. At low redshift, the DR2 sample is contaminated by sub-luminous SNeIa, which are not included in the simulations. At high redshift, our study showed that we need to extend the spectroscopic selection function used to fainter objects.

Amongst the two main problems in SNeIa cosmology, we find calibration and selection. In this present thesis, we presented our work in both of them on a sample that will anchor any Hubble diagram in the next decade. With its high statistics along with its homogeneity and the absence of bias, ZTF survey provides a key sample to test the standard model of cosmology and understand its current tensions. With the ongoing project to implement the state-of-the-art calibration pipeline, ZTF final sample will be crucial for DE characterisation studies.

BIASES STUDY

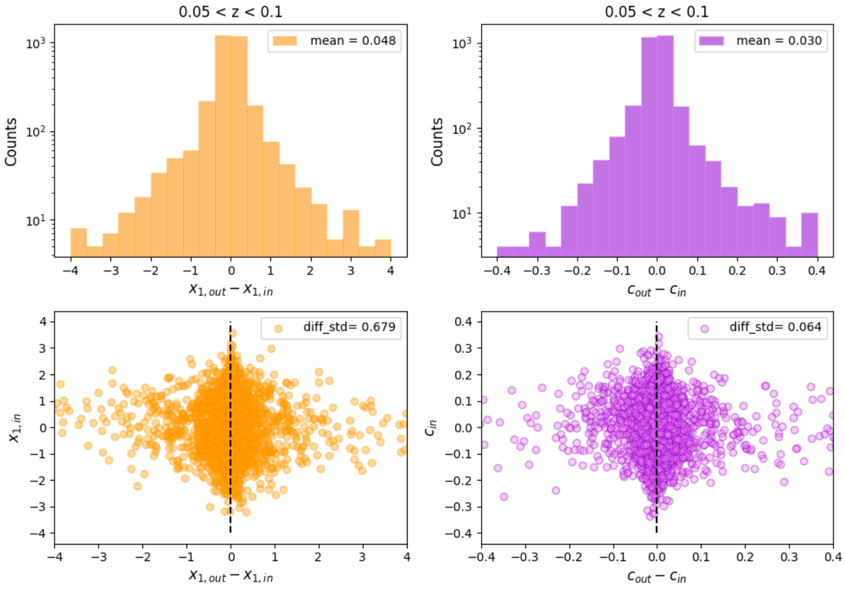

Figure 29: *Top:* difference distributions of x_1, in the left and c in the right. *Bottom:* $x_{1,in}$ in the left and c_{in} in the right in function of their differences for $0.05 < z < 0.1$.

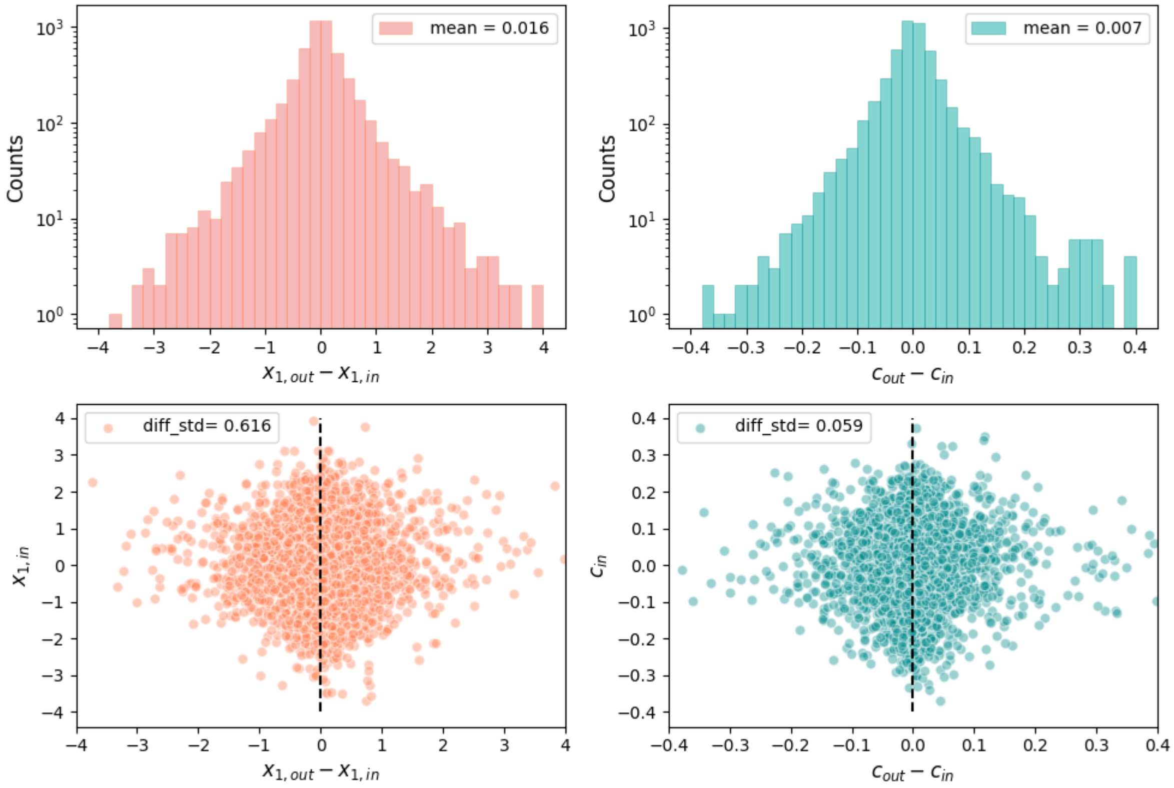

Figure 30: *Top:* after BTS cuts difference distributions of x_1, in the left and c in the right. *Bottom:* after BTS cuts$x_{1,in}$ in the left and c_{in} in the right in function of their differences for $0.05 < z < 0.1$.

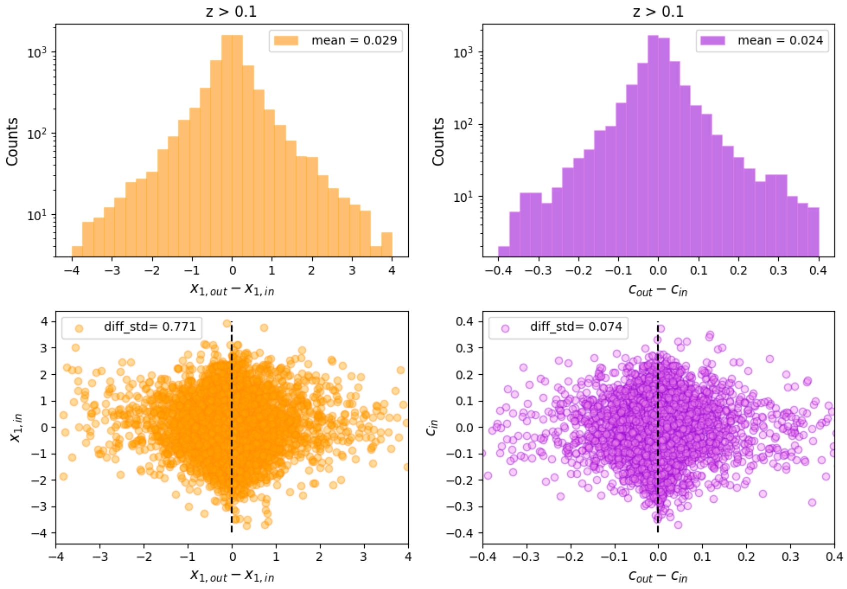

Figure 31: *Top:* difference distributions of x_1, in the left and c in the right. *Bottom:* $x_{1,in}$ in the left and c_{in} in the right in function of their differences for $z > 0.1$.

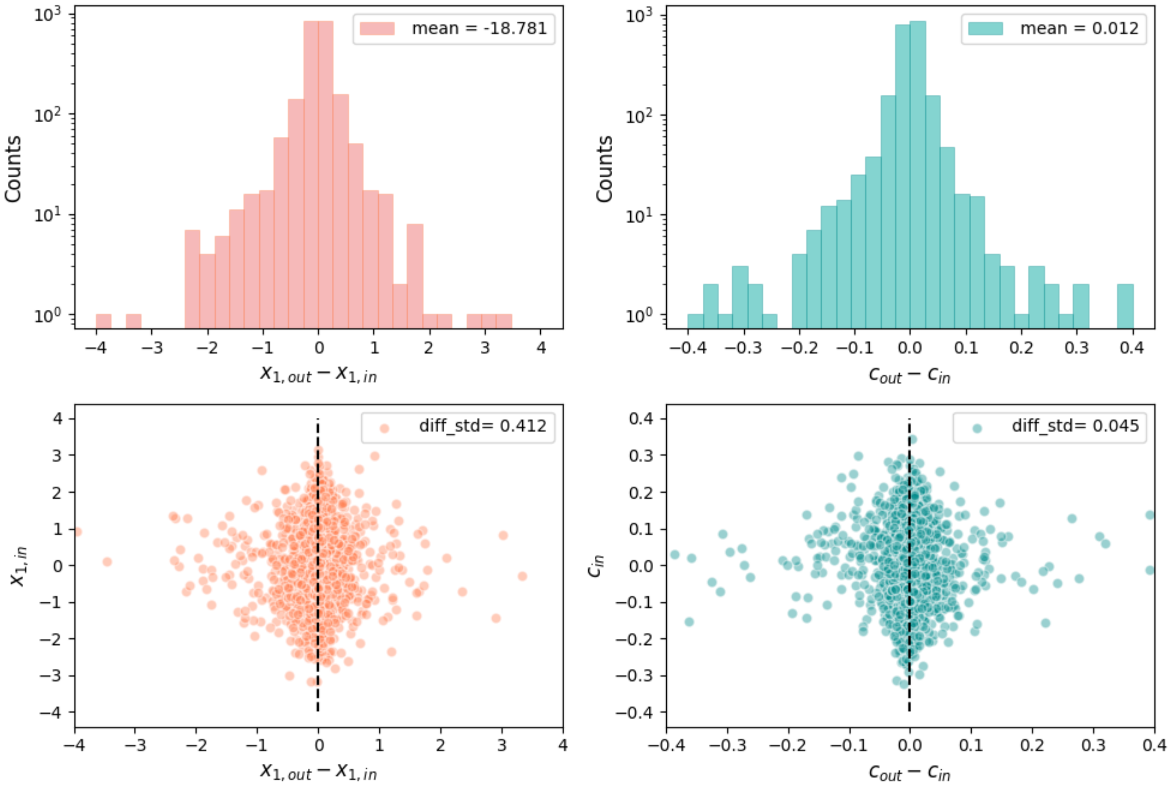

Figure 32: *Top:* after BTS cuts difference distributions of x_1, in the left and c in the right. *Bottom:* after BTS cuts$x_{1,in}$ in the left and c_{in} in the right in function of their differences for $z > 0.1$.

BIBLIOGRAPHY

Abbott, T. M. C. et al. (Aug. 2018). "Dark Energy Survey year 1 results: Cosmological constraints from galaxy clustering and weak lensing". In: 98.4, 043526, p. 043526. DOI: 10.1103/PhysRevD.98.043526. arXiv: 1708.01530 [astro-ph.CO].

Amanullah, R. et al. (2010). "SPECTRA ANDiHUBBLE SPACE TELESCOPE/iLIGHT CURVES OF SIX TYPE Ia SUPERNOVAE AT 0.511 &ltiz/i&lt 1.12 AND THE UNION2 COMPILATION". In: *The Astrophysical Journal* 716.1, pp. 712–738. DOI: 10.1088/0004-637x/716/1/712. URL: https://doi.org/10.1088\%2F0004-637x\%2F716\%2F1\%2F712.

Antilogus, P et al. (2014). "The brighter-fatter effect and pixel correlations in CCD sensors". In: *Journal of Instrumentation* 9.03, pp. C03048–C03048. DOI: 10.1088/1748-0221/9/03/c03048. URL: https://doi.org/10.1088\%2F1748-0221\%2F9\%2F03\%2Fc03048.

Astier, P. et al. (Feb. 2006). "The Supernova Legacy Survey: measurement of Ω_M, Ω_Λ and w from the first year data set". In: 447.1, pp. 31–48. DOI: 10.1051/0004-6361:20054185. arXiv: astro-ph/0510447 [astro-ph].

Astier, P. et al. (2013). "Photometry of supernovae in an image series: methods and application to the SuperNova Legacy Survey (SNLS)". In: *Astronomy &amp Astrophysics* 557, A55. DOI: 10.1051/0004-6361/201321668. URL: https://doi.org/10.1051\%2F0004-6361\%2F201321668.

Bellm, Eric C. et al. (2018). "The Zwicky Transient Facility: System Overview, Performance, and First Results". In: *Publications of the Astronomical Society of the Pacific* 131.995, p. 018002. DOI: 10.1088/1538-3873/aaecbe. URL: https://doi.org/10.1088\%2F1538-3873\%2Faaecbe.

Bertin, E. and Arnouts, S. (1996). "SExtractor: Software for source extraction". In: *Astron. Astrophys. Suppl. Ser.* 117.2, pp. 393–404. DOI: 10.1051/aas:1996164. URL: https://doi.org/10.1051/aas:1996164.

Betoule, M. et al. (2013). "Improved photometric calibration of the SNLS and the SDSS supernova surveys". In: *Astronomy &amp Astrophysics* 552, A124. DOI: 10.1051/0004-6361/201220610. URL: https://doi.org/10.1051\%2F0004-6361\%2F201220610.

Betoule, M. et al. (Aug. 2014). "Improved cosmological constraints from a joint analysis of the SDSS-II and SNLS supernova samples". In: 568, A22, A22. DOI: 10.1051/0004-6361/201423413. arXiv: 1401.4064 [astro-ph.CO].

Blagorodnova, Nadejda et al. (Mar. 2018). "The SED Machine: A Robotic Spectrograph for Fast Transient Classification". In: 130.985, p. 035003. DOI: 10.1088/1538-3873/aaa53f. arXiv: 1710.02917 [astro-ph.IM].

Blas, Diego, Julien Lesgourgues, and Thomas Tram (2011). "The Cosmic Linear Anisotropy Solving System (CLASS) II: Approximation schemes". In: *JCAP* 07, p. 034. DOI: 10.1088/1475-7516/2011/07/034. arXiv: 1104.2933 [astro-ph.CO].

Blondin, Stephane and John L. Tonry (2007). “Determining the Type, Redshift, and Age of a Supernova Spectrum”. In: *The Astrophysical Journal* 666.2, pp. 1024–1047. doi: 10.1086/520494. url: https://doi.org/10.1086\%2F520494.

Bonvin, Camille, Ruth Durrer, and Martin Kunz (2006). “Dipole of the Luminosity Distance: A Direct Measure of $H(z)$”. In: *Phys. Rev. Lett.* 96 (19), p. 191302. doi: 10.1103/PhysRevLett.96.191302. url: https://link.aps.org/doi/10.1103/PhysRevLett.96.191302.

Boruah, Supranta S., Michael J. Hudson, and Guilhem Lavaux (Oct. 2020). “Cosmic flows in the nearby Universe: new peculiar velocities from SNe and cosmological constraints”. In: *Monthly Notices of the Royal Astronomical Society* 498.2, pp. 2703–2718. doi: 10.1093/mnras/staa2485. arXiv: 1912.09383 [astro-ph.CO].

Branch, David, E. Baron, and David J. Jeffery (2001). *Optical Spectra of Supernovae.* doi: 10.48550/ARXIV.ASTRO-PH/0111573. url: https://arxiv.org/abs/astro-ph/0111573.

Brout, D. et al. (2019). “First Cosmology Results Using Type Ia Supernovae from the Dark Energy Survey: Photometric Pipeline and Light-curve Data Release”. In: *The Astrophysical Journal* 874.1, p. 106. doi: 10.3847/1538-4357/ab06c1. url: https://doi.org/10.3847\%2F1538-4357\%2Fab06c1.

Cardelli, Jason A., Geoffrey C. Clayton, and John S. Mathis (Oct. 1989). “The Relationship between Infrared, Optical, and Ultraviolet Extinction”. In: 345, p. 245. doi: 10.1086/167900.

Carrick, Jonathan et al. (Apr. 2015). “Cosmological parameters from the comparison of peculiar velocities with predictions from the 2M++ density field”. In: *Monthly Notices of the Royal Astronomical Society* 450.1, pp. 317–332. issn: 0035-8711. doi: 10.1093/mnras/stv547. eprint: https://academic.oup.com/mnras/article-pdf/450/1/317/18510270/stv547.pdf. url: https://doi.org/10.1093/mnras/stv547.

Chambers, K. C. et al. (2016). *The Pan-STARRS1 Surveys.* doi: 10.48550/ARXIV.1612.05560. url: https://arxiv.org/abs/1612.05560.

Chandrasekhar, S. (July 1931). “The Maximum Mass of Ideal White Dwarfs”. In: 74, p. 81. doi: 10.1086/143324.

Chevallier, Michel and David Polarski (2001). “Accelerating universes with scaling dark matter”. In: *Int. J. Mod. Phys. D* 10, pp. 213–224. doi: 10.1142/S0218271801000822. arXiv: gr-qc/0009008.

Childress, M. et al. (June 2013). “Host Galaxy Properties and Hubble Residuals of Type Ia Supernovae from the Nearby Supernova Factory”. In: 770.2, 108, p. 108. doi: 10.1088/0004-637X/770/2/108. arXiv: 1304.4720 [astro-ph.CO].

Chotard, Nicolas (Oct. 2011). “Étude de la variabilité des Supernovae de type Ia observées par la collaboration Nearby Supernova Factory”. Theses. Université Claude Bernard - Lyon I. url: https://tel.archives-ouvertes.fr/tel-00660289.

Colin, Jacques et al. (June 2011). “Probing the anisotropic local Universe and beyond with SNe Ia data”. In: *Monthly Notices of the Royal Astronomical Society* 414.1, pp. 264–271.

ISSN: 0035-8711. DOI: 10.1111/j.1365-2966.2011.18402.x. eprint: https://academic.oup.com/mnras/article-pdf/414/1/264/3804927/mnras0414-0264.pdf. URL: https://doi.org/10.1111/j.1365-2966.2011.18402.x.

Colin, Jacques et al. (2019). "Evidence for anisotropy of cosmic acceleration". In: *Astronomy &amp Astrophysics* 631, p. L13. DOI: 10.1051/0004-6361/201936373. URL: https://doi.org/10.1051\%2F0004-6361\%2F201936373.

Davis, Tamara M. and Morag I. Scrimgeour (June 2014). "Deriving accurate peculiar velocities (even at high redshift)". In: *Monthly Notices of the Royal Astronomical Society* 442.2, pp. 1117–1122. ISSN: 0035-8711. DOI: 10.1093/mnras/stu920. eprint: https://academic.oup.com/mnras/article-pdf/442/2/1117/5749233/stu920.pdf. URL: https://doi.org/10.1093/mnras/stu920.

Dekany, Richard et al. (2020a). "The Zwicky Transient Facility: Observing System". In: *Publications of the Astronomical Society of the Pacific* 132.1009, p. 038001. DOI: 10.1088/1538-3873/ab4ca2. URL: https://doi.org/10.1088\%2F1538-3873\%2Fab4ca2.

Dekany, Richard et al. (2020b). "The Zwicky Transient Facility: Observing System". In: *Publ. Astron. Soc. Pac.* 132, p. 038001. DOI: 10.1088/1538-3873/ab4ca2. arXiv: 2008.04923 [astro-ph.IM].

Dhawan, S et al. (2021). "The Zwicky Transient Facility Type Ia supernova survey: first data release and results". In: *Monthly Notices of the Royal Astronomical Society* 510.2, pp. 2228–2241. DOI: 10.1093/mnras/stab3093. URL: https://doi.org/10.1093\%2Fmnras\%2Fstab3093.

Di Valentino, Eleonora et al. (2021a). "Cosmology Intertwined III: fσ8 and S8". In: *Astroparticle Physics* 131, p. 102604.

Di Valentino, Eleonora et al. (2021b). "In the realm of the Hubble tension—a review of solutions". In: *Classical and Quantum Gravity* 38.15, p. 153001.

Einstein, Albert (Jan. 1917). "Kosmologische Betrachtungen zur allgemeinen Relativitätstheorie". In: *Sitzungsberichte der Königlich Preussischen Akademie der Wissenschaften*, pp. 142–152.

Feindt, U. et al. (Dec. 2013). "Measuring cosmic bulk flows with Type Ia supernovae from the Nearby Supernova Factory". In: 560, A90, A90. DOI: 10.1051/0004-6361/201321880. arXiv: 1310.4184 [astro-ph.CO].

Feindt, Ulrich et al. (2019). "simsurvey: estimating transient discovery rates for the Zwicky transient facility". In: *Journal of Cosmology and Astroparticle Physics* 2019.10, pp. 005–005. DOI: 10.1088/1475-7516/2019/10/005.

Filippenko, Alexei V. (Jan. 1997a). "Optical Spectra of Supernovae". In: 35, pp. 309–355. DOI: 10.1146/annurev.astro.35.1.309.

— (Jan. 1997b). "Optical Spectra of Supernovae". In: 35, pp. 309–355. DOI: 10.1146/annurev.astro.35.1.309.

Flewelling, H. A. et al. (2020). “The Pan-STARRS1 Database and Data Products”. In: *The Astrophysical Journal Supplement Series* 251.1, p. 7. doi: 10.3847/1538-4365/abb82d. url: https://doi.org/10.3847\%2F1538-4365\%2Fabb82d.

Freedman, Wendy L. et al. (May 2001). “Final Results from the Hubble Space Telescope Key Project to Measure the Hubble Constant”. In: 553.1, pp. 47–72. doi: 10.1086/320638. arXiv: astro-ph/0012376 [astro-ph].

Fremling, U. C. et al. (2019). *The Zwicky Transient Facility Bright Transient Survey I: Spectroscopic Classification and the Redshift Completeness of Local Galaxy Catalogs.* doi: 10.48550/ARXIV.1910.12973. url: https://arxiv.org/abs/1910.12973.

Friedmann, Aleksandr (1922). “125. on the curvature of space”. In: *Zeitschrift für Physik* 10, pp. 377–386.

Goobar, Ariel and Bruno Leibundgut (2011). “Supernova Cosmology: Legacy and Future”. In: *Annual Review of Nuclear and Particle Science* 61.1, pp. 251–279. doi: 10.1146/annurev-nucl-102010-130434. eprint: https://doi.org/10.1146/annurev-nucl-102010-130434. url: https://doi.org/10.1146/annurev-nucl-102010-130434.

Graham, Matthew J. et al. (2019). “The Zwicky Transient Facility: Science Objectives”. In: *Publications of the Astronomical Society of the Pacific* 131.1001, p. 078001. doi: 10.1088/1538-3873/ab006c. url: https://doi.org/10.1088\%2F1538-3873\%2Fab006c.

Gris, Philippe et al. (2022). *Designing an Optimal LSST Deep Drilling Program for Cosmology with Type Ia Supernovae.* doi: 10.48550/ARXIV.2205.07651. url: https://arxiv.org/abs/2205.07651.

Gupta, Ravi R. et al. (Oct. 2011). “Improved Constraints on Type Ia Supernova Host Galaxy Properties Using Multi-wavelength Photometry and Their Correlations with Supernova Properties”. In: 740.2, 92, p. 92. doi: 10.1088/0004-637X/740/2/92. arXiv: 1107.6003 [astro-ph.CO].

Guy, J. et al. (Apr. 2007). “SALT2: using distant supernovae to improve the use of type Ia supernovae as distance indicators”. In: 466.1, pp. 11–21. doi: 10.1051/0004-6361:20066930. arXiv: astro-ph/0701828 [astro-ph].

Guy, J. et al. (2010). “The Supernova Legacy Survey 3-year sample: Type Ia supernovae photometric distances and cosmological constraints”. In: *Astronomy &amp Astrophysics* 523, A7. doi: 10.1051/0004-6361/201014468. url: https://doi.org/10.1051\%2F0004-6361\%2F201014468.

Heymans, Catherine et al. (2021). “KiDS-1000 Cosmology: Multi-probe weak gravitational lensing and spectroscopic galaxy clustering constraints”. In: *A&A* 646, A140. doi: 10.1051/0004-6361/202039063. url: https://doi.org/10.1051/0004-6361/202039063.

Hiltner, William Albert (1962). *Astronomical techniques.*

Holtzman, Jon A. et al. (Dec. 2008). "The Sloan Digital Sky Survey-II: Photometry and Supernova IA Light Curves from the 2005 Data". In: 136.6, pp. 2306–2320. DOI: 10.1088/0004-6256/136/6/2306. arXiv: 0908.4277 [astro-ph.CO].

Hubble, Edwin (1929). "A relation between distance and radial velocity among extra-galactic nebulae". In: *Proceedings of the national academy of sciences* 15.3, pp. 168–173.

Hui, Lam and Patrick B. Greene (2006). "Correlated fluctuations in luminosity distance and the importance of peculiar motion in supernova surveys". In: *Physical Review D* 73.12. DOI: 10.1103/physrevd.73.123526. URL: https://doi.org/10.1103\%2Fphysrevd.73.123526.

Humphreys, E. M. L. et al. (2013). "TOWARD A NEW GEOMETRIC DISTANCE TO THE ACTIVE GALAXY NGC 4258. III. FINAL RESULTS AND THE HUBBLE CONSTANT". In: *The Astrophysical Journal* 775.1, p. 13. DOI: 10.1088/0004-637x/775/1/13. URL: https://doi.org/10.1088\%2F0004-637x\%2F775\%2F1\%2F13.

Ivezić, Ž eljko et al. (2007). "Sloan Digital Sky Survey Standard Star Catalog for Stripe 82: The Dawn of Industrial 1% Optical Photometry". In: *The Astronomical Journal* 134.3, pp. 973–998. DOI: 10.1086/519976. URL: https://doi.org/10.1086\%2F519976.

Jerjen, H. and G. A. Tammann (Sept. 1993). "The Local group motion towards Virgo and the microwave background." In: 276, pp. 1–8.

Jha, Saurabh, Adam G. Riess, and Robert P. Kirshner (2007). "Improved Distances to Type Ia Supernovae with Multicolor Light-Curve Shapes: MLCS2k2". In: *The Astrophysical Journal* 659.1, pp. 122–148. DOI: 10.1086/512054. URL: https://doi.org/10.1086\%2F512054.

Kaiser, Nick (1987). "Clustering in real space and in redshift space". In: *Monthly Notices of the Royal Astronomical Society* 227.1, pp. 1–21.

Kalus, B. et al. (2013). "Constraints on anisotropic cosmic expansion from supernovae". In: *A&A* 553, A56. DOI: 10.1051/0004-6361/201220928. URL: https://doi.org/10.1051/0004-6361/201220928.

Kashlinsky, A. et al. (Mar. 2010). "A New Measurement of the Bulk Flow of X-Ray Luminous Clusters of Galaxies". In: 712.1, pp. L81–L85. DOI: 10.1088/2041-8205/712/1/L81. arXiv: 0910.4958 [astro-ph.CO].

Kelly, Patrick L. et al. (June 2010). "Hubble Residuals of Nearby Type Ia Supernovae are Correlated with Host Galaxy Masses". In: 715.2, pp. 743–756. DOI: 10.1088/0004-637X/715/2/743. arXiv: 0912.0929 [astro-ph.CO].

Kessler, Richard et al. (2009). "FIRST-YEAR SLOAN DIGITAL SKY SURVEY-II SUPERNOVA RESULTS: HUBBLE DIAGRAM AND COSMOLOGICAL PARAMETERS". In: *The Astrophysical Journal Supplement Series* 185.1, pp. 32–84. DOI: 10.1088/0067-0049/185/1/32. URL: https://doi.org/10.1088\%2F0067-0049\%2F185\%2F1\%2F32.

Kocevski, Dale D. et al. (2007). "A Systematic X-Ray Search for Clusters of Galaxies behind the Milky Way. II. The Second CIZA Subsample". In: *The Astrophysical Journal* 662.1, pp. 224–235. doi: 10.1086/513303. url: https://doi.org/10.1086/513303.

Kogut, A. et al. (Dec. 1993). “Dipole Anisotropy in the COBE Differential Microwave Radiometers First-Year Sky Maps”. In: 419, p. 1. doi: 10.1086/173453. arXiv: astro-ph/9312056 [astro-ph].

Komatsu, E. et al. (Feb. 2011). “Seven-year Wilkinson Microwave Anisotropy Probe (WMAP) Observations: Cosmological Interpretation”. In: 192.2, 18, p. 18. doi: 10.1088/0067-0049/192/2/18. arXiv: 1001.4538 [astro-ph.CO].

Lahav, Ofer et al. (1991). “Dynamical effects of the cosmological constant”. In: *Mon. Not. Roy. Astron. Soc.* 251, pp. 128–136.

Laher, Russ et al. (Aug. 2017). “Processing Images from the Zwicky Transient Facility”. In.

Lampeitl, Hubert et al. (Oct. 2010). “The Effect of Host Galaxies on Type Ia Supernovae in the SDSS-II Supernova Survey”. In: 722.1, pp. 566–576. doi: 10.1088/0004-637X/722/1/566. arXiv: 1005.4687 [astro-ph.CO].

Leget, P.-F. et al. (2020). “SUGAR: An improved empirical model of Type Ia supernovae based on spectral features”. In: *Astronomy &amp Astrophysics* 636, A46. doi: 10.1051/0004-6361/201834954. url: https://doi.org/10.1051\%2F0004-6361\%2F201834954.

Lemaître, Georges (1927). “Un Univers homogène de masse constante et de rayon croissant rendant compte de la vitesse radiale des nébuleuses extra-galactiques”. In: *Annales de la Société scientifique de Bruxelles*. Vol. 47, pp. 49–59.

Li, Weidong et al. (Apr. 2011). “Nearby supernova rates from the Lick Observatory Supernova Search – III. The rate–size relation, and the rates as a function of galaxy Hubble type and colour”. In: *Monthly Notices of the Royal Astronomical Society* 412.3, pp. 1473–1507. issn: 0035-8711. doi: 10.1111/j.1365-2966.2011.18162.x. eprint: https://academic.oup.com/mnras/article-pdf/412/3/1473/3574597/mnras0412-1473.pdf. url: https://doi.org/10.1111/j.1365-2966.2011.18162.x.

Linder, Eric V. (2003). “Exploring the Expansion History of the Universe”. In: *Phys. Rev. Lett.* 90 (9), p. 091301. doi: 10.1103/PhysRevLett.90.091301. url: https://link.aps.org/doi/10.1103/PhysRevLett.90.091301.

Linder, Eric V. and Robert N. Cahn (2007). “Parameterized beyond-Einstein growth”. In: *Astroparticle Physics* 28.4, pp. 481–488. issn: 0927-6505. doi: https://doi.org/10.1016/j.astropartphys.2007.09.003. url: https://www.sciencedirect.com/science/article/pii/S0927650507001326.

Lundmark, Knut (June 1925). “The Motions and the Distances of Spiral Nebulæ”. In: 85, p. 865. doi: 10.1093/mnras/85.8.865.

Ma, Yin-Zhe and Douglas Scott (Jan. 2013). “Cosmic bulk flows on 50 h^{-1} Mpc scales: a Bayesian hyper-parameter method and multishell likelihood analysis”. In: *Monthly Notices of the Royal Astronomical Society* 428.3, pp. 2017–2028. doi: 10.1093/mnras/sts178. arXiv: 1208.2028 [astro-ph.CO].

Macri, Lucas M. et al. (2019). “The 2MASS Redshift Survey in the Zone of Avoidance”. In: *The Astrophysical Journal Supplement Series* 245.1, p. 6. DOI: 2mass-sky-map. URL: https://doi.org/10.3847\%2F1538-4365\%2Fab465a.

Magnier, Eugene. A. et al. (2020). “Pan-STARRS Photometric and Astrometric Calibration”. In: *The Astrophysical Journal Supplement Series* 251.1, p. 6. DOI: 10.3847/1538-4365/abb82a. URL: https://doi.org/10.3847\%2F1538-4365\%2Fabb82a.

Masci, Frank J. et al. (2018). “The Zwicky Transient Facility: Data Processing, Products, and Archive”. In: *Publications of the Astronomical Society of the Pacific* 131.995, p. 018003. DOI: 10.1088/1538-3873/aae8ac.

Mathews, G. J. et al. (2016). “DETECTABILITY OF COSMIC DARK FLOW IN THE TYPE IA SUPERNOVA REDSHIFT–DISTANCE RELATION”. In: *The Astrophysical Journal* 827.1, p. 60. DOI: 10.3847/0004-637x/827/1/60. URL: https://doi.org/10.3847\%2F0004-637x\%2F827\%2F1\%2F60.

Minkowski, R. (Aug. 1941). “Spectra of Supernovae”. In: 53.314, p. 224. DOI: 10.1086/125315.

Mosher, J. et al. (2014). “COSMOLOGICAL PARAMETER UNCERTAINTIES FROM SALT-II TYPE IA SUPERNOVA LIGHT CURVE MODELS”. In: *The Astrophysical Journal* 793.1, p. 16. DOI: 10.1088/0004-637x/793/1/16. URL: https://doi.org/10.1088/0004-637x/793/1/16.

Ngeow, C-C et al. (2019). “Introducing the Zwicky Transient Facility and the Be star variability program: a progress report at the National Central University”. In: *Journal of Physics: Conference Series* 1231.1, p. 012010. DOI: 10.1088/1742-6596/1231/1/012010. URL: https://doi.org/10.1088/1742-6596/1231/1/012010.

Nicolas, N. et al. (2021). “Redshift evolution of the underlying type Ia supernova stretch distribution”. In: *A&A* 649, A74. DOI: 10.1051/0004-6361/202038447. URL: https://doi.org/10.1051/0004-6361/202038447.

Nielsen, J. T., A. Guffanti, and S. Sarkar (2016). “Marginal evidence for cosmic acceleration from Type Ia supernovae”. In: *Scientific Reports* 6.1. DOI: 10.1038/srep35596. URL: https://doi.org/10.1038\%2Fsrep35596.

Nomoto, K. (Feb. 1982). “Accreting white dwarf models for type I supernovae. I - Presupernova evolution and triggering mechanisms”. In: 253, pp. 798–810. DOI: 10.1086/159682.

Nugent, Peter, Alex Kim, and Saul Perlmutter (Aug. 2002). “K-Corrections and Extinction Corrections for Type Ia Supernovae”. In: 114.798, pp. 803–819. DOI: 10.1086/341707. arXiv: astro-ph/0205351 [astro-ph].

Nugent, Peter E. et al. (2011). “Supernova SN 2011fe from an exploding carbon–oxygen white dwarf star”. In: *Nature* 480.7377, pp. 344–347. DOI: 10.1038/nature10644. URL: https://doi.org/10.1038\%2Fnature10644.

P. A. R. Ade, and et al. (2014). “iPlanck/iintermediate results”. In: *Astronomy &amp Astrophysics* 561, A97. DOI: 10.1051/0004-6361/201321299. URL: https://doi.org/10.1051\%2F0004-6361\%2F201321299.

Padmanabhan, Nikhil et al. (2008a). “An Improved Photometric Calibration of the Sloan Digital Sky Survey Imaging Data”. In: *The Astrophysical Journal* 674.2, pp. 1217–1233. DOI: 10.1086/524677. URL: https://doi.org/10.1086\%2F524677.

Padmanabhan, Nikhil et al. (2008b). “An Improved Photometric Calibration of the Sloan Digital Sky Survey Imaging Data”. In: *The Astrophysical Journal* 674.2, pp. 1217–1233. DOI: 10.1086/524677. URL: https://doi.org/10.1086%2F524677.

Patterson, Maria T. et al. (Jan. 2019). “The Zwicky Transient Facility Alert Distribution System”. In: 131.995, p. 018001. DOI: 10.1088/1538-3873/aae904. arXiv: 1902.02227 [astro-ph.IM].

Peebles, P. J. E. (1980). *The large-scale structure of the universe.*

Perley, Daniel A. et al. (2020). “The Zwicky Transient Facility Bright Transient Survey. II. A Public Statistical Sample for Exploring Supernova Demographics”. In: *The Astrophysical Journal* 904.1, p. 35. DOI: 10.3847/1538-4357/abbd98. URL: https://doi.org/10.3847\%2F1538-4357\%2Fabbd98.

Perlmutter, S. et al. (1999). “Measurements of Ω and Λ from 42 High-Redshift Supernovae”. In: *The Astrophysical Journal* 517.2, pp. 565–586. DOI: 10.1086/307221. URL: https://doi.org/10.1086\%2F307221.

Phillips, M. M. (Aug. 1993). “The Absolute Magnitudes of Type IA Supernovae”. In: 413, p. L105. DOI: 10.1086/186970.

Pierel, J. D. R. et al. (2022). *SALT3-NIR: Taking the Open-Source Type Ia Supernova Model to Longer Wavelengths for Next-Generation Cosmological Measurements.* DOI: 10.48550/ARXIV.2209.05594. URL: https://arxiv.org/abs/2209.05594.

Planck Collaboration et al. (2020). “Planck 2018 results - I. Overview and the cosmological legacy of Planck”. In: *A&A* 641, A1. DOI: 10.1051/0004-6361/201833880. URL: https://doi.org/10.1051/0004-6361/201833880.

Popovic, Brodie et al. (2021). “Improved Treatment of Host-galaxy Correlations in Cosmological Analyses with Type Ia Supernovae”. In: *The Astrophysical Journal* 913.1, p. 49.

Pruzhinskaya, MV et al. (2020). “The dependence of Type Ia Supernovae salt2 light-curve parameters on host galaxy morphology”. In: *Monthly Notices of the Royal Astronomical Society* 499.4, pp. 5121–5135.

Qin, Fei et al. (2021). “Cosmic Flow Measurement and Mock Sampling Algorithm of Cosmicflows-4 Tully-Fisher Catalog”. In: *The Astrophysical Journal* 922.1, p. 59. DOI: 10.3847/1538-4357/ac249d. URL: https://doi.org/10.3847/1538-4357/ac249d.

Regnault, N. et al. (2009). “Photometric calibration of the Supernova Legacy Survey fields”. In: *Astronomy &amp Astrophysics* 506.2, pp. 999–1042. DOI: 10.1051/0004-6361/200912446. URL: https://doi.org/10.1051\%2F0004-6361\%2F200912446.

Riess, Adam G, William H Press, and Robert P Kirshner (1996). “A precise distance indicator: Type Ia supernova multicolor light-curve shapes”. In: *The Astrophysical Journal* 473.1, p. 88.

Riess, Adam G. et al. (Sept. 1998). “Observational Evidence from Supernovae for an Accelerating Universe and a Cosmological Constant”. In: 116.3, pp. 1009–1038. DOI: `10.1086/300499`. arXiv: `astro-ph/9805201 [astro-ph]`.

Riess, Adam G. et al. (Apr. 2011). “A 3% Solution: Determination of the Hubble Constant with the Hubble Space Telescope and Wide Field Camera 3”. In: 730.2, 119, p. 119. DOI: `10.1088/0004-637X/730/2/119`. arXiv: `1103.2976 [astro-ph.CO]`.

Riess, Adam G. et al. (2021). “Cosmic Distances Calibrated to 1% Precision with Gaia EDR3 Parallaxes and Hubble Space Telescope Photometry of 75 Milky Way Cepheids Confirm Tension with Λ CDM”. In: *The Astrophysical Journal Letters* 908.1, p. L6. DOI: `10.3847/2041-8213/abdbaf`. URL: `https://doi.org/10.3847/2041-8213/abdbaf`.

Riess, Adam G. et al. (July 2022). “A Comprehensive Measurement of the Local Value of the Hubble Constant with 1 km s^{-1} Mpc^{-1} Uncertainty from the Hubble Space Telescope and the SH0ES Team”. In: 934.1, L7, p. L7. DOI: `10.3847/2041-8213/ac5c5b`. arXiv: `2112.04510 [astro-ph.CO]`.

Rigault, M. et al. (Dec. 2013a). “Evidence of environmental dependencies of Type Ia supernovae from the Nearby Supernova Factory indicated by local Hα”. In: 560, A66, A66. DOI: `10.1051/0004-6361/201322104`. arXiv: `1309.1182 [astro-ph.CO]`.

— (Dec. 2013b). “Evidence of environmental dependencies of Type Ia supernovae from the Nearby Supernova Factory indicated by local Hα”. In: 560, A66, A66. DOI: `10.1051/0004-6361/201322104`. arXiv: `1309.1182 [astro-ph.CO]`.

Rigault, M. et al. (July 2019). “Fully automated integral field spectrograph pipeline for the SEDMachine: pysedm”. In: 627, A115, A115. DOI: `10.1051/0004-6361/201935344`. arXiv: `1902.08526 [astro-ph.IM]`.

Rigault, Mickael (Aug. 2018). *ztfquery, a python tool to access ZTF data*. Version doi. DOI: `10.5281/zenodo.1345222`. URL: `https://doi.org/10.5281/zenodo.1345222`.

Robertson, Howard P (1929). “On the foundations of relativistic cosmology”. In: *Proceedings of the National Academy of Sciences* 15.11, pp. 822–829.

Roman, M. et al. (July 2018). “Dependence of Type Ia supernova luminosities on their local environment”. In: 615, A68, A68. DOI: `10.1051/0004-6361/201731425`. arXiv: `1706.07697 [astro-ph.GA]`.

Saunders, C. et al. (2018). “SNEMO: Improved Empirical Models for Type Ia Supernovae”. In: *The Astrophysical Journal* 869.2, p. 167. DOI: `10.3847/1538-4357/aaec7e`. URL: `https://doi.org/10.3847\%2F1538-4357\%2Faaec7e`.

Schlafly, Edward F. and Douglas P. Finkbeiner (Aug. 2011). “Measuring Reddening with Sloan Digital Sky Survey Stellar Spectra and Recalibrating SFD”. In: 737.2, 103, p. 103. DOI: `10.1088/0004-637X/737/2/103`. arXiv: `1012.4804 [astro-ph.GA]`.

Schlegel, David J., Douglas P. Finkbeiner, and Marc Davis (June 1998). "Maps of Dust Infrared Emission for Use in Estimation of Reddening and Cosmic Microwave Background Radiation Foregrounds". In: 500.2, pp. 525–553. doi: 10.1086/305772. arXiv: astro-ph/9710327 [astro-ph].

Scolnic, D. and R. Kessler (2016). "MEASURING TYPE IA SUPERNOVA POPULATIONS OF STRETCH AND COLOR AND PREDICTING DISTANCE BIASES". In: *The Astrophysical Journal* 822.2, p. L35. doi: 10.3847/2041-8205/822/2/l35. url: https://doi.org/10.3847\%2F2041-8205\%2F822\%2F2\%2Fl35.

Scolnic, D. M. et al. (June 2018). "The Complete Light-curve Sample of Spectroscopically Confirmed SNe Ia from Pan-STARRS1 and Cosmological Constraints from the Combined Pantheon Sample". In: 859.2, 101, p. 101. doi: 10.3847/1538-4357/aab9bb. arXiv: 1710.00845 [astro-ph.CO].

Scrimgeour, Morag I. et al. (Nov. 2015). "The 6dF Galaxy Survey: bulk flows on 50-70 h-1 Mpc scales". In: *Monthly Notices of the Royal Astronomical Society* 455.1, pp. 386–401. issn: 0035-8711. doi: 10.1093/mnras/stv2146. eprint: https://academic.oup.com/mnras/article-pdf/455/1/386/3059232/stv2146.pdf. url: https://doi.org/10.1093/mnras/stv2146.

Smith, M. et al. (May 2020). "First cosmology results using type Ia supernovae from the Dark Energy Survey: the effect of host galaxy properties on supernova luminosity". In: 494.3, pp. 4426–4447. doi: 10.1093/mnras/staa946. arXiv: 2001.11294 [astro-ph.CO].

Sullivan, M. et al. (Aug. 2010). "The dependence of Type Ia Supernovae luminosities on their host galaxies". In: 406.2, pp. 782–802. doi: 10.1111/j.1365-2966.2010.16731.x. arXiv: 1003.5119 [astro-ph.CO].

Tripp, Robert (Mar. 1998). "A two-parameter luminosity correction for Type IA supernovae". In: 331, pp. 815–820.

Tröster, Tilman et al. (2020). "Cosmology from large-scale structure - Constraining with BOSS". In: *A&A* 633, p. L10. doi: 10.1051/0004-6361/201936772. url: https://doi.org/10.1051/0004-6361/201936772.

Tully, R. B. and J. R. Fisher (Feb. 1977). "A new method of determining distances to galaxies." In: 54, pp. 661–673.

Tully, R. Brent et al. (2014). "The Laniakea supercluster of galaxies". In: *Nature* 513.7516, pp. 71–73. doi: 10.1038/nature13674. url: https://doi.org/10.1038\%2Fnature13674.

Turatto, Massimo (2003). "Classification of Supernovae". In: *Supernovae and Gamma-Ray Bursters*. Springer Berlin Heidelberg, pp. 21–36. doi: 10.1007/3-540-45863-8_3. url: https://doi.org/10.1007\%2F3-540-45863-8_3.

Turnbull, Stephen J. et al. (Jan. 2012). "Cosmic flows in the nearby universe from Type Ia supernovae". In: *Monthly Notices of the Royal Astronomical Society* 420.1, pp. 447–454. issn: 0035-8711. doi: 10.1111/j.1365-2966.2011.20050.x. eprint: https://academic.oup.com/mnras/article-pdf/420/1/

447/18458552/mnras0420-0447.pdf. URL: https://doi.org/10.1111/j.1365-2966.2011.20050.x.

Walker, Arthur G (1933). “Distance in an expanding universe”. In: *Monthly Notices of the Royal Astronomical Society* 94, p. 159.

Whelan, John and Jr. Iben Icko (Dec. 1973). “Binaries and Supernovae of Type I”. In: 186, pp. 1007–1014. DOI: 10.1086/152565.

Yao, Yuhan et al. (2019). “ZTF Early Observations of Type Ia Supernovae. I. Properties of the 2018 Sample”. In: *The Astrophysical Journal* 886.2, p. 152. DOI: 10.3847/1538-4357/ab4cf5. URL: https://doi.org/10.3847\%2F1538-4357\%2Fab4cf5.

Zeldovich, Ya. B. and R. A. Sunyaev (July 1969). “The Interaction of Matter and Radiation in a Hot-Model Universe”. In: 4.3, pp. 301–316. DOI: 10.1007/BF00661821.

Zwicky, Fritz (1933). “The redshift of extragalactic nebulae”. In: *Helvetica Physica Acta* 6, pp. 110–127.

Acknowledgements

These few lines are just a way to express my gratitude to anyone who helped me in his/her own way in my journey. This experience was fulfilling in many ways, we wouldn't think at first sight but on the human plan especially.

First and foremost I would like to deeply thank my supervisor, Philippe Rosnet, for these three years. He guided me through PhD with commitment, kindness and patience. His scientific thinking, pedagogical skills and support provided me with the right working environment. Merci Philippe.
I would like as well to thank Mathew Smith for his kind guidance, involvement and optimism. He is always willing to hear and help. Mat, thank you for everything.
To Pierre Antilogus, Stéphane Monteil, Mickael Rigault, Cécile Roucelle and Lin Yan thank you for agreeing to be part of my jury. The comments and discussions were very much appreciated.

To the LSST group at LPC, current and former members, many thanks for your support and welcoming environment. It was a pleasure to share the working and fun moments with you. This, of course, extends to the whole laboratory, the colleagues from other groups and the administration members.

To the PhD students I met here and there, thanks for the shared moments and all the laughter. This also goes to my friends, met before and during the thesis, inside or outside academia.

To my parents, sisters and my other siblings thank you for unconditionally encouraging and guiding me in my journeys. Lastly to my life partner, you experienced PhD in another way. You carried all the doubts and disappointments that I have experienced (true way before PhD). Thank you for always lifting me up.